A Measurement of the Tau Lepton Lifetime at Argus

by

P.R.B. Saull

A Measurement of
the Tau Lepton Lifetime
at Argus

P.R.B. Saull

Department of Physics
McGill University, Montreal

Abstract

Data taken with the ARGUS detector at DESY, Hamburg, specifically $\tau\bar{\tau}$ pairs produced from e^+e^- collisions in the energy range (10.4-10.6)GeV, are used to make a precision measurement of the tau lifetime. A new method is introduced which is independent of the beam position and envelope, and applicable to tau events having one-three topology. Applied to ARGUS data the method yields a value for the tau lifetime of

$$\tau_\tau = 287 \pm 11(statistical) \pm 8(systematic) \quad \text{fs.}$$

Abstrait

Des données accumulées avec l'aide du detecteur ARGUS situé à DESY, à Hambourg, spécifiquement des leptons $\tau^+\tau^-$ produits lors des collisions e^+e^- à des énergies dans la regime (10.4-10.6)GeV, sont utilisées pour effectuer une mesure précise du temp de vie du lepton tau. Une nouvelle méthode est présentée qui est indépendente de la position et taille du faisceau, et qui est applicable aux événements tau ayant la topologie 1-3. Appliqué aux données ARGUS la méthode fourni une valeur pour le temp de vie du lepton tau de

$$\tau_\tau = 287 \pm 11(statistique) \pm 8(systèmatique) \quad \text{fs.}$$

Acknowledgments

When I first started my Ph.D. my advisor, Prof. David MacFarlane, told me his attitude as a supervisor towards a student was "sink or swim". Although I suspect he didn't have in mind the waters of ARGUS subsequent to shutdown, in retrospect I am pleased he had this approach (and exercised it). It forced me to learn much more than I ordinarily would have, had I been coddled every step of the way in my work. As a corollary to this attitude, he had unwavering patience with me at times when I perhaps deserved harsher treatment. I am grateful for the opportunity he has given me to "sink or swim" and hope that I have managed, in his eyes, to stay afloat.

I am deeply indebted to Dr. Herbert Kapitza. His ground breaking work in calibrating the ARGUS drift chamber, and boundless tracking expertise simplified my life considerably. Hopefully some of his skills have rubbed off. His door was always open to me, despite the fact that I was constantly entering it, and for that I am especially thankful.

It is a pleasure to thank the ARGUS spokesman, Prof. Henning Schröder, who gave me some early suggestions for a thesis topic, made me feel welcome in building 49 when Hera-B personnel were eyeing my space greedily, and sent me off into the real world with a very kind letter of recommendation.

I thank Profs. Bernhard Spaan and Andre Golutvin, for suggesting ways to reduce the multihadron background in my data sample. I thank Dr. Klaus Strahl as well for some valuable discussions on the ARGUS trigger. Dr. David Gilkinson deserves a special mention as well for allowing the conversation to drift to tracking now and then when we were out for a beer.

A very warm thank you goes out to the many people who played soccer with me regularly and kept me sane, in particular the crazy Russians and Ukranians who would play in any type of weather.

I thank all the playful members of *Zimmer 6* for their bizarre antics and fine tea. I particularly wish to thank Klaus Reim for his help in solving various computing problems I experienced.

I'd like to thank my office mates over the years - Richard Van de Water, Peter Kreuzer, Michael Beck, Raoul Zimmerman, Rüdiger Mahn, and Steve Aplin, - for keeping me company. A special mention goes to my longest-lasting office mate, Katerina Tzamariudaki, with whom I shared many a conversation over the common enemy.

A deep apology goes out to my family and friends back in Canada who expected me home much sooner.

My parents played an invaluable role throughout my Ph.D. years. Through loans and several trips to the Bank of Montreal to put my account in order, my Mom managed to keep me fed and topped up with beer. She never gave up trying to put me in touch with God, something I am only now beginning to appreciate. True to the scientist's curiosity, my Dad had a rather warped interest in the tiny details of my work, despite his limited high energy physics background. Talks with him often provided me with a new perspective on my work.

A very special thank you goes out to Edwin Tam for footing the bill for long-distance marathon conference calls with myself and Kevin Dias, who, despite his best efforts, is still fat.

A sarcastic thanks to the Ph.D. experience for making me fat too.

Thanks go to Betty, Lynda, Paula, Joanne, Janice, Paul, and Juan at the McGill end of things for providing a lifeline to the university. At the DESY end, I thank Nora van Looveren, who helped me repeatedly with last minute residence permit renewals, never once complaining.

I will never manage to list all the members, past and present, of the ZEUS-Canada group at DESY who incorporated me as an honorary member, so I'd better not try. Suffice to say that I will long remember the many good times we had together in Hamburg and on European road trips. I get a dopey smile just thinking about them. It's been hard watching the group break up in the last couple of years, and I hope we manage to stay in touch.

I'd like to acknowledge my high school physics teacher, Dr. Nish Mukerji, for having inspired me early on with his enthusiasm, vibrant teaching style, and devotion to his students. There are still a few questions I would like to ask him, but sadly, he died in the senseless 1985 AIR India Flight 182

bombing, only a week after receiving his Ph.D. degree in physics. May he rest in peace.

Most of all I thank you, Laurel, for what has been, and promises to continue to be, a wonderfully rewarding life together. Without your support in the final stretch of my thesis I would not have pulled through in time. In being with you, I am truly blessed.

I'm outta here. :)

Pat Saull
February 1997

Contents

List of Figures

List of Tables

Personal Contributions

The balance of the author's contribution to the ARGUS experiment and science in general is contained in this thesis. Almost all of the work described herein was done by him. This includes, for example, the selection and re-reconstruction of all the data, the recalibration of both the main drift chamber and vertex drift chamber, the realignment of the vertex chamber, the determination of the drift chamber wire positions using the ORIFIT procedure, the determination of the residual track offsets at the origin, and the determination of the track resolution function. The cuts used to select the data were fairly standard ARGUS analysis cuts, and with the exception of some of the vertex cuts, the author claims no credit for them. Although the concept of making a tau lifetime measurement without using the beam spot was not new, carrying out such a measurement in two-dimensions was the author's own idea, and he developed the VIP method to do this. The ORIFIT procedure is also his idea, although it is built on ideas that had already been conceived by Dr. Herbert Kapitza. The vertex beam tube fit code was written and implemented by the author as well, although the idea again came from Dr. Kapitza. Dr. Kapitza is also responsible for the excellent, new procedure used to calibrate the ARGUS drift chamber. Everything else, however, was conceived and executed by the author. Also, all the code necessary to carry out a lifetime measurement, and which did not already exist, was written by the author.

Some of the work by the author that was directly relevant to this thesis but was not emphasised in the text includes a thorough debugging of the ARGUS reconstruction program and Monte Carlo simulation program, a realistic simulation of the VDC and DC cell efficiences derived from exper-

imental data, a rewriting of the VDC alignment code due to its accidental deletion, and many upgrades to the reconstruction and simulation code for the purpose of ensuring as precise and accurate a lifetime measurement as possible.

Some less related contributions include:

- the inclusion of the μVDC and silicon detector readout code in the ARGUS detector simulation program;

- the inclusion of the cradle for the silicon detector process in the ARGUS reconstruction program;

- a completely general track swim package (GSMAIN) capable of correctly handling the non-cylindrical geometries of the μVDC and silicon tracking detectors, and which accounts for multiple scattering, energy loss, and variable magnetic field;

- an investigation into enhancing the selection efficiency for the channel $D \rightarrow K^* \ell \nu$ using vertexing information;

- participation in a study, using secondary vertex D° tagging, of the improvements gained by using the new ARGUS μVDC over the previous VDC (presented at the 1992 *Physics Research Committee* (PRC) at DESY);

- porting ARGUS code between various computer platforms at DESY;

- participation in regular shifts during data taking; and

- regular proof reading of ARGUS papers prior to publication.

Foreword

The original (1992) objective of this thesis was to make an ARGUS measurement of the tau lifetime using a newly installed vertex drift chamber having three-dimensional tracking capability. The measurement was expected to be comparable with the world average lifetime value at the time of (305 ± 6)fs. In 1992 there were indications that tau decays did not respect universality, and a high precision measurement of the tau lifetime would have gone a long way towards resolving that question.

Unfortunately, as a result of failed attempts to improve the specific luminosity of DORIS, the e^+e^- storage ring on which ARGUS took data, it was deemed unfruitful in early 1993 to continue data-taking, and ARGUS was shut down, with the result that only a fraction of the data necessary to carry out an accurate and precise lifetime measurement was collected. For the author, this meant that a new thesis topic had to be found using the large data sample already collected with a previous vertex drift chamber having lower resolving power and two-dimensional tracking ability. A new lifetime method was devised by the author to accomplish this. The method, dubbed the *vertex impact parameter* (VIP) method, is novel in that it is independent of the beam spot position, size and shape. This thesis comprises a detailed description of the VIP method, and its application to the ARGUS data pool.

Despite the simplicity of the method, carrying out a lifetime measurement has been difficult. As is typical with experiments past the data-taking stage, the number of individuals both able and willing to offer useful advice and guidance dropped sharply subsequent to shutdown as scientists moved on to other projects. This forced the students completing analyses to take on a larger share of responsibilities, responsibilities normally shared among the

members of an active collaboration, or carried out by qualified post-doctorate members. In the author's case, the problem was complicated by the decision to embark on a lifetime measurement, for which there is little precedent at ARGUS. Compounded with this was the discovery in 1995 of an alignment problem with the wires in the main drift chamber that had to be corrected. This required a time-consuming recalibration of the main drift chamber and the vertex chamber, and the introduction of a novel wire-finding procedure using di-muon events (see Chapter 7).

In the end, there was not enough time to make a thorough check of the accuracy of the final measurement, and the work in this thesis should not be considered publishable in its current state, although further work may allow this. The precision and accuracy obtainable with the ARGUS data pool has been bettered by various other experiments since the present work began. Therefore, it is not sensible to invest more time and effort attempting to do a more thorough job. Instead, this work should be considered to lie somewhere between a feasibility study and a thorough analysis. It is hoped that some of the suggestions for improvements will be incorporated into future applications of the VIP method, in particular at the still active CLEO collaboration, where a much larger amount of data is available. There, many of the difficulties encountered in an ARGUS analysis could be circumvented. Thus, the introduction and development of the VIP method as detailed in this thesis constitutes a valuable contribution to science.

Ad Majorem Dei Gloriam

Chapter 1

The Standard Model

1.1 Introduction

Over the past several decades, physicists have sought to account for all the properties of subatomic particles and to explain the interactions amongst them. An extensive proliferation of particles, first observed in the fifties and sixties, has been shown to display many symmetries and interrelations that indicate a simpler underlying structure. Several attempts have been made over the years to describe what is observed. Eventually, the now widely-accepted *standard model* emerged as a reliable, testable, and highly predictive theory. On-going and future experiments promise to provide new opportunities to test this model.

Despite its success, the standard model falls somewhat short of being the complete story for particle interactions. Yet it appears to be applicable at the laboratory energies investigated in the field of high energy physics so far, and, in particular, all τ lepton production and decay mechanisms can be understood in its context. Therefore, the standard model is accepted here as the working theory of particle interactions. The remainder of this chapter is devoted to a brief overview of its basic features.

Bosons				
Force	Mediator	Q	Mass (GeV/c^2)	Spin
Gravitational	G	0	0	2
Electromagnetic	γ	0	$< 3 \times 10^{-36}$	1
Weak	$W^{\pm}$	± 1	80.3	1
Weak	Z°	0	91.2	1
Strong	$g_1 \ldots g_8$	0	0	1
—	H°	0	> 58.4	0

Fermions					
Mass (GeV/c^2)	Q	Quark	Lepton	Q	Mass (GeV/c^2)
First Generation					
$0.005 - 0.015^a$	-1/3	d	e	-1	0.0005
$0.002 - 0.008$	2/3	u	ν_e	0	$< 5.1 \times 10^{-9}$
Second Generation					
$0.1 - .3$	-1/3	s	μ	-1	0.106
$1 - 1.6$	2/3	c	ν_μ	0	$< 1.7 \times 10^{-4}$
Third Generation					
$4.1 - 4.5$	-1/3	b	τ	-1	1.777
≈ 180	2/3	t	ν_τ	0	$< 2.4 \times 10^{-2}$

^{a}(Current masses)

Table 1.1: Fundamental particles of the standard model [1].

1.2 General Description of the Standard Model

The four forces observed in nature are gravity, electromagnetism, the strong force and the weak force (see Table 1.1). At the energies available to experimental physicists today, the gravitational force is much too feeble to play an important role in particle interactions; therefore, the standard model is a description of the last three forces alone. The incorporation of gravity and the unification of these four forces remains a theoretical objective and is left to the realm of *theories of everything*. The electromagnetic and weak forces have already been united in the electroweak force and therefore the standard model is more correctly considered to be a mathematical description of the electroweak and strong forces. Various attempts have been made to

formulate a theory which unifies the electroweak and strong forces; these are termed *grand unified theories*.

There are several particles involved in the standard model. Leptons are particles that experience the weak force but not the strong. They include the massive electron, muon, and tau and their associated massless [1] neutrinos. The first three have electric charge and therefore may participate in electromagnetic interactions. The neutrinos have no electric charge and hence interact only weakly with other particles; they are therefore effectively impossible to detect directly in practical collider detectors. Although the tau neutrino has not been directly observed, its existence can be inferred from the large missing momentum observed in tau decays. Also in this model are six massive quarks, the fundamental building blocks of mesons and baryons. They experience the strong, weak, and electromagnetic interactions and have fractional electric charges: 2/3 for the u, c and t quarks and $-1/3$ for the d, s and b quarks (in units of proton charge). In order to overcome an early difficulty with the theory, quarks had to be endowed with an additional quantum number called colour. The adoption of colour leads quite naturally in the context of gauge theory to the strong force. Except for the t (or top) quark, the properties of the quarks have been extensively studied, and the existence of quarks is on firm ground experimentally. Until 1994, evidence for the existence of the top quark was derived primarily from the absence of flavour-changing neutral currents, and the observation of $B\overline{B}$ mixing at ARGUS [2] and CLEO [3]. More direct evidence has come recently through invariant mass studies of 2-, 3-, and 4-jet events at D0 [4] and CDF [5].

All the above particles are spin 1/2 fermions, and must therefore respect the Pauli exclusion principle which states that no two identical fermions can occupy the same space-time-spin point. It is therefore natural to associate them with matter [6]. Indeed, the basic building blocks of matter, electrons, protons, and neutrons, are all fermions. Bosons, on the other hand, need not satisfy the exclusion principle, and they create fields with which the fermions interact. Interactions between particles thus occur through the exchange of

---

[1]The possibility that neutrinos are endowed with a tiny mass has not been ruled out. However, the standard model in its present form assumes this mass to be zero.

virtual (off mass shell) spin 1 gauge bosons which arise in the theory quite naturally from the principle of gauge invariance. The massless, uncharged photon is the mediator of the electromagnetic force while the very heavy electrically charged W's and neutral Z mediate the weak interaction. Eight massless gluons carrying colour charge but not electric charge are responsible for the strong force. Because they have colour, they interact strongly with each other.

In addition to the above fields, the standard model assumes the existence of the neutral Higgs scalar field (H°) in order to endow particles with mass. As yet, there is no experimental evidence for the Higgs field.

1.3 Standard Model Physics Relevant to Tau Decays

This thesis focuses on a particular property of the tau lepton, i.e. its *lifetime*. To facilitate a detailed discussion of the physics of the tau lepton in the next chapter, it is useful to investigate more thoroughly certain areas of the standard model. Tau leptons decay through the weak force into leptons and quarks and therefore a description of the electro-weak Langrangian is provided. An overview of *quantum chromodynamics* (QCD) is desirable for an understanding of how quarks produced in hadronic tau decays manifest themselves. An understanding of the CKM matrix is also relevant for the quark sector. Finally, the physics of e^+e^- collisions is discussed in order to explain how tau pairs are produced at ARGUS.

1.3.1 The Electroweak Lagrangian

Because the main emphasis in this work is on weak decays of the tau meson, only the charged-current weak Lagrangian of the quark and leptonic sectors will be presented. The quarks and leptons can be arranged into three families (or generations) of left-handed $SU(2)$ doublets and right-handed singlets [2].

---

[2]There is no theoretical reason why more families could not exist, but measurements of the width of the Z [1] indicate that $n_f = 3$, if one assumes that additional families would have light neutrinos.

The doublets **L** are given by

$$\begin{pmatrix} \nu_e \\ e^- \end{pmatrix}_L , \quad \begin{pmatrix} \nu_\mu \\ \mu^- \end{pmatrix}_L , \quad \begin{pmatrix} \nu_\tau \\ \tau^- \end{pmatrix}_L , \quad \begin{pmatrix} u \\ d \end{pmatrix}_L , \quad \begin{pmatrix} c \\ s \end{pmatrix}_L , \quad \begin{pmatrix} t \\ b \end{pmatrix}_L .$$

This is a reflection of the maximal parity violation of weak decays observed in nature: the left- and right-handed components of a spinor field do not experience the weak interaction with equal strengths. Because right-handed spinors do not participate in charged-current weak interactions at all, the asymmetry is termed "maximal".

The leptonic sector of the weak charged-current Lagrangian can be written in terms of these doublets as (interaction terms only)

$$\begin{aligned} \mathcal{L}_{lep} &= -\frac{g}{\sqrt{2}} \overline{\mathbf{L}_i} \gamma^\mu (\tau_+ W_\mu^+ + \tau_- W_\mu^-) \mathbf{L}_l \\ &= -\frac{g}{\sqrt{2}} (\overline{\nu_L} \gamma^\mu e_L W_\mu^+ + \overline{e_L} \gamma^\mu \nu_L W_\mu^-) + \mu, \tau \text{ terms} \\ &= -\frac{g}{2\sqrt{2}} (\overline{\nu} \gamma^\mu (1 - \gamma^5) e W_\mu^+ + \overline{e} \gamma^\mu (1 - \gamma^5) \nu W_\mu^-) + \mu, \tau \text{ terms} \end{aligned} \qquad (1.1)$$

where ν, e, and $W^\pm$ are respectively the neutrino, electron, and charged intermediate boson fields, and g characterises the strength of the coupling. The operators τ_+ and τ_- operate in doublet space and have the explicit form

$$\tau_+ = \begin{pmatrix} 0 & 1 \\ 0 & 0 \end{pmatrix} \qquad \tau_- = \begin{pmatrix} 0 & 0 \\ 1 & 0 \end{pmatrix} .$$

In terms of the 2×2 Pauli matrices τ_i they are given by $\frac{1}{2}(\tau_1 \pm i\tau_2)$, where

$$\tau_1 = \begin{pmatrix} 0 & 1 \\ 1 & 0 \end{pmatrix} \qquad \tau_2 = \begin{pmatrix} 0 & -i \\ i & 0 \end{pmatrix} \qquad \tau_3 = \begin{pmatrix} 1 & 0 \\ 0 & -1 \end{pmatrix} .$$

The 4×4 Dirac matrices γ^μ and γ^5 satisfy the relations

$$\{\gamma^\mu, \gamma^\nu\} = 2g^{\mu\nu} \qquad \{\gamma^5, \gamma^\nu\} = 0 \qquad \mu, \nu = 0, 1, 2, 3. \qquad (1.2)$$

The adjoint spinor, $\overline{\psi}$ is defined as $\overline{\psi} = \psi^\dagger \gamma^\circ$.

In the quark sector, the situation is complicated by the fact that the weak interaction quark eigenstates q_i' are not the same as the quark mass eigenstates q_i, but are related by a unitary transformation. By convention

the u, c, and t quarks are considered unmixed, and the entire mixing is parametrised in terms of the *Cabibbo-Kobayashi-Maskawa matrix*, a 3×3 unitary matrix V operating on the d, s, and b quarks:

$$\begin{pmatrix} d' \\ s' \\ b' \end{pmatrix} = \begin{pmatrix} V_{ud} & V_{us} & V_{ub} \\ V_{cd} & V_{cs} & V_{cb} \\ V_{td} & V_{ts} & V_{tb} \end{pmatrix} \begin{pmatrix} d \\ s \\ b \end{pmatrix} .$$

This mixing allows charged-current (but not neutral-current) transitions between different families to occur. Assuming three generations and using the unitarity constraint, the magnitude of the elements of V lie in the range (90% confidence) [1]:

$$V = \begin{pmatrix} 0.9745 - 0.9757 & 0.219 - 0.224 & 0.002 - 0.005 \\ 0.218 - 0.224 & 0.9736 - 0.9750 & 0.036 - 0.046 \\ 0.004 - 0.014 & 0.034 - 0.046 & 0.9989 - 0.9993 \end{pmatrix} . \qquad (1.3)$$

Taking into account these rotations, the quark sector Lagrangian is given by

$$\begin{aligned} \mathcal{L}_{quark} &= -\frac{gV_{ij}}{2\sqrt{2}} \left[\overline{u_i} \gamma^\mu (1 - \gamma^5) d_j W_\mu^+ + \overline{d_j} \gamma^\mu (1 - \gamma^5) u_i W_\mu^- \right] \\ &= -\frac{g}{2\sqrt{2}} \left[V_{ud} \overline{u} \gamma^\mu (1 - \gamma^5) d W_\mu^+ + V_{ud} \overline{d} \gamma^\mu (1 - \gamma^5) u W_\mu^- \right. \\ &\quad \left. + V_{us} \overline{u} \gamma^\mu (1 - \gamma^5) s W_\mu^+ + V_{us} \overline{s} \gamma^\mu (1 - \gamma^5) u W_\mu^- + \dots \right] \end{aligned} \qquad (1.4)$$

where the u_i and d_j respectively represent sums over up and down type quarks.

Each of the lepton and quark weak Lagrangians have a common "V-A" structure,

$$\overline{\psi} \gamma^\mu (1 - \gamma^5) \psi = \overline{\psi} \gamma^\mu \psi - \overline{\psi} \gamma^\mu \gamma^5 \psi. \qquad (1.5)$$

All known weak processes have been found to respect this form of interaction. The first and second terms transform respectively as vector (V) and axial vector (A) under Lorentz transformations. This V-A form ensures that only left-handed (right-handed) particles (antiparticles) participate in weak interactions. This follows from the definition of right- and left-handed particles,

$$\psi = \left[\frac{(1 + \gamma^5)}{2} + \frac{(1 - \gamma^5)}{2} \right] \psi = \frac{(1 + \gamma^5)}{2} \psi + \frac{(1 - \gamma^5)}{2} \psi = \psi_R + \psi_L, \qquad (1.6)$$

so that with the help of 1.2 and the identity $(1 - \gamma^5)(1 - \gamma^5)/2 = 1 - \gamma^5$, the weak Lagrangian can be rewritten as

$$
\begin{aligned}
\overline{\psi}\gamma^\mu(1 - \gamma^5)\psi &= \overline{\psi}\gamma^\mu(1 - \gamma^5)\frac{(1 - \gamma^5)}{2}\psi \\
&= \overline{\psi}(1 + \gamma^5)\gamma^\mu\frac{(1 - \gamma^5)}{2}\psi \\
&= \psi^\dagger(1 - \gamma^5)\gamma^\circ\gamma^\mu\psi_L \\
&= [(1 - \gamma^5)\psi]^\dagger\gamma^\circ\gamma^\mu\psi_L \\
&= 2\overline{\psi_L}\gamma^\mu\psi_L.
\end{aligned}
\tag{1.7}
$$

The two particle sectors can be combined in a convenient form in order to connect with the current-current effective Fermi theory:

$$
\mathcal{L}_{cc} = \frac{g}{\sqrt{2}}(J^\mu W^+_\mu + J^{\mu\dagger}W^-_\mu)
$$

where the charged current J^μ is given by

$$
J^\mu = \overline{\nu_e}\gamma^\mu\frac{1}{2}(1 - \gamma^5)e + \overline{u}\gamma^\mu\frac{1}{2}(1 - \gamma^5)d' + \dots
\tag{1.8}
$$

and d' etc. provide the mixing of the quark mass states (see next section),

$$
d' = dV_{ud} + sV_{us} + bV_{ub}.
$$

This gives the coupling of charged currents to the vector bosons. The decay of a W produces another current, and the Lagrangian for charged current weak decays is given by

$$
\mathcal{L}_{cc} = \frac{g^2}{2}J^\mu\left(\frac{g_{\mu\nu} - q_\mu q_\nu/M_W^2}{q^2 - M_W^2}\right)J^{\nu\dagger},
$$

where the expression within parentheses is the boson propagator and q its four momentum. At low energies, the momentum transfer q^2 is much smaller than M_W^2 and therefore the propagator becomes simply $g_{\mu\nu}/M_W^2$ and yields the well-known phenomenological Fermi interaction,

$$
\mathcal{L}_{Fermi} = -\frac{4G_F}{\sqrt{2}}J^\mu J^\dagger_\mu,
\tag{1.9}
$$

with

$$
\frac{g^2}{2M_W^2} = \frac{4G_F}{\sqrt{2}}.
\tag{1.10}
$$

The above effective Lagrangian is quite satisfactory for practical τ physics. To see this, consider that the largest possible momentum transfer in τ decays is m_τ^2 ($\tau \to W\nu_\tau$ with W produced at rest in the tau rest frame) and so

$$
\frac{q^2_{max}}{M_W^2} = \frac{m_\tau^2}{M_W^2} \simeq 0.0005.
$$

After the invariant amplitude is squared, this is a correction of the order of 0.1% [7]

1.3.2   QCD

The strong force is responsible for binding quarks into hadronic states of mesons and baryons. The valence quark configuration of the mesons is of the form $q\overline{q}$, while that of the baryons is qqq. (The situation is, of course, much more messy than this because the valence quark configuration is embedded in what can aptly be described as a "virtual sea" of fluctuating $q\overline{q}$ and gluonic states, as allowed by the uncertainty principle.) These appear to be the only quark combinations permitted by nature. This has been accounted for through colour theory, or quantum chromodynamics (QCD), by postulating the existence of a new quantum number called colour. According to this hypothesis, each quark carries one of three possible colours, red, green or blue, while the mediators of the strong force, the gluons, also carry colour and so interact with each other in a complex manner. The three quark colour fields form a colour triplet; the strong interactions are invariant under local $SU(3)$ transformations of these fields. Colour theory stipulates that only colour singlets are allowed in nature, i.e., only colourless states are possible. Meson states are thus formed from a quark and antiquark of the same colour, while baryon states are formed from three quarks each of a different colour.

Because an isolated quark is a member of a colour triplet it cannot exist alone, and indeed free quarks have never been observed. All attempts to isolate quarks from their hadronic states result in the extraction of quark-antiquark pairs from the vacuum in order to form colour singlets. This is a

direct consequence of the nature of the strong coupling constant, α_S. Unlike the QED coupling constant, α_S grows as the interquark distance widens, increasing the force between quarks and confining them within the hadronic state. If the interaction energy is sufficient, it becomes possible to produce real quark-antiquark pairs from the vacuum allowing the more energetically favourable process of fragmentation to take place. The original quarks then combine with the new $q\bar{q}$ pairs to form colourless hadronic states.

Although QCD has been a very successful theory, it has not demonstrated the widespread applicability of QED. This is because the small electromagnetic coupling allows one to do perturbation theory and calculate as accurately as necessary, while the strong interaction coupling constant is much larger and exhibits a dramatic increase in strength at large distances. In this limit, lacking the aid of perturbation theory, there is no satisfactory way to calculate. At the other limit of very small distance, the coupling constant tends towards zero and the quarks, although confined within hadronic states, are effectively free (asymptotic freedom). It is only in this region that perturbation theory can be applied with any reliability. Therefore, QCD is currently a theory of limited applicability.

Mesons and baryons can be grouped very naturally into singlets, octets and decuplets, representations of the symmetry group $SU(3)$. It was this $SU(3)$ structure that eventually led Gell-Mann and Zweig to postulate the existence of a quark triplet as a more fundamental set of particles [8]. The three quarks u, d, and s combine to form all the known low mass hadrons. The $SU(3)$ symmetry is then the invariance of the strong interaction under unitary transformations of these three quark fields. (Note that this global symmetry has no connection with the local $SU(3)$ colour symmetry responsible for the strong interaction.) The symmetry is not perfect, however, owing to the mass differences between the u, d, and s quarks. Indeed, the current masses given in Table 1.1 differ greatly and it would appear that the $SU(3)$ and even the $SU(2)$ isospin symmetries should be badly broken. This is in fact not the case: isospin symmetry holds at the $1-2\%$ level while $SU(3)$ is good at the $15-20\%$ level. The real reason that these symmetries hold so well is that all the quark masses are small compared to the hadronic quark

interaction energies which are at least of the order of $\Lambda_C \simeq 0.2 - 0.3\,\mathrm{GeV}$ [9]. In this energy range, the masses of the u and d quarks are negligible leading to an almost exact isospin symmetry while the larger s quark mass yields a more approximate $SU(3)$ symmetry. The masses of the c, b, and t quarks are clearly much too big for the larger $SU(4)$ etc. symmetries to be exhibited.

The $SU(3)$ symmetry can be displayed by arranging the low-lying hadrons according to their isospin projection I_3 and strangeness S quantum number (Figure. 1.1). Each horizontal row is a multiplet of the isospin sub-
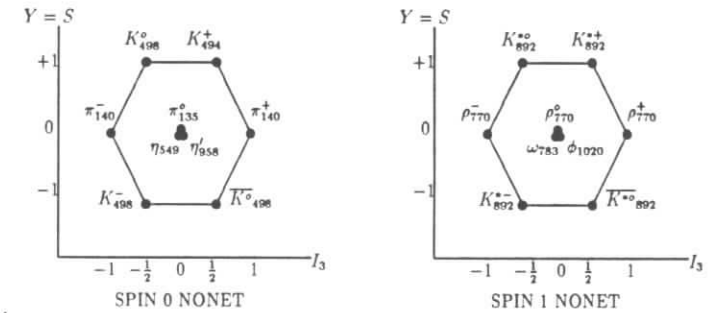
Figure 1.1: Multiplet structure exhibited by the lowest lying spin-0 and spin-1 mesons.

group, while the vertical scale represents different degrees of strangeness. The masses in a given isospin multiplet are all very similar indicating the near degeneracy of the u and d quarks. Each location in a multiplet represents a different possible particle state, specified by the quantum numbers S and I_3. The total isospin I is also a good quantum number, but this is not displayed in the diagram. For example, although the ω and ρ^o appear to occupy the same position, the former has total isospin I=0 while the latter has I=1. This distinguishes them from each other.

1.3.3 e^+e^- Collisions

Electron-positron collisions provide a very clean method for high energy particle production. In contrast to proton-proton and proton-antiproton colli-

sions, where the parton momenta are not known, the energy of the interaction can be fixed quite accurately. In addition, electrons being point-like particles, the number of possible types of interactions is limited and all background processes are fairly well understood from electroweak theory. The proton, along with three valence quarks, contains a sea of virtual gluons and $q\bar{q}$ pairs making it difficult to isolate the desired processes.

There are two types of processes that can occur in e^+e^- collisions: annihilation and scattering. Those interactions which do not involve annihilation are Bhabha events (where a single virtual photon is exchanged between electron and positron) and $\gamma\gamma$ events (where virtual photons emitted from the beam particles collide). Annihilation of the original beam particles produces fermion-antifermion pairs of leptons or quarks.

There are two possible annihilation channels for electron-positron collisions. These are to a virtual photon ($J^P = 1^-$) or a virtual Z ($J^P = 1^-$ or 1^+). The Z being very massive, at the energy of the Υ resonances this channel is suppressed by the factor M_Z^2 in the propagator and cannot compete with the photon channel. The first order differential cross section for annihilation into energetic fermion-antifermion pairs with electric charge Q_f and velocity $\beta = \frac{v}{c}$ is given by [1]

$$\frac{d\sigma(e^+e^- \to f\bar{f})}{d\Omega} = \frac{\alpha^2}{4s}\beta[1 + \cos^2\theta + (1 - \beta^2)\sin^2\theta]Q_f^2 \qquad (1.11)$$

where θ is the angle the produced particles have with respect to the incoming beam axis, and s is the square of the centre-of-mass energy. An integration over the solid angle gives

$$\sigma(e^+e^- \to f\bar{f}) = \frac{4\pi\alpha^2}{3s}Q_f^2[\frac{\beta(3 - \beta^2)}{2}] = \frac{86.8Q_f^2}{s(\text{GeV}^2)}[\frac{\beta(3 - \beta^2)}{2}] \text{ nb.} \qquad (1.12)$$

For $q\bar{q}$ production, QCD corrections to second order in α_s introduce a factor

$$[1 + \frac{\alpha_S(s)}{\pi} + 1.41(\frac{\alpha_S(s)}{\pi})^2]$$

if the quarks are assumed massless. The hadronic cross section expression applies only at energies well away from resonance regions. A summation over

all quark pairs not including $b\bar{b}$ and $t\bar{t}$ yields an approximate expression for the continuum hadronic cross section at 10.55GeV. Using a value $\alpha_S = 0.16$, and summing over quark colours gives

$$\sigma(e^+e^- \to \text{hadrons}) = \frac{86.8}{111} \cdot 1.05 \cdot [3(\frac{2}{3})^2 + 3(\frac{1}{3})^2 + 3(\frac{1}{3})^2 + 3(\frac{2}{3})^2] = 2.7\text{nb.}$$

In comparison, the channels e^+e^-, $\mu^+\mu^-$ and $\tau^+\tau^-$ have cross sections of about 0.8nb, therefore from this crude calculation, the fraction of the annihilation cross section resulting in tau pairs is expected to be of the order of 15%. Of course, contributions from beam-wall, beam-gas, two-photon, and t-channel $e^+e^- \to e^+e^-$ events drive the fraction of tau pairs produced in the ARGUS detector far lower than this, and the fraction is lower still when collecting data on the Υ resonances, where $b\bar{b}$ processes are enhanced.

Chapter 2

Tau Physics

2.1 Introduction and Historical Overview

In 1973, Kobayashi and Maskawa [10] proposed a mechanism for CP violation which involved the hypothesis of a third generation of quarks and leptons. At the time there was then no experimental evidence for another generation. Glashow, Iliopoulos, and Maiani had already suggested the existence of a fourth quark to account for the non-observation of flavour-changing neutral currents [11], and its discovery in 1974 [12] by way of the J/Ψ made the theory nicely symmetric and elegant. There was no need for a third generation of particles. In 1975, however, evidence for a new heavy lepton, the tau, began to accumulate. In what follows, a brief historical account of the discovery of the tau lepton is provided.

The tau was in fact sought before there was any real reason to believe it existed. In the early seventies, efforts to understand the connection between the muon and the electron were turning up little in the way of an explanation. In all respects the muon appears to be nothing more than a higher mass repetition of the electron, prompting Rabi to utter the now famous line, "Who ordered that?". The idea arose that perhaps if other higher mass versions of these particles existed then through studying them a new understanding of the origin of lepton differences might be forthcoming. There was some theoretical basis for expecting these heavier particles at the time, and this lent credibility to searching for them. It was in this period that the term

"sequential lepton" was coined, and that Y.Tsai wrote his seminal paper on the production and decay of heavy leptons [13].

In 1971, the proposal for the Mark I experiment on the SPEAR storage ring at SLAC was submitted, with heavy lepton searches the very last item on the proposed agenda. This was not the first time such a proposal had been made - two experiments at the ADONE storage ring were performing searches while SPEAR and MARK I were being built, but the energy of the storage ring was below the threshold for tau pair production. Data taking at SPEAR began in 1973, with the first evidence for anomalous $e - \mu$ events observed in 1974. These events have exactly two oppositely charged tracks, consistent with being an electron and a muon, and no photons, a very distinctive signature for tau decays. However, hadron misidentification rates were very high (of the order 20% for both electrons and muons) and the detector did not cover the complete solid angle, so further efforts were required to convince scientists both inside and outside of the collaboration that the events were genuinely from a heavy lepton source. It wasn't until late 1975 that the first claim of evidence for a new heavy lepton was published [14]. In that paper, the heavy lepton was referred to as the U, and not named the tau (first letter of the greek word for *third*, $\tau\rho\iota\tau o\nu$) until later.

There followed in the years 1976 to 1978 a plethora of attempts to strengthen or weaken the Mark I claim. The skepticism surrounding the claim was primarily motivated by there being no need in the theory for a third lepton. As to whether the anomalous $e - \mu$ events were indeed the result of heavy lepton production, rather than some other mechanism, a favourite criticism of the time was that inclusive hadronic one-prong production, expected to have twice the rate of the leptonic channel, had not been observed. In particular, the exclusive channel $\tau \to \pi\nu$ was supposed to occur at the 10% level but was at one point measured by DASP at DORIS to be less than 2%. Through the efforts of several experiments all these problems were eventually addressed. $e -$ hadron and $\mu -$ hadron inclusive rates were shown to be consistent with heavy lepton production and the decay $\tau \to \pi\nu$ measured at about 8%, By the end of 1978, the existence of the tau was considered firmly established.

Since that time the properties of the tau lepton have been extensively

studied. Being the only lepton heavy enough to decay into hadrons, it was hoped that the tau would provide a window to new physics and indeed for a long time both the *1-prong deficit problem* (or "completeness" problem) and the *universality problem* (or "consistency" problem), discussed later in the chapter, had the high energy physics community scrambling to account for what appeared to be significant deviations from expectation. It now appears, however, that the tau lepton does in fact behave as is predicted.

In what follows, the theory of the tau lepton will be described assuming it is a standard model sequential lepton, comparing to experiment where appropriate. The physics of the tau is a broad field. Naturally not all aspects are relevant to this thesis, and therefore the author has taken the liberty of addressing only a subset of what is known about it.

2.2 Tau Production

Tau production and decay can occur in fixed target experiments but the cross section is small and the process is usually embedded among other more abundant types of particle production. A much cleaner and more productive environment is that of e^+e- colliders. If the tau is merely a heavy electron it should couple electromagnetically to the photon and the Z^o. Thus pairs of tau leptons can be produced via the annihilation process

$$e^+e^- \to \gamma^*, Z^* \to \tau^+\tau^-,$$

and its radiative cousins (Figure 2.1). Many experiments have successfully
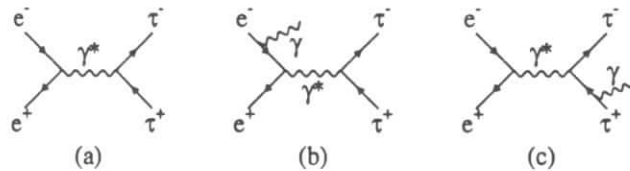
Figure 2.1: Feynman diagrams for tau production including lowest order initial and final state radiative decay diagrams.

contributed to our understanding of the tau lepton in this environment. The

most recent are the high energy LEP experiments, the low energy experiments CLEO and ARGUS, and the threshold experiment BES.

At ARGUS energies, the contribution from the Z pole can be safely neglected and the cross section for non-radiative tau production at centre-of-mass energy $\sqrt{s}$ is calculated from the differential cross section for point like fermion production $e^+e^- \to f\bar{f}$ given by Equation 1.11. Using $\sqrt{s} = 10.55 GeV$ (the average centre-of-mass energy of the data used in this thesis) and $m_\tau = 1.777 GeV/c^2$ yields $\sigma = 0.776$nb. However, initial state radiation increases the cross section to 0.916nb.

2.3 Mass and Lifetime of the Tau

The current world average of the tau mass is $m_\tau = (1.7770 \pm 0.0003) \text{GeV}/c^2$ [1]. Therefore, it is the only lepton capable of decaying into hadrons, providing us with a unique QCD testing ground. Only decays into mesons containing u, d, and s valence quarks are kinematically allowed because 1) baryons would have to be produced in pairs to conserve baryon number, yet the lowest-lying baryon-antibaryon system, $p\bar{p}$, has a mass $2m_p = 1.876 \text{GeV}/c^2 > m_\tau$; and 2) the lowest-lying charmed meson, the D^o, has a mass of $m_{D^o} = 1.865 \text{GeV}/c^2 > m_\tau$.

The current world average value for the tau lifetime is $\tau_\tau = (291 \pm 1.5)$fs [1], corresponding to a mean tau flight path of about 250 microns at ARGUS energies. The lifetime values for some individual measurements are provided in Chapter 3, along with a detailed explanation of the various lifetime measuring methods currently in use.

2.4 Tau Decay

Using Equations 1.9 and 1.8, the weak charged-current Lagrangian for τ^- decay can be written explicitly as

$$\mathcal{L}_\tau = -\frac{G_F}{\sqrt{2}} \left(\quad \left[\overline{\nu_\tau}\gamma^\mu(1-\gamma^5)\tau\right] \left[\overline{e}\gamma^\mu(1-\gamma^5)\nu_e\right] \right.$$
$$\left. + \quad \left[\overline{\nu_\tau}\gamma^\mu(1-\gamma^5)\tau\right] \left[\overline{\mu}\gamma^\mu(1-\gamma^5)\nu_\mu\right] \right.$$

$$+V_{ud}\left[\overline{\nu_\tau}\gamma^\mu(1-\gamma^5)\tau\right]\left[\overline{d}\gamma^\mu(1-\gamma^5)u\right]$$
$$+V_{us}\left[\overline{\nu_\tau}\gamma^\mu(1-\gamma^5)\tau\right]\left[\overline{s}\gamma^\mu(1-\gamma^5)u\right]\qquad). \qquad (2.1)$$

In the order they are written, the terms correspond to decay into electrons, muons, non-strange mesons, and strange mesons, respectively. Figure 2.2 shows the Feynman tree diagrams for these terms.
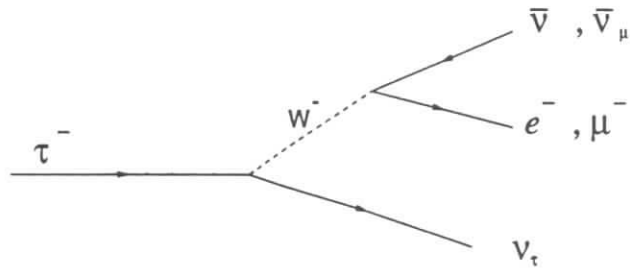
a) Leptonic tau decay
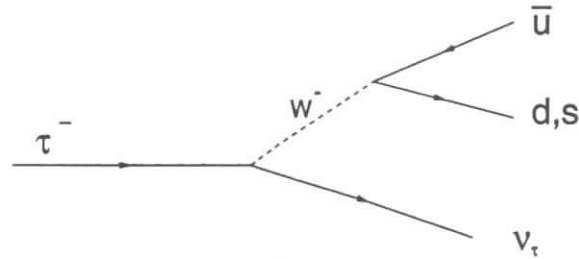
b) Hadronic tau decay

Figure 2.2: Feynman diagrams for leptonic and hadronic tau decay.

Table 2.1 lists the experimentally determined branching ratios [1] of several tau decay channels. These were derived from a multi-parameter fit to measurements by many experiments and represent the best information

τ^- mode	Exp. value
$e^-\overline{\nu}_e\nu_\tau$	$(17.83 \pm 0.08)\%$
$\mu^-\overline{\nu}_\mu\nu_\tau$	$(17.35 \pm 0.10)\%$
$\pi^-\nu_\tau$	$(11.31 \pm 0.15)\%$
$K^-\nu_\tau$	$(0.71 \pm 0.05)\%$
$\pi^-\pi^\circ\nu_\tau$	$(25.24 \pm 0.16)\%$
$K^-\pi^\circ\nu_\tau$	$(0.52 \pm 0.05)\%$
$\pi^-2\pi^\circ\nu_\tau(ex.K^\circ)$	$(9.27 \pm 0.14)\%$
$K^-2\pi^\circ\nu_\tau(ex.K^\circ)$	$(0.08 \pm 0.03)\%$
$\pi^-3\pi^\circ\nu_\tau(ex.K^\circ)$	$(1.14 \pm 0.14)\%$
$K^-3\pi^\circ\nu_\tau(ex.K^\circ)$	$(0.05 \pm 0.05)\%$
$h^-4\pi^\circ\nu_\tau(ex.K^\circ,\eta)$	$(0.12 \pm 0.06)\%$
$\pi^-\overline{K}^\circ\nu_\tau$	$(0.77 \pm 0.08)\%$
$K^-K^\circ\nu_\tau$	$(0.16 \pm 0.03)\%$
$\pi^-\overline{K}^\circ\pi^\circ\nu_\tau$	$(0.41 \pm 0.06)\%$
$K^-K^\circ\pi^\circ\nu_\tau$	$(0.14 \pm 0.03)\%$
$\pi^-\overline{K}^\circ K^\circ\nu_\tau$	$(0.10 \pm 0.02)\%$
$h^-h^-h^+\nu_\tau(ex.\overline{K}^\circ,\omega)$	$(9.44 \pm 0.10)\%$
$h^-h^-h^+\pi^\circ\nu_\tau(ex.\overline{K}^\circ,\omega)$	$(2.55 \pm 0.09)\%$
$h^-h^-h^+2\pi^\circ\nu_\tau(ex.\overline{K}^\circ,\omega,\eta)$	$(0.10 \pm 0.04)\%$
$h^-h^-h^+ \geq 3\pi^\circ\nu_\tau$	$(0.11 \pm 0.06)\%$
$3h^-2h^+\nu_\tau(ex.\overline{K}^\circ)$	$(0.08 \pm 0.01)\%$
$3h^-2h^+\pi^\circ\nu_\tau(ex.\overline{K}^\circ)$	$(0.02 \pm 0.01)\%$
$\eta\pi^-\pi^\circ\nu_\tau$	$(0.17 \pm 0.03)\%$
$h^-\omega\nu_\tau$	$(1.91 \pm 0.09)\%$
$h^-\omega\pi^\circ\nu_\tau$	$(0.04 \pm 0.06)\%$

Table 2.1: Experimental values of the known tau lepton branching ratios. The symbol h denotes $\pi^\pm$ or $K^\pm$, and "ex" means that indicated daughter particles do not contribute to the channel.

currently available on tau branching ratios. The corresponding topological branching ratios for decays to one, three, and five charged particles (termed one-prong, three-prong and five-prong decays) are $BR^1 = (84.96 \pm 0.14)\%$, $BR^3 = (14.91 \pm 0.14)\%$, and $BR^5 = (0.097 \pm 0.007)\%$, implying that tau pair production is almost completely saturated by the 1-1 (72.2%) and 1-3 (25.3%) event topologies.

The theoretical decay widths predicted by the Lagrangian 2.1 are in agreement with experiment. In the remainder of this section, a more detailed description of the theory is provided.

2.4.1 Leptonic Tau Decay

In contrast to hadronic tau decays, discussed in section 2.4.2, the rates for $\tau \rightarrow \ell \overline{\nu}_\ell \nu_\tau$, where ℓ represents an electron or muon, can be derived unambiguously in the context of the standard model. The lowest order matrix element follows from Equation 2.1:

$$\mathcal{M} = \frac{G_F}{\sqrt{2}}[\overline{u}(\nu_\tau)\gamma^\mu(1-\gamma^5)u(\tau)][\overline{u}(\ell)\gamma^\mu(1-\gamma^5)v(\nu_\ell)], \qquad (2.2)$$

where $u(\nu_\tau)$, $u(\tau)$, $\overline{u}(\ell)$, and $v(\nu_\ell)$ are the appropriate Dirac spinors for the four particles entering the interaction. The differential decay rate is given by the Fermi Golden rule [1],

$$d\Gamma = \frac{(2\pi)^4}{m_\tau}\overline{|\mathcal{M}|^2}d\Phi_3, \qquad (2.3)$$

where $d\Phi_3$ represents the three-body phase-space factor. Integrating over all of phase-space yields

$$\Gamma(\tau \rightarrow \ell \overline{\nu}_\ell \nu_\tau) = \frac{G_F^2 m_\tau^5}{192\pi^3}F(x)$$

where $F(x) = 1 - 8x + 8x^2 - x^4 - 12x^2 \ln x$ and $x = (m_\ell/m_\tau)^2$. For decay to electrons $F(x)$ is unity to better than 10^{-6}, well below current experimental sensitivity to the decay rate. For decay to muons however this correction is much larger ($F(x) \approx 0.973$) and cannot be neglected. Including W mass effects and radiative corrections the decay rate becomes

$$\Gamma(\tau \rightarrow \ell \overline{\nu}_\ell \nu_\tau) = \frac{G_F^2 m_\tau^5}{192\pi^3}F(x)\left[1 + \frac{3}{5}\frac{m_\tau^2}{M_W^2}\right]\left[1 + \frac{\alpha(m_\tau)}{2\pi}(\frac{25}{4} - \pi^2)\right]. \qquad (2.4)$$

The first and second bracketed factors contribute changes of +.029% and -.43% respectively to the uncorrected rate ($\alpha(m_\tau) = 1/133.3$).

2.4.2 Hadronic Tau Decay

An exact calculation of the hadronic decay rates of the tau lepton is hampered by the non-perturbative nature of QCD. Although at the quark level the process is equivalent to leptonic decay, the problem is that these bare quarks are not observable. Instead, through the strong interaction processes of gluon exchange and quark pair production from the vacuum they become dressed up into hadrons. While QCD in principle describes the manner in which these hadrons arise, the theory remains intractable from a calculational perspective. Nevertheless the situation is not as bad, for example, as in heavy meson hadronic decay where both the original and final states contain quarks and the QCD dynamics is more complicated. In hadronic tau decays the decaying W produced in the weak interaction process decays into quarks which hadronise independently of the $\tau \rightarrow \nu_\tau$ current, i.e. the invariant amplitude for the decay can be legitimately decomposed into independent leptonic and hadronic parts. Explicitly,

$$\mathcal{M} = \frac{G_F}{\sqrt{2}}\mathcal{L}^\mu\mathcal{H}_\mu \qquad (2.5)$$

$$\mathcal{L}^\mu = <\nu|J^\mu|\tau> = <\nu|\overline{\psi}(1-\gamma_5)\gamma^\mu\psi|\tau> \qquad (2.6)$$

$$\mathcal{H}_\mu = <h|J_\mu|0> = <h|\overline{\psi}(1-\gamma_5)\gamma_\mu\psi|0> \qquad (2.7)$$

where h represents the final state hadronic system. The leptonic part is easily calculable given the point-like nature of the tau and its neutrino. The hadronic part is much more difficult to evaluate given that the currents are quark currents and the final hadronic state is not a set of free quarks but rather a system of one or more mesons. Nevertheless $\mathcal{H}_\mu$ can be simplified using various properties of the weak current.

G-Parity

$\mathcal{H}_\mu$ can be rewritten in terms of the (Lorentz) vector and axial vector currents V_μ and A_μ,

$$\mathcal{H}_\mu = V_\mu - A_\mu \tag{2.8}$$

$$= <h|\bar{\psi}\gamma_\mu\psi|0> - <h|\bar{\psi}\gamma_5\gamma_\mu\psi|0> . \tag{2.9}$$

It can be shown [15] that the vector and axial-vector currents are even and odd respectively under G-parity. Recall that G-parity is the product of a rotation by π about the y-axis in isospin space and charge conjugation,

$$G = Ce^{i\pi\tau_2}. \tag{2.10}$$

It is useful in that it allows a net charged system of pions to be an eigenstate, in a loose sense, of C: the rotation in I-space flips the sign of the charge of the system before the C operation flips it back. Because the vacuum is G even the vector (axial-vector) current alone contributes in processes having final state $G = +1$ ($G = -1$). Because the pion has odd G-parity, the vector current is responsible for final states composed entirely of an even number of pions and the axial current responsible for those states with an odd number of pions. Thus the channels $\tau^- \to \rho^-\nu_\tau$ and $\tau^- \to \pi^+\pi^-\pi^-\pi^0\nu_\tau$, for example, are mediated by the vector current, whereas $\tau^- \to \pi^-\nu_\tau$ and $\tau^- \to \pi^+\pi^-\pi^-\nu_\tau$ are mediated by the axial-vector current. Currents which violate these conditions are termed *second-class currents* and can only appear at the level at which isospin is violated.

Conserved Vector Current Hypothesis

The electromagnetic interaction

$$\mathcal{L}_{em} = eQ_i\bar{\psi}\gamma^\mu\psi A_\mu \tag{2.11}$$

leads to matrix elements of the form $< f|J^\mu_{em}|i >$ with electromagnetic current

$$J^\mu_{em} = eQ_i\bar{\psi}\gamma^\mu\psi,$$

which, if only the quark $u - d$ sector is considered, is

$$J^\mu_{em} = e\{\frac{2}{3}\bar{u}\gamma^\mu u - \frac{1}{3}\bar{d}\gamma^\mu d\}.$$

It is instructive to recast this current in terms of the doublet

$$q = \begin{pmatrix} u \\ d \end{pmatrix}.$$

Noting that the constructions $\frac{1}{2}(I + \tau_3)$ and $\frac{1}{2}(I - \tau_3)$, where τ_3 is the third Pauli spin matrix given in section Section 1.3.1 and I is the 2×2 unit matrix, project out the upper and lower members of the q doublet, respectively, the current can be rewritten as

$$J^\mu_{em} = e\{\frac{2}{3}\bar{q}\gamma^\mu(\frac{I + \tau_3}{2})q - \frac{1}{3}\bar{q}\gamma^\mu(\frac{I - \tau_3}{2})q\} \tag{2.12}$$

$$= e\{\frac{1}{6}\bar{q}\gamma^\mu q + \frac{1}{2}\bar{q}\gamma^\mu\tau_3 q\}. \tag{2.13}$$

The first term is invariant under isospin rotations (iso-scalar) whereas the second term transforms as the third component of a vector (iso-vector). The other two components are given by $\bar{q}\gamma^\mu\tau_\pm q$ and when written out explicitly can be identified as the charge raising and lowering vector weak currents, $v^+ = \frac{1}{\sqrt{2}}\bar{u}\gamma^\mu d$ and $v^- = \frac{1}{\sqrt{2}}\bar{d}\gamma^\mu u$. The *conserved vector current* (CVC) hypothesis states that because the strong interaction conserves isospin, matrix elements of the three components of the isovector current must be the same even though the quarks are bound into hadrons and strong force effects come into play. This allows the evaluation of matrix elements involving $v^\pm$ through direct comparison with the production of $I = 1$ final states in e^+e^- collisions. (See below.)

Partially Conserved Axial Vector Current

There is no corresponding identification for the axial vector current. However, in the limit of zero quark mass, the QCD Lagrangian turns out to be *chiral invariant*, i.e. invariant under independent rotations of left- and right-handed quark fields [9]. This leads to conserved axial currents of the form

$$A^\mu = \bar{q}\gamma^\mu\gamma^5\tau_3 q. \tag{2.14}$$

in addition to vector currents like those above. In reality the quarks are not massless and the symmetry is broken at the level of the pion mass, leading instead to a *partially conserved axial current* (PCAC). In computing matrix elements involving the axial current, assumptions as to how chiral symmetry is broken need to be made. The Weinberg Sum Rules [16] and Das-Mathur-Okubo [17] relations facilitate the decay rate calculations, which are typically accurate to about 10%.

2.4.3 General Expression for Tau Hadronic Decay Widths

The general expression for tau decay into hadrons can be derived starting from Equations 2.1 and 2.7 [13]:

$$\Gamma(\tau \to \text{hadrons} + \nu_\tau) = \frac{G_f^2}{32\pi^2 m_\tau^3} \int_0^{m_\tau^2} dq^2 (m_\tau^2 - q^2)^2 \times \qquad (2.15)$$
$$\left[V_{ud}^2 \left\{ (m_\tau^2 + 2q^2)^2)[v_1(q^2) + a_1(q^2)] + m_\tau^2 a_o(q^2) \right\} \right.$$
$$\left. + V_{us}^2 \left\{ (m_\tau^2 + 2q^2)^2)[v_1^s(q^2) + a_1^s(q^2)] + m_\tau^2 [v_o^s(q^2) + a_o^s(q^2)] \right\} \right],$$

where the *spectral functions* v and a contain the information on how the quarks produced in the decay of the W hadronise into final states, and refer to vector and axial vector current couplings to the W, respectively. They are functions only of the momentum transfer to the hadronic system, $q^2 = (p_\tau - p_{\nu_\tau})^2$. The subscripts denote the spin J of the final state hadronic system, and the superscript s labels the final states of net strangeness. The absence of $v_o(q^2)$ in this expression is a consequence of CVC.

A few example applications of Equation 2.15 in calculating the rates of hadronic tau decays are provided here.

- $\tau^- \to \pi^-(K^-)\nu_\tau$ The pion has spin $J = 0$, negative G-parity, and zero strangeness, so the relevant spectral function here is $a_o(q^2)$, corresponding to the matrix element $< \pi(q)|A_\mu|0 >$. The pion has negative parity, therefore this must evaluate to a vector, the only one available being q_μ, the four-momentum of the pion produced in the decay. Therefore

$$< \pi(q)|A_\mu|0 >= f_\pi q_\mu \qquad (2.16)$$

where the *pion decay constant*, f_τ, can be evaluated through measurement of the decay $\pi \to \mu\nu_\mu$. The spectral function is given by [13]

$$a_o(q^2) = 2\pi f_\tau^2 \delta(q^2 - m_\tau^2) \qquad (2.17)$$

which upon substitution into Equation 2.15 yields

$$\Gamma(\tau^- \to \pi^- \nu_\tau) = \frac{G_f^2}{16\pi} f_\pi^2 |V_{ud}|^2 m_\tau^3 (1 - \frac{m_\pi^2}{m_\tau^2})^2. \qquad (2.18)$$

A similar expression for the $\tau^- \to K^- \nu_\tau$ decay rate can be derived by replacing the CKM matrix element V_{ud} with V_{us}, and the pion decay constant f_π with the *kaon decay constant* f_K.

- $\tau^- \to \pi^- \pi^o \nu_\tau$ In this case the G-parity of the final hadronic system is positive, the net strangeness zero, and the spin $J = 1$. The relevant spectral function is therefore $v_1(q^2)$. The form for this expression can be obtained from CVC by considering the electromagnetic process $e^+ e^- \to \rho^o \to \pi^+ \pi^-$. As noted earlier, CVC relates the isovector part of the electromagnetic current to weak charged hadronic current, so that [13]

$$v_1(q^2) = \frac{q^2 \sigma_{I=1}(e^+ e^- \to \pi^+ \pi^-)}{4\pi \alpha^2}, \qquad (2.19)$$

where α is the *fine structure constant*. The calculation of $\sigma_{I=1}$ is complicated by interference from the $I = 0$ channel, $e^+ e^- \to \omega \to \pi^+ \pi^-$, as well as excited ρ states. Corrected for these influences, the $e^+ e^-$ cross section yields an expression for $v_1(q^2)$ which can be used to calculate $\tau^- \to \pi^- \pi^o \nu_\tau$ via 2.15. Decays involving four or six pions, $\tau^- \to 4, 6\pi\nu_\tau$, also involve the spectral function $v_1(q^2)$, and can be calculated using $e^+ e^-$ annihilation data in a similar manner.

- $\tau^- \to \pi^+ \pi^- \pi^- \nu_\tau$ and $\tau^- \to \pi^- \pi^o \pi^o \nu_\tau$ These two decay modes are related by isospin conservation. To conserve G-parity they must proceed through the axial vector current. Therefore, CVC cannot be applied. ARGUS has found that the three-prong channel $\tau^- \to \pi^+ \pi^- \pi^- \nu_\tau$ is dominated by the $a_1(1260)$ resonance [18], decaying predominantly into $\rho^o \pi^-$. The width of this resonance is very large, and the uncertainty

in the width and shape complicates theoretical calculations and leads to varied predictions for the rate. Crude estimates based on PCAC or the Weinberg sum rules are derivable.

2.5 The Tau Neutrino

To respect lepton number conservation, all tau decays should produce a tau neutrino. Although the tau neutrino has not been directly observed, there are experiments planned which will attempt to do this. In any case, the nature of tau decays suggests the presence of a third neutrino, and experiments have been carried out which strongly favour this neutrino as being distinct from the electron or muon neutrinos [19]. All indications are that the tau behaves as a sequential lepton.

The current upper limit on the mass of the tau neutrino is $m_{\nu_\tau} < 24\text{MeV/c}^2$ at 90% confidence, set by ALEPH [20]. This only recently superceded the long-standing ARGUS value of $m_{\nu_\tau} < 31\text{MeV/c}^2$ [21]. Both measurements employ the endpoint in the invariant mass spectrum of the hadronic system in tau decays to derive the limit.

In this thesis, the tau neutrino is assumed to have zero mass.

2.6 Problems with the Tau

In the mid-1980s, there were indications that the tau might exhibit properties which could not be explained in the context of the standard model. Two different problems could be identified. The first concerned the possibility that the tau did not respect the hypothesis of a universal weak coupling constant, and the second that the tau might have exotic one-prong decay modes. These two issues are addressed in the remainder of this chapter.

2.6.1 Universality

Noting that the only difference between the decay channels $\mu \to e\overline{\nu}_e\nu_\mu$ and $\tau \to e\overline{\nu}_e\nu_\tau$ is the mass of the decaying particle, the rate for muon decay can

year	τ_τ (fs)	m_τ (MeV/c^2)	B_e (%)	g_τ/g_μ
1990	303 ± 8	1784.1 ± 3.4	$17.7 \pm .4$	$.967 \pm .018(1.8\sigma)$
1992	305.6 ± 6	1784.1 ± 3.4	$17.93 \pm .26$	$.969 \pm .013(2.4\sigma)$
1994	295.6 ± 3.1	$1777.1 \pm .45$	$18.1 \pm .181$	$.997 \pm .007(.4\sigma)$
1996	291.0 ± 1.5	$1777.0 \pm .275$	$17.83 \pm .080$	$1.000 \pm .003(.0\sigma)$

Table 2.2: Experimental values of the tau lifetime, mass, and electronic branching ratio for various years. An early indication of universality violation is no longer observed. See text.

be obtained immediately from Equation 2.4 by replacing the tau mass with the muon mass. Thus,

$$\Gamma(\mu \to e\overline{\nu}_e\nu_\mu) = \frac{G_F^2 m_\mu^5}{192\pi^3} F(\frac{m_e^2}{m_\mu^2}) \left[1 + \frac{3}{5}\frac{m_\mu^2}{M_W^2}\right] \left[1 + \frac{\alpha(m_\mu)}{2\pi}(\frac{25}{4} - \pi^2)\right]. \quad (2.20)$$

According to *universality*, the weak coupling constant g should have the same value for all weak interactions, e.g. $G_F = G_\mu = G_\tau$. Taking the ratio of Equation 2.4 (with $\ell = e$) and Equation 2.20, and using

$$\Gamma(\tau \to e) = \Gamma(\tau \to \text{all}) \cdot B_e = B_e \cdot \frac{\hbar}{\tau_\tau} \quad (2.21)$$

and

$$\Gamma(\mu \to e) = \Gamma(\mu \to \text{all}) = \frac{\hbar}{\tau_\mu}, \quad (2.22)$$

one finds

$$(\frac{G_\tau}{G_\mu})^2 = (\frac{g_\tau}{g_\mu})^2 = (\frac{m_\mu}{m_\tau})^5(\frac{\tau_\mu}{\tau_\tau}) \cdot Br(\tau \to e\overline{\nu}_e\nu_\tau) \cdot R, \quad (2.23)$$

where $R = .9996$ is the ratio of the tau and muon correction factors. The couplings g_e at each of the $e\nu_e W$ vertices cancel to yield this expression for g_τ/g_μ (see Equation 1.10). The right hand side of this equation involves quantities that can be measured independently of each other and therefore allow a direct test of universality. Table 2.2 lists the values of these quantities as they were known in each of the years 1990 [22], 1992 [23], 1994 [24], and 1996 [1], along with the values of g_τ/g_μ calculated according to Equation 2.23. The initial apparent deviation from unity in the coupling constant ratio is known as the universality problem or *consistency problem*. Together with the

one-prong deficit problem, described in the next section, this was cause for much excitement among the tau physics community because it suggested the existence of new physics. This spawned a wealth of new measurements of τ_τ, m_τ, and the tau leptonic branching ratios, the result being the disappearance of any universality problem. The principal player in this improvement [1] was a 2σ downward shift in the value of m_τ. The original world average was dominated by the DELCO measurement of 1978 [25] and only updated in 1992 by ARGUS [21], BES [26], and CLEO [27]. New measurements of the tau lifetime were also instrumental in improving the agreement. The need to resolve the universality puzzle has been the primary motivation for recent attempts to make a precise and accurate measurement of the tau lifetime.

2.6.2 One-prong Deficit Problem

Because the one-prong deficit problem, or *completeness* problem, is not directly relevant to an analysis of the tau lifetime, it will be given brief treatment here. It is included only for the sake of completeness.

The one-prong deficit problem was first noticed in the mid 1980s [28, 29] when comparing the inclusive topological one-prong tau branching ratio to the sum of individual branching ratios for the known exclusive one-prong channels. Data available from various experiments at the time were used to make the comparison; for those channels for which measurements were unavailable or poor the corresponding theoretical branching ratios were used. The exclusive channels were found not to saturate the observed total inclusive rate. Several possibilities for this deficit were considered:

- an underestimation of the statistical and/or systematic errors in some or all measurements;

- a faulty approach to combining the information from the various measurements;

---

[1] Admittedly, the restored experimental agreement in the coupling constants diminishes the likelihood of observing any new physics in this sector and in some sense may not be considered an improvement at all. Handles on new physics are difficult to come by these days!

- errors in the theoretical calculations; and

- the existence of tau decays in modes not predicted by the standard model.

The second item was a particular concern. It was difficult to take into account the correlations between the systematic errors in the various measurements. This was eventually circumvented by the CELLO collaboration in 1990 [30], which carried out a complete *global analysis* of all the one-prong branching ratios in their data, taking into account migrations. No deficit was observed. ALEPH confirmed this in 1992 with a similar analysis of their data [31], and recently updated their claim using a larger data sample [32]. Global analyses like these are now commonly accepted as being the best method available to resolve the one-prong deficit problem. Based on the information currently available, it would appear that the one-prong problem has been resolved, and that there is no need to invoke new physics to describe tau decays.

Chapter 3

Methods for Measuring the Tau Lifetime

Before describing in detail the various methods available for measuring the tau lifetime, some general comments are useful. All tau lifetime measurements to date have been made in the very clean environment of e^+e^- colliders with symmetric beams [1]. Because of the large bucket size the z position of the tau production vertex is poorly known on an event-by-event basis, making a three-dimensional analysis difficult. In addition, the tracking detectors of an experiment typically have a spatial resolution in the plane perpendicular to the beam line ($r - \phi$) far superior to that along the beam line (z). Therefore, it is no surprise that, except for the 3DIPS method (see below), all methods described below and the one dealt with in this thesis make use of decay lengths and impact parameters measured in the $r - \phi$ plane alone.

There are two main difficulties one must circumvent in order to measure the tau lifetime. First, the production point of the tau in e^+e^- collisions is unknown and must be approximated by the beam spot position. However, the beam envelope is often comparable in size to the decay length or impact parameter measured and contributes a non-negligible level of smearing to these quantities. This seriously compromises the statistical power of methods that rely on a knowledge of the production point. Second, because the decay of the tau is always accompanied by at least one (undetectable) neutrino it is impossible to reconstruct the direction of the tau (see the 3DIPS method below, however). This is in stark contrast to measurements of charm and

beauty mesons, where, by choosing decay channels in which all products are observable, the meson flight direction can be reconstructed. The flight direction contributes an invaluable constraint to any lifetime analysis and allows a more direct measurement of the particle's decay length.

To circumvent these difficulties several new methods have been developed, mostly through the efforts of the LEP collaborations. These methods greatly improve upon the traditional *decay length* (DL) and *classical impact parameter* (IP) methods. The *miss distance* (MD) and *impact parameter sum* (IPS) methods almost completely remove any dependence upon the beam spot, although they do not escape the smearing introduced by the unknown tau direction. The *momentum dependent impact parameter sum* (MIPS) method is a slightly more powerful version of the IPS method. The *impact parameter difference* (IPD) method has a reduced dependence upon the unknown tau flight direction but suffers badly from the smearing due to the unknown tau production point. Finally, in a class by itself, the *three-dimensional impact parameter sum* (3DIPS) method surmounts the tau flight direction difficulty through three-dimensional tracking, but can only be applied to hadronic tau decays.

A brief description of each of these methods for measuring the tau lifetime follows. An arbitrary combination of logical and temporal order is adopted. Advantages and disadvantages other than those listed above are noted. In the final section arguments for why each analysis has not been applied at ARGUS are provided.

3.1 Decay Length Method (DL)

The *decay length* method uses the beam spot ($\vec{x}_B$) and reconstructed decay vertex ($\vec{x}_V$) in three-prong tau decays (decays where the tau decay products form three charged tracks) to estimate on an event-by-event basis the distance the tau travels (Figure 3.1). This is the only method that directly tries to determine the production and decay points of the tau. However, because the z positions of both the tau production and decay points are so poorly known, the decay length is measured in 2 dimensions and scaled to 3 dimensions using
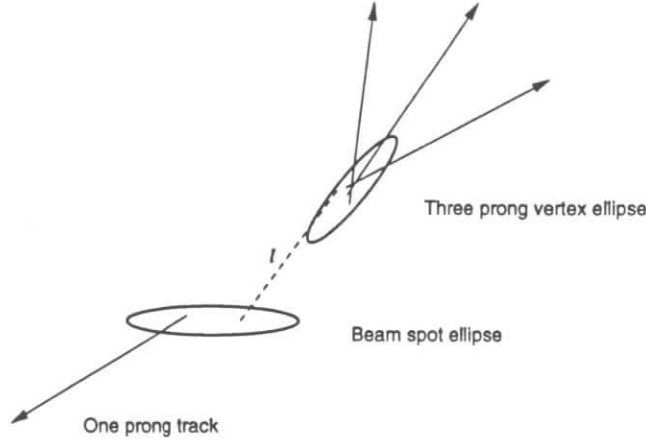
Figure 3.1: Schematic for the *decay length* method.

the thrust or sphericity axis as an estimate of the tau flight direction.

Although simply measuring $(\vec{x}_V - \vec{x}_B)_{xy}$ and extrapolating to three dimensions does provide an estimate of the lifetime, the standard technique is first to sharpen up the two-dimensional decay length measurements using the projected estimate of the tau-production axis. This fixes the tau direction in the $r - \phi$ plane on an event-by-event basis and a χ^2 minimisation or maximum likelihood procedure based on the beam ellipse and vertex ellipse errors is performed. This allows better estimates of the production and decay points and consequently a more precise decay length. In the DELPHI notation from [33] the following likelihood function is maximised with respect to $l = |(\vec{x}_V - \vec{x}_B)_{xy}|$:

$$
\begin{aligned}
L(l, \delta_x, \delta_y) &= \log P(x_v, y_v; x_o, y_o) - \frac{1}{2}(\delta_x/\sigma_x)^2 - \frac{1}{2}(\delta_y/\sigma_y)^2 \\
x_v &= x_b + \delta_x + l\cos\phi \\
y_v &= y_b + \delta_y + l\sin\phi
\end{aligned}
\tag{3.1}
$$

where (δ_x, δ_y) is the (fitted) offset of the tau production point from the beam position centre (x_b, y_b), σ_x and σ_y are the beam ellipse errors, and ϕ is the

estimated direction of the tau in the $r - \phi$ plane. The function $P(x_v, y_v; x_o, y_o)$ represents the probability of the true tau decay point being (x_v, y_v) given that the measured vertex position is (x_o, y_o), and uses the complete covariance matrix of the fitted vertex. The conversion to a three-dimensional decay length is then made using the $\sin\theta$ value of the tau flight direction, and the decay time calculated as

$$
t = \frac{l}{\beta\gamma c \sin\theta}.
\tag{3.2}
$$

Using t and σ_t (derived from the likelihood fit) for each event, a value for the lifetime can be extracted. Typically this is done in either of two ways. One approach is to use a maximum likelihood fit of the observed set of (t, σ_t) values in the data sample. Assuming that the true (unsmeared) decay length distribution is of exponential form, a likelihood function is constructed for each event based on the convolution of an exponential with mean t_o and the resolution function of the detector (typically a Gaussian of width σ_t, or the sum of two Gaussians with widths proportional to σ_t). In conjunction with the measured values of t and σ_t the event can then be assigned a relative probability for having resulted from a particle of lifetime t_o. The value of t_o that maximises the product of all event probabilities then yields a lifetime estimate. (Often the errors σ_t are also allowed to vary by an overall scale factor in the fit to take into account any underestimation of the resolution.) For the case where a single Gaussian parametrisation of the resolution is used the event likelihood function is given explicitly by

$$
\begin{aligned}
F(t, \sigma_t; t_o) &= \int_0^\infty \frac{1}{t_o}\exp(-\frac{t'}{t_o}) \times \frac{1}{\sqrt{2\pi}\sigma_t}\exp(-\frac{(t'-t)^2}{2\sigma_t^2}) \\
&= \frac{1}{2t_o}\exp(\frac{\sigma_t^2}{2t_o^2} - \frac{t}{t_o})\mathrm{erfc}[\frac{1}{\sqrt{2}}(\frac{\sigma_t}{t_o} - \frac{t}{\sigma_t})].
\end{aligned}
$$

The form of the likelihood function is slightly more complicated for applications of the DL method at lower energy experiments because of the presence of a non-negligible $q\bar{q}$ background in the data.

A second approach is simply to use the weighted mean of the set of t values, which can be shown to be an unbiased estimator of the lifetime t_o. This method was applied to an ARGUS data sample of $162pb^{-1}$ in 1987

and the tau lifetime found to be [34] $(295 \pm 14 \pm 11)$fs, the first error being statistical and the latter systematic.

It should be noted that this method, in addition to a few others discussed below, takes no advantage of the second tau produced in the event.

3.2 The Classical Impact Parameter Method (IP)

The IP method uses the distance of closest approach d of the daughter particles in tau decay to the best estimate of the tau production point, typically the beam spot. Fast one-prong tracks are used. The analytic form of the unsigned impact parameter is given by

$$d = \gamma \beta c t \sin \theta_\tau \sin \psi \qquad (3.3)$$

where ψ is the angle the daughter track makes with respect to the tau direction in the $r - \phi$ plane,

$$\psi = \phi - \phi_\tau. \qquad (3.4)$$

The sign of the impact parameter is fixed according to whether the track passes upstream $(+)$ or downstream $(-)$ of the tau production point, these directions defined along the estimator for the tau flight direction of the event (Figure 3.2). The distribution of impact parameters has a mean that scales linearly with the lifetime of the tau; Monte Carlo is used to determine the exact relation. Alternatively, one can use Monte Carlo to determine the so-called *physics function*, the underlying generator level distribution of impact parameters, as a function of lifetime. This has to be smeared with a convolution of the beam position uncertainty, the beam error ellipse, and the detector resolution function before it can be fit to the observed spectrum. This second approach is more statistically powerful than the simple mean (because it introduces a further constraint, i.e. the expected shape of the distribution) but is more sensitive to systematic uncertainties.

The IP method requires an accurate knowledge of the beam spot position, and if the physics function approach is taken the beam envelope and track
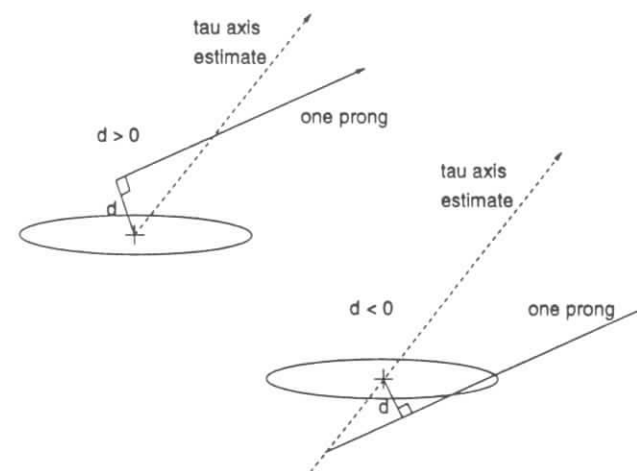
Figure 3.2: Definition of sign of impact parameter. Negative impact parameter values occur due to imperfect impact parameter resolution and/or imperfect knowledge of the tau direction.

spatial resolution function need also to be well understood. (For example, if the resolution is underestimated, i.e. the spatial precision of the track reconstruction unknowingly computed to be too good, then it cannot completely account for the observed broadening of the impact parameter distribution. The fit algorithm will attempt to compensate by widening the underlying physics function, thus leading to an overestimated lifetime value.) Because both the tau production point and the tau direction have to be estimated a considerable amount of smearing is introduced, making this method statistically weak. An advantage it has over the DL method is that it does not require a vertex and can be applied to one-prong decays, thus benefiting from a larger branching ratio.

3.3   The Miss Distance Method (MD)

The MD method [35] was developed in order to reduce the dependence on a knowledge of the beam location. For events where each tau decays in one-prong mode, the spectrum of distances of closest approach of the two daughter tracks in three dimensions is sensitive to the mothers' decay times. For a "zero lifetime" tau the two tracks have a common origin and necessarily meet except for the effect of imperfect detector resolution. Any deviation from this pure resolution distribution is due to the lifetime of the tau. *There is no need whatsoever to know the production point of the tau pair, and the beam spot position and shape do not need to be known.* The earliest proposals for measuring the tau lifetime with the three-dimensional capability of the μVDC (see Chapter 5) were based on this concept.

In two dimensions, of course, the two daughter tracks *always* meet at some point (except for tracks perfectly back-to-back in ϕ) and the distance of closest approach is a meaningless quantity (being always zero). For a two-dimensional analysis, therefore, one uses the beam spot position to define the location for measuring a quantity closely related to the distance of closest approach, the *impact parameter sum* ($\delta = d_+ + d_-$). This is the sum of the *signed* impact parameters of the two tracks (Fig. 3.3) at the beam spot. At LEP energies the daughter track directions lie closely along the
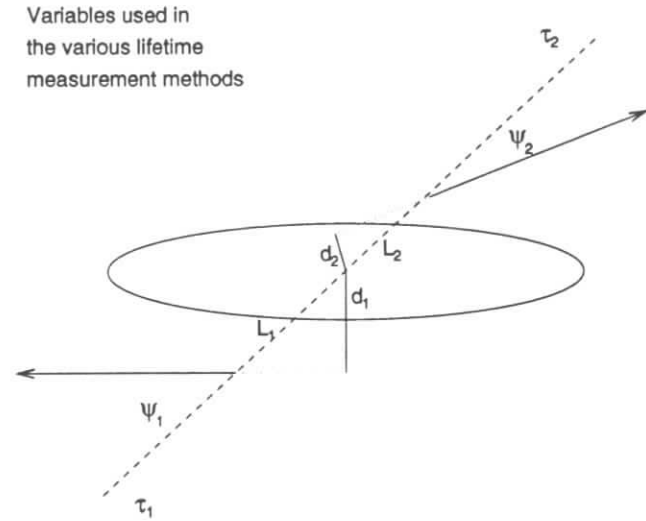
Figure 3.3: Diagram of variables used in *miss distance*, *impact parameter sum*, *momentum dependent impact parameter sum*, and *impact parameter difference* methods.

tau production axis and are essentially back to back. Therefore δ basically measures the distance of closest approach of the two tracks at the beam line, and is only influenced to a minor degree by the beam width and position. The smearing of the individual impact parameters due to the finite size of the beam envelope enters with opposite sign, and cancels in the sum. The dependence on the beam spot is not completely eradicated because one still needs to choose a reference point for calculating δ. This reference point is not arbitrary: different choices lead to different δ spectra. The least sensitivity to the beam spot width is achieved by choosing $\vec{X}_{ref} = \vec{X}_{bs}$, however, and so it is still necessary to know the beam spot parameters.

The MD method measures the *width* of the δ distribution, which is symmetric about the origin. As noted above, for a zero lifetime tau this distribution would simply reflect the resolution of the detector. Indeed, measuring this quantity for Bhabhas, di-muons, and two-prong two-photon events is a standard way of extracting a detector's resolution function from the data (see Chapters 7 and 8). Because the tau has a measurable lifetime this distribution is necessarily broadened, and the resulting δ spectrum is a convolution of the resolution function and the underlying δ distribution produced by the finite path lengths of the taus. Using 3.3 the analytic form for δ is given by

$$\delta = d_+ + d_- = \gamma\beta c \sin\theta_\tau (t_+ \sin\psi_+ + t_- \sin\psi_-) \tag{3.5}$$

Because θ_τ and $\psi_\pm$ are unknown, Monte Carlo is used to determine the δ distribution. This is parametrised as a function of τ_τ, convoluted with the resolution function, and then used to fit the δ distribution using the maximum likelihood method.

The main advantage of this method is its relative insensitivity to the tau production point and to the smearing introduced by the beam spot size. The disadvantage remains that the direction of the tau pairs is unknown and must be averaged out.

3.4 The Impact Parameter Sum Method (IPS)

The IPS method [36] is the result of an attempt to improve upon the MD method by taking into account the dependence of δ on the decay angles $\psi = \phi - \phi_\tau$ of the daughter one-prongs. This dependence is explicit in Equation 3.5, which relates the true impact parameter sum δ' to the decay angles ψ'. Although the measured track ϕ values are essentially equal to the true values, the correlation is nevertheless compromised because of the unknown tau direction, ϕ_τ, which must be approximated using the sphericity or thrust axis of the event. For each event the set of variables (δ, ψ_+, ψ_-) is measured and a maximum likelihood analysis carried out over all events based on the following likelihood function:

$$\frac{dN(\delta|\psi_+, \psi_-)}{d\delta} = \int d\delta' g(\delta - \delta') \int d\psi'_+ d\psi'_- h(\psi_+, \psi_-, \psi'_+, \psi'_-) \frac{dN'(\delta'|\psi'_+, \psi'_-)}{d\delta'} \tag{3.6}$$

Here $\frac{dN'}{d\delta'}$ is the probability function for a true value of δ' to occur given the true values of ψ'_+ and ψ'_-. This is easily expressed in closed form using the sum of two decaying exponentials. The function h accounts for the smearing of the true ψ' variables introduced by modelling ϕ_τ with the sphericity axis, and must be computed numerically using Monte Carlo. The function g accounts for the resolution of the detector.

At LEP, where this method has been applied, the sphericity axis lies within 20mrad of the true tau direction but the true decay angles ψ' are only of the order of 25mrad. Therefore, the correlation of δ with the decay angles is considerably weakened, to the point where this method gains only slightly in statistical power over the MD method.

3.5 The Momentum Dependent Impact Parameter Sum Method (MIPS)

The MIPS method [37] also relies on the δ distribution but takes into account the strong correlation between the momentum of each one-prong and its decay angle $\psi = \phi - \phi_\tau$ with respect to the tau flight direction. In three

dimensions, there is a one-to-one correspondence between the momentum of the charged track and its decay angle in the two-body decays $\tau \to \pi\nu$ and $\tau \to K\nu$. The presence of a second neutrino (in leptonic decays) or neutral particles (in hadronic decays) lessens the overall correlation but it remains strong enough to improve the lifetime estimate.

To extract a lifetime estimate using this method a maximum likelihood approach is employed on 1-1 topology events. The probability density function for observing a true impact parameter sum value $\hat{\delta}$ is constructed using Monte Carlo data and parametrised as a function of p_+ and p_-. This is then convoluted with the track resolution function to yield the likelihood function for observing a measured δ. On an event by event basis the measured track momenta p_+ and p_- define the probability density function. A maximum likelihood fit is performed on the entire event sample to determine the lifetime.

The advantage of this method is that an estimate of the tau production axis (in the x-y plane) is not required to construct the event likelihood function. Only the well defined track momenta are used. By using these momenta the correlation between δ and the track decay angles can be employed to advantage without suffering from the smearing brought on by the unknown tau axis, making this approach more powerful than the IPS method.

3.6 The Impact Parameter Difference Method (IPD)

Like the MIPS method, the IPD [38, 36] method does not require an estimate of the tau direction. The 1-1 topology is also used, but rather than employing the sum of the impact parameters, the *difference* Y is taken. With the help of Equation 3.3 this difference is written (assuming collinear taus)

$$
\begin{aligned}
Y &= \gamma\beta c \sin\theta_\tau(t_+ \sin\psi_+ - t_- \sin\psi_-) \\
&= \sin\theta_\tau(L_+ \sin\psi_+ - L_- \sin\psi_-)
\end{aligned}
\tag{3.7}
$$

Averaging over the decay lengths and using the small angle approximation this becomes

$$
\begin{aligned}
<Y> &= <L> \sin\theta_\tau(\sin\psi_+ - \sin\psi_-) \\
&= <L> \sin\theta_\tau \Delta\phi \\
&= \left[\frac{P_\tau}{M_\tau}\tau_\tau\right] \sin\theta_\tau \Delta\phi \\
&= \left[\frac{P_\tau}{M_\tau}\tau_\tau\right] X
\end{aligned}
\tag{3.8}
$$

where $\Delta\phi$ is the acoplanarity of the decay product tracks, $\Delta\phi = \psi_+ - \psi_-$. The acoplanarity can be computed without any reference to the tau decay axis direction, and the only dependence on this direction comes through θ_τ, derived from the event thrust axis. However, the event selection is typically limited to tracks from the barrel region of the detector where $\sin\theta$ is slowly varying, so that the polar angle dependence does not compromise the power of the method.

For non-radiative tau decays at fixed centre-of-mass energy Equation 3.8 shows that the mean impact parameter difference $<Y>$ scales linearly with X with a constant of proportionality directly related to the lifetime. The IPD approach is to make a linear fit of the $<Y>$ versus X distribution observed in data, taking into account any variation in centre-of-mass energy in the data sample, and extract the lifetime from the slope value. Corrections for radiative decays and the bias introduced by the small angle approximation are derived from Monte Carlo and used to adjust the lifetime value.

An advantage of this method is that it does not require any knowledge of the tau flight direction in the x-y plane and so avoids the loss in precision due to this unknown. However, in contrast to the previous methods which use the sum of the impact parameters δ for a lifetime estimate and therefore suffer only mildly from the smearing introduced by the beam spot size, the IPD method suffers doubly from this uncertainty in the tau production point.

3.7   The Three-Dimensional Impact Parameter Sum Method (3DIPS)

The 3DIPS method is the three-dimensional generalisation of the IPS method and requires precision tracking in the z direction as well as in the $x-y$ plane. As this condition is certainly not met at ARGUS the method will only be given a brief treatment here.

The 3DIPS method [39] capitalises on a well known feature of tau events wherein both taus decay into hadrons: it is in principle possible to determine the tau production axis to within a two-fold ambiguity from observing the energy and momentum of the final state hadronic systems, a direct consequence of energy momentum conservation. In practice imperfect detector resolution, incomplete detector hermeticity, and radiative decays degrade this determination but it is still possible to make fairly precise estimates of the two possible directions. A vector $\hat{H}$ perpendicular to the plane containing these two possible directions is guaranteed to be perpendicular to the true tau direction (barring radiative decays and resolution effects etc.) and provides an ideal axis upon which to project the three-dimensional impact parameter vectors of the decay product tracks (the vectors from beam spot to distance of closest approach of the track to the beam spot). It can be shown that the projection of the vectorial difference δ_3 of these three-dimensional impact parameter vectors is directly related to the three-dimensional decay lengths of the taus and to the well measured track angles with respect to $\hat{H}$. The δ_3 distribution is parametrised analytically and smeared with the detector resolution function. A maximum likelihood method similar to that used for the other methods is then employed to extract the lifetime.

The precision of this method is improved compared to the IPS method because 1) a larger distance δ_3 is measured compared to the measurement error and 2) the uncertainty due to the unknown tau direction is kept in check. Although this method can be applied to both 1-1 and 1-3 topology decays (for 1-3 topologies the best measured track is chosen in the calculation of δ_3) only hadronic channels (in both taus) can be used.

3.8   Summary of Recent Lifetime Measurements

Figure 3.4 provides a list of recent measurements of the tau lifetime by various collaborations, indicating the methods used in each case. It is clear that LEP
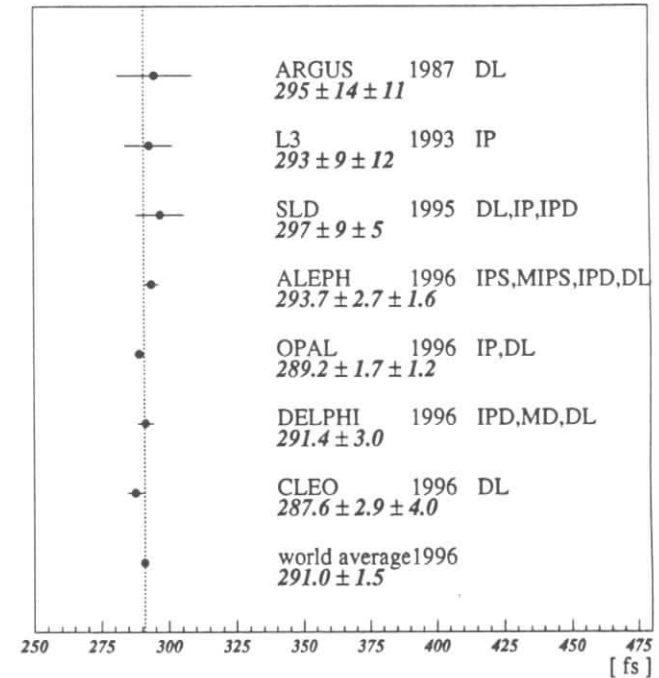
Figure 3.4: Recent tau lifetime measurements from various experiments.

has dominated this field in recent years. In fact, with the exception of the DL and IP methods, all the techniques described in this chapter were developed at LEP. This can be ascribed to the exploitation of silicon detectors and the very high purity and selection efficiency of the tau data sample at LEP. The high precision of the CLEO measurement is the result of an extremely large

event sample. The dashed line gives the world average value from [1], which is the average of all values shown except the ARGUS and CLEO ones.

3.9   Applicability at ARGUS

Because of the large size of the ARGUS beam spot compared to that of the other experiments (Figure 3.5), methods which rely directly on the beam

Ring	Size (microns)	Relative Size (Arbitrary Scale)
SLC	2.6 x .8	
LEP	160 x <10	
CESR	350 x 10	
DORIS	480 x 85	
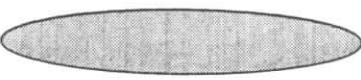
Figure 3.5: Beam spot sizes at various e^+e^- storage rings

spot position for an estimate of the tau decay point are not viable at ARGUS from a precision point of view. A second application of the DL method to ARGUS data, even though the size of the data sample has doubled, would not result in a measurement competitive with recent lifetime results, and it was deemed not worth repeating. The same holds true for the IP method. The 3DIPS method requires three-dimensional tracking and is not applicable to the available ARGUS data sample.

The remaining methods all employ the two-prong topology of tau pair production. At ARGUS this topology is plagued by backgrounds from Bhabhas, di-muons, and two-photon events, and a large, pure sample is very difficult to isolate. The six-prong topology, wherein each tau decays into three charged tracks, and a direct measurement of the tau flight distance can be made using the distance between the two reconstructed vertices, is doubly plagued in that 1) the rate is very low ($\approx 2\%$ of all tau pair production) and 2) events

are difficult to isolate from $q\bar{q}(\gamma)$ multihadron events. This leaves the one-three topology as the only one that can be reasonably studied at ARGUS. One could in principle select such events and then use the one-prong plus the fastest track on the three-prong side as a fake two-prong pair but this would lead to other problems. The large angles (ψ) involved cause the impact parameter to "feel" much more of the beam spot than at other experiments, and hence be more affected by it. Also, in the case of the IPD method the angles are much too large to make the approximation $\sin\psi \approx \psi$.

From these considerations, it was apparent to the author that a new technique for the ARGUS environment was worth developing. Such a method, the *vertex impact parameter* method, is described in the next chapter.

Chapter 4

The Vertex Impact Parameter Method

4.1 Introduction

All measurements of the tau lifetime have been made using, in some way, the nominal position of the electron-positron beam interaction point. As noted at the end of the previous chapter, the uncertainty introduced by the size of the DORIS beam spot is quite large and it would be beneficial to employ a method at ARGUS which does not use the beam spot. Such a method would in addition have the advantage of being insensitive to possible unknown systematic uncertainties associated with the beam spot determination. Most experiments model the beam position and width in a Gaussian manner, implicitly assuming the absence of any non-Gaussian effects, an assumption which cannot be checked.

A knowledge of the tau production point is not required, however, if one uses the tracking information from an entire four-prong tau event. With the 1-3 event topology the standard technique is to use the beam position and the reconstructed three-prong vertex as estimators for the production and decay points, respectively, of the three-prong tau. The one-prong side of the event is used solely for event selection purposes and otherwise does not contribute to the lifetime measurement. However, an indirect handle on the tau decay length distribution is available in the one-prong distance of closest approach to the three-prong vertex. For the ideal case of perfect spatial track

resolution and negligible background from non-tau events, the mean of this distribution scales in proportion to the lifetime value, the proportionality factor being immediately obtainable through Monte Carlo studies. This is an incomplete and oversimplified description of the technique adopted for this work and it suffices only to outline the basic strategy involved. The key point to be understood is that the tau production point becomes irrelevant with this approach, which will be referred to as the *vertex impact parameter method* or VIP method.

4.2 Detailed Description

Figure 4.1 depicts the decay process of a non-radiative four-prong tau pair event at the physics level. Neutrals are not shown. The taus are produced
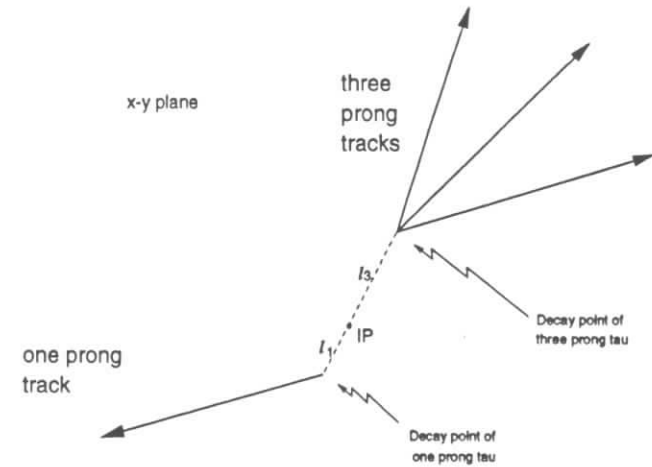
Figure 4.1: Physics level view of a four-prong tau pair event.

back-to-back at the interaction point IP, and decay at independent times t_1 and t_3 later, travelling distances ℓ_1 and ℓ_3 given by

$$\ell_i = c\beta_\tau\gamma_\tau t_i = c\frac{P_\tau}{M_\tau}t_i, \tag{4.1}$$

where c is the speed of light in vacuum, and P_τ and M_τ are the momentum and mass of the tau, respectively. γ_τ is the time dilation factor resulting from the velocity $c\beta_\tau$ of the taus.

If all the information displayed in Figure 4.1 were known on an event-by-event basis it would be relatively straight-forward to measure the lifetime. In reality, however, the IP is unknown, as is the direction along which the taus are produced (termed the tau production axis in what follows), and the points in space where the tau leptons actually decay. Fortunately, this information can be partially recovered by estimating the three-prong decay point using its reconstructed vertex, and by associating the direction of the total three-prong momentum with the tau production axis. Then two quantities which reflect the finite lifetime can be measured in each event:

- the vertex impact parameter (dca), which is defined as the signed distance of closest approach of the one-prong to the three-prong vertex, where the sign is chosen in the same way as the sign of the impact parameter defined in Section 3.2, and

- the decay point separation distance ($xsep$), which is the signed distance from the three-prong vertex to the intersection point of the three-prong momentum with the one-prong track, with sign taken from dca.

A visual definition of these variables is shown in Figure 4.2. One notices that $xsep$ is roughly equivalent to the distance between the decay points of the two taus and hence provides a fairly direct measurement of the lifetime. dca is a more convoluted measure of the lifetime but no less powerful than $xsep$. The two variables are related through the acoplanarity angle ψ

$$dca = xsep \cdot \sin\psi. \tag{4.2}$$

Both dca and $xsep$ scale directly with the tau lifetime value, and the proportionality factor can be derived from Monte Carlo. Figure 4.3 shows the sign of dca for various configurations.

The distributions of these lifetime variables at the generated and reconstructed levels for a sample of tau Monte Carlo data generated with lifetime
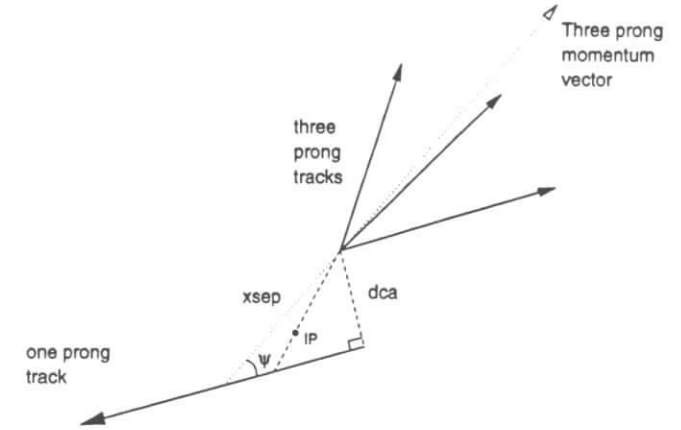
Figure 4.2: Definition of the variables dca and $xsep$ in 1 vs 3 tau decay.

303fs and passing all the cuts described in Chapter 8 are shown in Figures 4.4 and 4.5. The generator level variables are first calculated using the true three-prong tau decay point. Negative tails appear when the three-prong momentum vector is used instead as an estimate of the production axis, and the distributions are significantly broadened when the finite detector resolution comes into play. The cause of this broadening is divided roughly equally between the one-prong impact parameter resolution and the three-prong vertex position resolution. Mean values for these uncertainties (displayed in Figure 4.6) are $\sigma_T = 90$ microns and $\sigma_L = 480$ microns for the transverse and longitudinal (with respect to the major axis) vertex errors, respectively. The error on the one-prong track impact parameter, d_o, has a mean of $\sigma_{d_o} = 140$ microns. The major axis of the error ellipse has an r.m.s. deviation of about 50mrad from the three-prong momentum direction.

One approach to extracting the tau lifetime with these distributions would be to use the simple mean of the event sample, e.g.,

$$< dca > = \sum_{i=1}^{N} dca_i$$
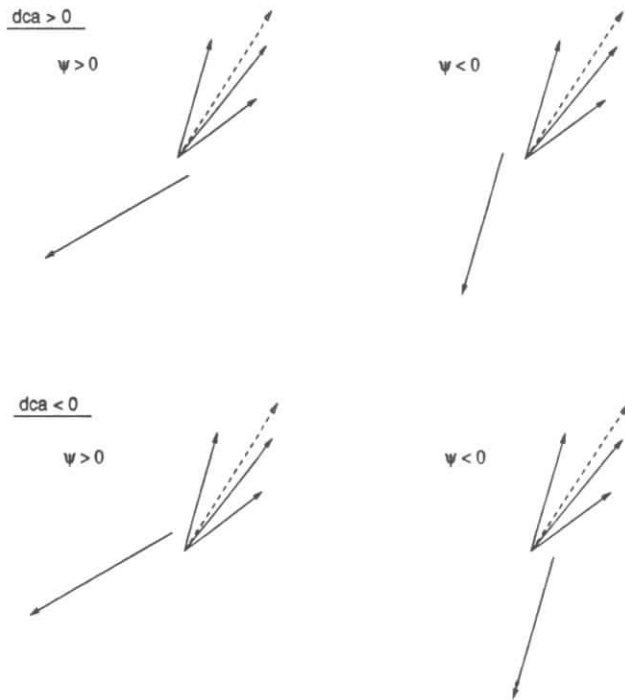
Figure 4.3: Sign of *dca* for various configurations.
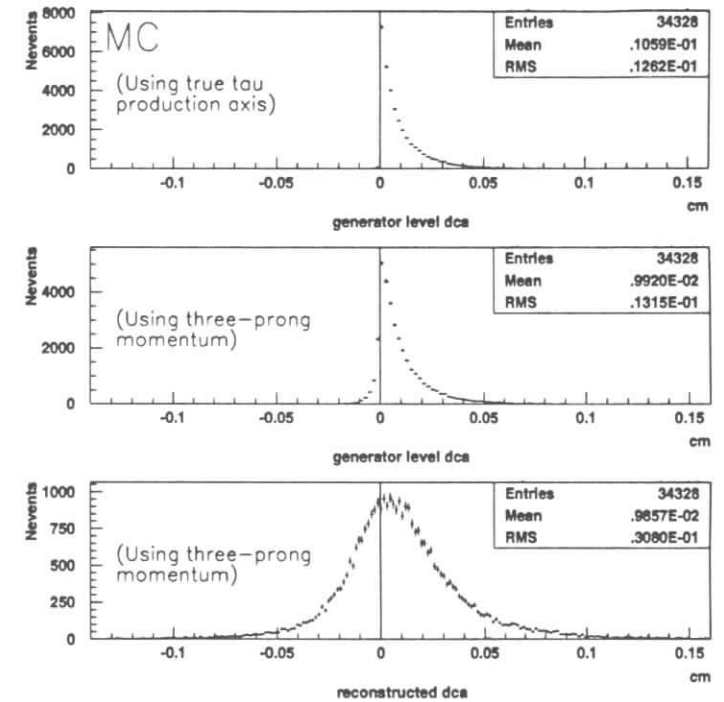
Figure 4.4: The tau Monte Carlo distributions for the vertex impact parameter lifetime variable *dca* a) at the generator level using the true tau flight direction for the tau production axis, b) also at the generator level but using the three-prong momentum vector for the tau production axis, and c) at the reconstruction level.
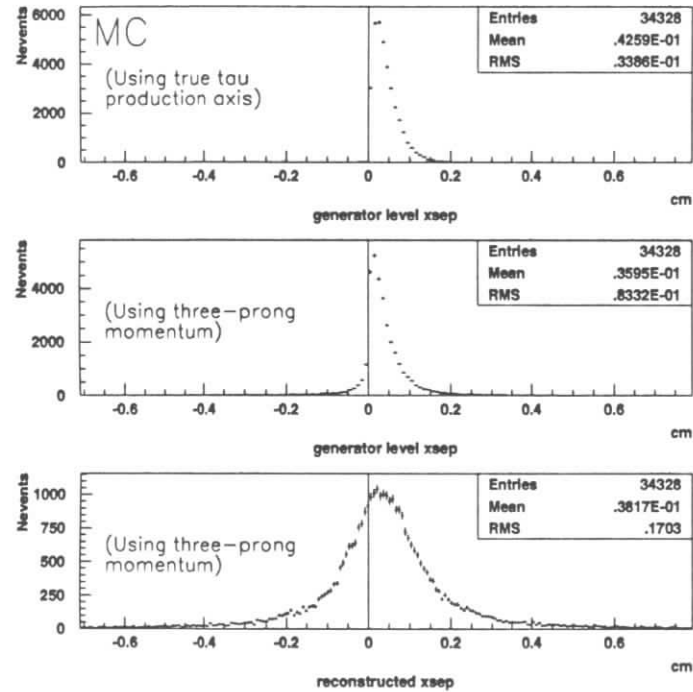
Figure 4.5: The tau Monte Carlo distributions for the decay point separation distance variable *xsep* a) at the generator level using the true tau flight direction for the tau production axis, b) also at the generator level but using the three-prong momentum vector for the tau production axis, and c) at the reconstruction level.
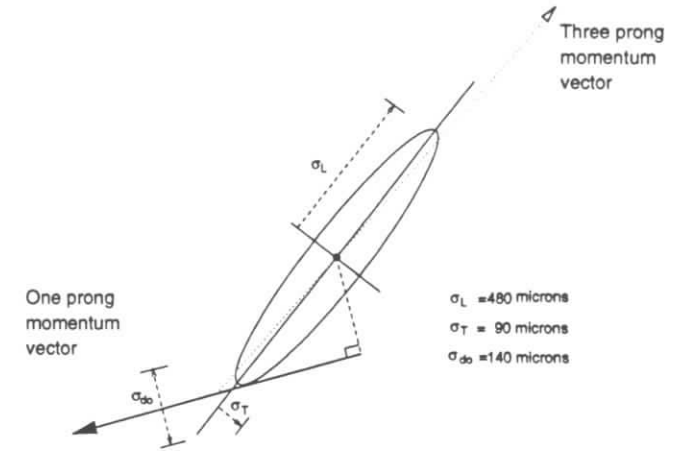
Figure 4.6: Schematic of errors associated with the tau lifetime measurement. Not drawn to scale.

in a comparison of Monte Carlo and experimental four-prong data, taking into account the lifetime contribution from background events. However, this approach ignores the fact that some events have more precise lifetime variables than others, a direct consequence of event topology and kinematics. To treat all *dca* or *xsep* measurements on equal footing would not take full advantage of the detector capability, a somewhat dissatisfying prospect.

A possible improvement on the simple mean, the *weighted mean*, e.g.

$$< dca >_W = \frac{\sum_{i=1}^{N} \frac{dca_i}{\sigma^2_{dca_i}}}{\sum_{i=1}^{N} \frac{1}{\sigma^2_{dca_i}}}$$

introduces a bias in the lifetime measurement and cannot be used. Figure 4.6 helps to demonstrate why this is so. The error on *dca* is the sum in quadrature of the error on the vertex position and the error on the one-prong impact parameter, d_o, and depends upon the angle the one-prong makes with the major axis of the vertex ellipse. Since the major axis is strongly correlated

with the three-prong momentum, the error can be written

$$\sigma_{dca}^2 \approx \sin^2(\psi)\sigma_L^2 + \cos^2(\psi)\sigma_T^2 + \sigma_{do}^2. \tag{4.3}$$

This expression shows that for larger values of ψ more of the longitudinal component σ_L^2 of the three-prong vertex contributes to σ_{dca}^2, and therefore larger values of ψ are associated with larger dca errors. However, larger values of ψ also yield larger dca values on average. (see Figure 4.9). Hence, there is a strong correlation between ψ and dca. Ignoring this correlation by taking a strict weighted average necessarily leads to a bias in the lifetime estimate towards lower values, because the dca values around zero have the highest weight. The weighted average is in fact found to underestimate the lifetime by about 30%. A weighted average of the $xsep$ variable is similarly biased.

To take into account the varying precision of the lifetime variables, remain bias free, and extract the most lifetime information, a two-dimensional fit method termed the *vertex impact parameter* (VIP) method was devised that properly handles the $dca - \psi$ correlation. The procedure is to construct a joint probability function $F(dca, \psi)$ for observing any set of dca and ψ values, and to use this function in a maximum likelihood fit to the sets of dca and ψ observed in the data. This correctly compensates for the correlation by dictating how the dca probability distribution (and therefore its mean) varies as a function of ψ. Because for a fixed value of ψ there is no correlation between dca and its error (see Eq 4.3), no bias is introduced by using a weighting technique. This approach is somewhat like performing a separate weighted mean of the data for each distinct value of ψ. A two-dimensional maximum likelihood method does the job somewhat more elegantly, however. Furthermore, it is more statistically powerful because not only the mean (first moment) but also the shape (all moments) of the underlying physics distribution is taken into account, adding further constraints. A disadvantage is that the shape must be provided as input, making the method somewhat Monte Carlo dependent.

In a maximum likelihood fit the weight of the event is taken into account by convoluting the true dca spectrum with the uncertainty in dca on an

event-by-event basis. This is made more explicit in the next section where it is shown how to construct the likelihood function.

The reader may have concluded that the $xsep$ variable has been neglected here. In fact, through the relation 4.2, this handle on the lifetime is very much present in the two-dimensional probability distribution. Therefore, the VIP method successfully employs the lifetime information from both dca and $xsep$, correctly accounting for correlations.

4.3 The τ Likelihood Function

To determine the likelihood function $F(dca, \psi, \sigma)$ a large Monte Carlo data sample of 575 000 tau pair events (including initial and final state radiation) was generated with the TAUOLA/KORALB packages (see Chapter 8), and run though a full simulation of the ARGUS detector. A centre-of-mass energy equal to the mean energy $E_{cms} = 10.55\text{GeV}$ of the experimental data was used, and the input lifetime was 303fs. The Monte Carlo data were then reconstructed and processed through the same event selection chain applied to the experimental data (see Chapter 8). About 34 000 events survive all the cuts. An appropriate set of generator level distributions from this sample was then modelled and used to build the required likelihood function as it would be without the effect of detector smearing. The resulting physics function was then convoluted with the detector resolution function in an appropriate manner to yield $F(dca, \psi, \sigma)$. This is made more clear in what follows.

The required generator level distributions are shown in Figure 4.7 together with their fit functions. They are (all variables in $x - y$ plane):

- $f(\ell)$, where ℓ is the unsigned separation distance between the generator level tau decay vertices,

- $g(\phi_3)$, with ϕ_3 the signed deviation of the three-prong momentum vector from the true mother tau direction, and

- $h(\phi_1)$, where ϕ_1 is the signed deviation of the one-prong from its true mother tau direction.

$$I_o \quad = 0.0214$$
$$\sigma^3 \quad = 0.12$$
$$f'_o \quad = 48.3\%$$
$$f'_b \quad = 51.7\%$$
$$\sigma'_o \quad = 0.22$$
$$\sigma'_b \quad = 0.44$$
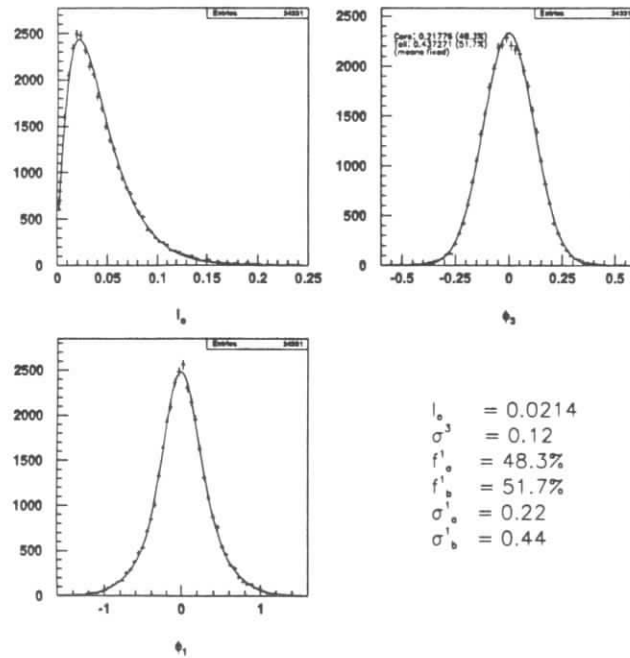
Figure 4.7: Generator level distributions of physics function variables together with fit results.

These distributions are parametrised with the following empirical forms: a sum of two Gaussians for ϕ_1, a Gaussian for ϕ_3, and for ℓ the form

$$f(\ell) = \frac{\ell}{\ell_o^2} \times e^{-\ell/\ell_o}. \tag{4.4}$$

This expression for $f(\ell)$ is exact only for the three dimensional decay point separation (neglecting initial and final state radiation), but describes the two dimensional separation reasonably well. The parameter ℓ_o scales linearly with the lifetime value τ_r, and is the only parameter that has any lifetime dependence. It therefore provides the means of measuring the tau lifetime.

Figure 4.8 defines these variables visually. Neglecting for the moment any
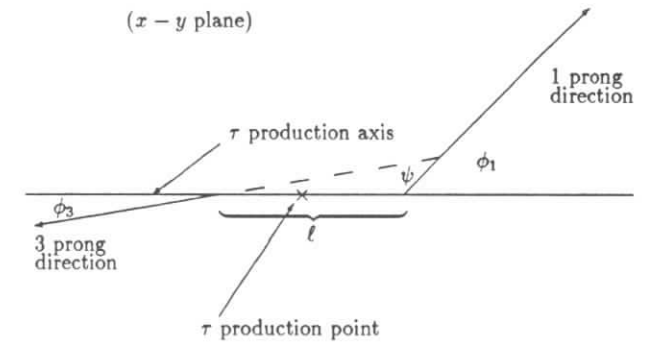
Figure 4.8: The variables ϕ_1, ϕ_3, ψ and ℓ described in the text. As shown both ϕ_1 and ϕ_3 have positive sign.

correlation in the decay angles due to selection cuts or spin-spin correlations, the three variables are independent of each other and completely define the event from a lifetime measurement point of view. Although none of these variables is observable, the two observables dca and and ψ are expressible in

terms of them:

$$\psi = |\phi_1 - \phi_3| \text{ and } dca = \ell \cdot \sin(\phi_1). \qquad (4.5)$$

To determine $F(dca, \psi)$ at the generator level (ignoring the finite detector resolution) one makes a change of variables from $\{\ell, \phi_3, \phi_1\}$ to $\{dca, \psi, \phi_1\}$ and integrates over the unobserved ϕ_1 variable (the Jacobian adds in a factor $|1/\sin(\phi_1)|$:

$$F(dca, \psi) = \int_{\phi_1} \frac{d\phi_1}{|\sin(\phi_1)|} h(\phi_1) \cdot g(\phi_1 - \psi) \cdot f\left(\frac{dca}{\sin(\phi_1)}\right).$$

This is a simplified form of the actual expression, which is complicated by the signs of dca and ϕ_1. In the real case $F(dca, \psi)$ is the sum of two integrals, one over $\phi_1 < 0$ and one over $\phi_1 > 0$. A more detailed description is provided in Appendix A.

To make the connection between this generator level probability distribution and the distribution of the variables actually observed in the detector, the function needs to be convoluted with the resolution function for these variables. The smearing in ψ is relatively small and can be neglected, and only the resolution function for dca needs to be included. For each event there is an error estimate σ associated with dca provided by the ARGUS track fit. This is used to build the resolution function $R(\epsilon, \sigma)$ which gives the probability that the true vertex impact parameter is in fact $dca + \epsilon$. More on this can be found in Chapter 8. Adding in the resolution function the final smeared physics function becomes:

$$F(dca, \psi, \sigma) = \int_\epsilon d\epsilon R(\epsilon, \sigma) \int_{\phi_1} \frac{d\phi_1}{\sin(\phi_1)} h(\phi_1) \cdot g(\phi_1 - \psi) \cdot f\left(\frac{dca - \epsilon}{\sin(\phi_1)}\right). \quad (4.6)$$

In general this expression has no closed form but with the choice of fit functions for the ℓ, ϕ_1, and ϕ_3 distributions listed above, it is possible to reverse the order of integration and carry out the resolution integral first, leaving a single integral to be performed by a numerical integration package. A detailed derivation of the likelihood function is given in Appendix A.

The curves of Figure 4.9 were produced using Equation 4.6, or more correctly, Equation A.18. A mean resolution of $\sigma_o = 250$ microns was input,
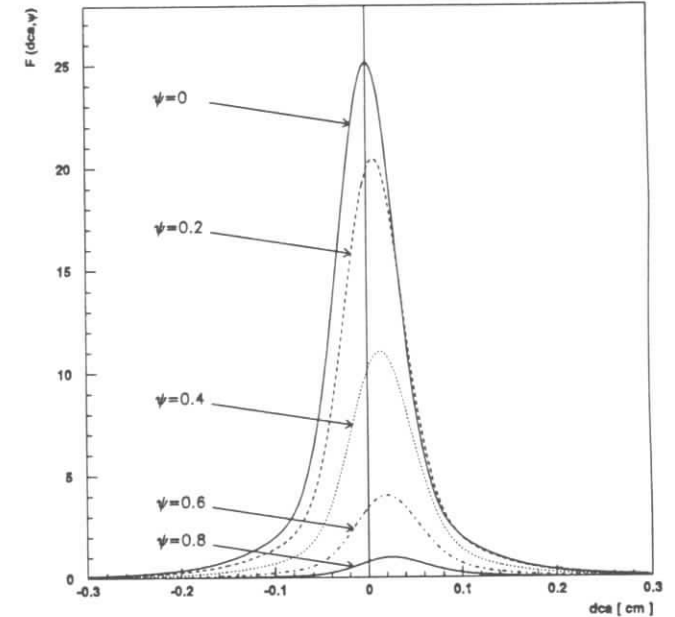
Figure 4.9: Cross section of the two-dimensional physics function for various values of ψ. The curves were generated for a lifetime of 303fs using a triple Gaussian resolution function having the parameters listed in the text.

modified by a triple Gaussian resolution function having widths and fractional areas of (see Equation A.11)

$$\begin{aligned} \sigma_1 &= 1.2 \cdot \sigma_o & c_1 &= 0.65 \\ \sigma_2 &= 3.0 \cdot \sigma_o & c_2 &= 0.25 \\ \sigma_3 &= 6.0 \cdot \sigma_o & c_3 &= 0.10 \end{aligned} \quad (4.7)$$

These numbers are based loosely on the experimental resolution function values. The input lifetime value was 303fs, corresponding to $\ell_o = 214\mu$ in the ARGUS detector after cuts (see Chapter 8). The width of each curve broadens or narrows depending upon whether the mean resolution is greater or less than σ_o, therefore it is important to calculate the resolution function correctly, otherwise the wrong shape would be used, biasing the result. It should be stressed that the relative normalisation of these curves is not arbitrary, but is dictated by the likelihood function F. The accuracy of these curves has been checked by comparing them to the corresponding distributions from a large simple Monte Carlo event sample generated with a small FORTRAN program. The agreement was found to be excellent for all values of dca and ψ, which implies that the integration and coding have been done correctly.

With Eq. 4.6 in hand it is a straight-forward matter to extract the lifetime from a sample of four-prong tau events. The *maximum likelihood method* was adopted to extract the lifetime using the function $F(dca, \psi, \sigma)$. The procedure is a conventional one. The probability density function $F(dca, \psi, \sigma)$ provides on an event-by-event basis the relative probability for observing the variables dca and ψ given the error σ on dca. Because the kinematics, and therefore $\{dca, \psi, \sigma\}$, of each event are independent of each other, the relative probability for observing the N different measurements $\{dca, \psi, \sigma\}$ of the event sample as a function of lifetime τ_τ is

$$\prod_i^N F(dca_i, \psi_i, \sigma_i; \tau_\tau).$$

The most likely value of τ_τ for the sample is the one that maximises this product, because then the observed distribution most closely resembles the expected distribution. This value is taken as a measurement of the tau lifetime.

The method was checked by applying it to a large reconstructed Monte Carlo data sample passing all cuts. The MINUIT [40] package was used to perform the function maximisation. For a lifetime of 303fs the VIP method yielded a lifetime of (296.7±3.9)fs compared to a less precise value of (306.3± 5.8)fs from the simple mean and a strongly biased weighted mean result of (204.8 ± 4.0)fs (statistical errors only). There appears to be a tendency for the VIP method to underestimate the tau lifetime by (2.1 ± 1.3)%, although at 1.6 standard deviations the shift is not significant and more Monte Carlo would be required to confirm that a bias exists. In any case, slight biases like this are not uncommon among the various lifetime methods and are usually accounted for by adjusting the final experimental measurement by the observed shift in Monte Carlo. Possible explanations for a shift include

- incorrect modelling of underlying physics functions,

- K_S^o contamination ,

- neglect of errors on angles,

- spin-spin correlations,

- and the effects of cuts.

Shown in Figure 4.10 is the dca spectrum for this Monte Carlo sample. The curve shows the predicted spectrum based on the final fitted lifetime. This is derived from a weighted sampling of the individual event likelihood functions and is *not* the result of a direct fit to the dca spectrum. The agreement is very good.

4.4   The $q\bar{q}$ Likelihood Function

The likelihood function described in the previous section holds for a pure sample of tau decays. In reality, the experimental data sample is not pure, but contains a fraction of the order of $f = 4\%$ multihadron $q\bar{q}$ background, about 30% of which has a non-zero lifetime component of its own. The appropriate likelihood function therefore requires additional terms to account
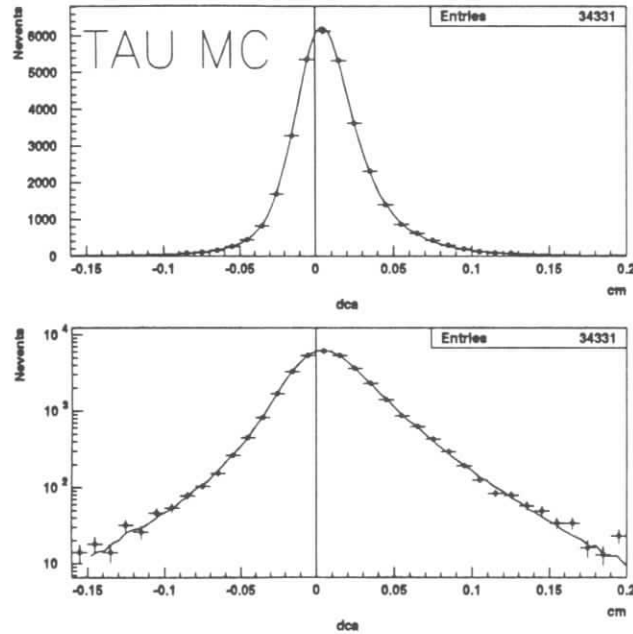
Figure 4.10: Monte Carlo *dca* spectrum with the result of the likelihood fit overlaid. Linear and log scale views are shown.

for these contributions. Two types of background contamination need to be modelled. Data that do not contain long lived particles (zero lifetime component) and data that do (non-zero lifetime component). Denoting the total $q\bar{q}$ fraction of the data by f, and the fraction of $q\bar{q}$ data with long lived particles by α, the complete likelihood function F is given by

$$F = (1 - f) \cdot F_\tau + f \cdot [(1 - \alpha) \cdot F_{q\bar{q}}^o + \alpha \cdot F_{q\bar{q}}^t]. \qquad (4.8)$$

The form of the two lifetime components $F_{q\bar{q}}^o$ and $F_{q\bar{q}}^t$ is considered in the next two subsections.

4.4.1 Zero Lifetime Component

This component is very easily accounted for. By definition, all the four-prong tracks originate from the same point, i.e. $d' = 0$. Therefore, the probability for observing the dca value $d = d' + \epsilon = \epsilon$ is simply given by the product of the resolution function, $R(\epsilon)$, and the probability for observing ψ, $\Psi(\psi)$, i.e.,

$$F_{q\bar{q}}^o(d, \psi) = R(d) \cdot \Psi(\psi). \qquad (4.9)$$

This can be confirmed explicitly by evaluating the tau likelihood function in the limit $\ell_o \to 0$. Referring to Appendix A, this yields

$$F_{q\bar{q}}^o(d, \psi) = R(d) \cdot 2 \cdot \int_{-\phi_1^{max}}^{\phi_1^{max}} d\phi_1 h(\phi_1) \cdot g(\phi_1 - \psi), \qquad (4.10)$$

which has the correct form for the ψ spectrum assuming ϕ_1 and ϕ_3 are uncorrelated. For the analysis, the ψ spectrum observed in Monte Carlo data is fit directly with a sum of two Gaussians because there is neither advantage nor necessity in developing it from the individual ϕ_1 and ϕ_3 spectra. In contrast, in the treatment of background events with lifetime, discussed next, the ϕ_1 and ϕ_3 spectra must be explicitly modelled.

4.4.2 Non-Zero Lifetime Component

This component is far trickier to account for, but fortunately it is reasonably small so it is not necessary to model it perfectly. Unlike the situation for tau

decays where a single particle type has a well defined back-to-back production dynamics and well defined decay points, the non-zero lifetime $q\bar{q}$ background involves a wide variety of long-lived particle types. Often more than one long-lived particle type contributes to an event, so that the three-prong tracks need not all originate from the same point. CPU constraints prevent a complete Monte Carlo investigation of all the various possibilities involved, and in any case it is not entirely clear how one would make a legitimate connection to the treatment of the tau likelihood function. Instead, the approach adopted is to use the averaged distributions of each of the variables ϕ_1, ϕ_3, and ℓ and proceed as in the tau likelihood function case.

The Monte Carlo $q\bar{q}$ background angular distributions are shown in Figure 4.11. Some elaboration of the approach used to derive them is required. First, in each event used in the Monte Carlo sample an axis must be chosen at the generator level in order to define the angles ϕ_1 and ϕ_3. This axis is not arbitrary - it should correspond to the direction in the $x - y$ plane of the particle(s) having observable lifetime, as in the tau case. As pointed out above, the underlying physics is too complex to admit a perfect model and instead the axis along which the original $q\bar{q}$ pair is produced is used. For radiative decays or decays in which more than one particle is produced in the initial parton state (corresponding to all the particles with no mother in the LUND [41] event record) this axis is taken as the thrust axis of the initial set of particles. The angles can then be calculated using the generator level tracks. A potential problem arises in that there may be no correspondence between the observed 1-3 structure at the detector simulation level and that at the generator level. Fortunately, there is a high probability for a proper match (> 95% is a conservative estimate) and the angular distributions can be modelled without penalty using only those events that *are* matched. Each is parametrised with the sum of two Gaussians similarly to the tau pair case. The distribution of ℓ is more difficult to calculate, but can be modelled in an unambiguous and straight-forward manner if one views the underlying physics as, on average, mimicking a single particle type X produced back-to-back with its antiparticle $\overline{X}$, in direct analogy to tau pair production. (This is not an unrealistic assumption. The non-zero lifetime
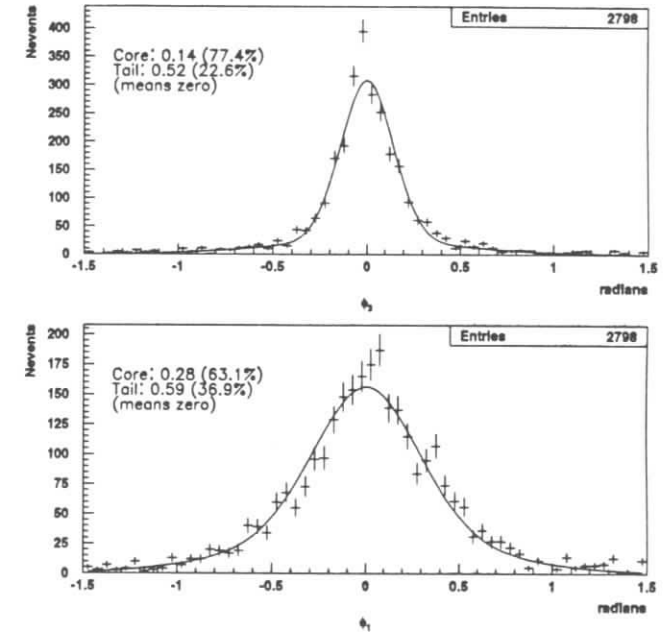
Figure 4.11: The $q\bar{q}$ background angular distributions ϕ_3 and ϕ_1 derived from Monte Carlo. The overlaid functions are the results of fits with a sum of Gaussians each of mean zero. The width and fractional area of each Gaussian is also indicated.

contribution is almost entirely due to charm anti-charm meson production via $c\bar{c}$ events, so that the typical scenario is the one assumed.) With this assumption, the same functional form used to model the tau pair ℓ distribution can be applied, i.e,

$$f(\ell) = \frac{\ell}{\ell_q^2} \times e^{-\ell/\ell_q}. \tag{4.11}$$

The value of ℓ_q, which represents the characteristic decay length of the fictitious particle in the x-y plane, can be determined by fitting the $dca - \psi$ spectrum for the non-zero lifetime component, leaving ℓ_q free, and using as input the parametrisations for ϕ_1 and ϕ_3 derived as described above. This approach of using the unambiguous detector simulation level quantities to derive the underlying function successfully avoids having to model the various generator level configurations. The fit yields $\ell_q = (490 \pm 20)$ microns (statistical error only). The final form for $F_{q\bar{q}}^t$ is obtained by smearing the underlying function with the detector resolution.

The procedure for determining $F_{q\bar{q}}^t$ is approximate and only valid if the non-zero lifetime $q\bar{q}$ contamination in the tau lifetime sample is small compared to the precision of the lifetime measurement, a condition that is well satisfied by the data.

4.5   Conclusion

The VIP method described in detail in this chapter was developed for the purpose of making a tau lifetime measurement at ARGUS without relying on the beam spot. The validity of the method is demonstrated through its successful application to Monte Carlo data. In principle, then, the method can be applied to experimental data to yield a high precision measurement of the tau lifetime.

Before proceeding to a detailed explanation of the application of the VIP method to ARGUS data, a general overview of the ARGUS detector is first provided in Chapter 5. This is followed in Chapter 6 by a detailed description of the algorithms used to reconstruct tracks and vertices with the ARGUS main drift chamber and vertex chamber, and finally by a closer treatment of

the calibration and alignment of these tracking detectors in Chapter 7.

Chapter 5

The Detector

5.1 Introduction

The ARGUS detector [42] is a universal, cylindrical, magnetic detector designed to study the Υ resonances produced in high energy e^+e^- annihilation collisions. Its most powerful attribute is its excellent ability to identify charged particles. As well, it provides good photon energy resolution and high precision momentum measurement over a nearly 4π solid angle. Located in the DORIS storage ring at the DESY laboratory in Hamburg, Germany, it accumulated a total of $514pb^{-1}$ between 1982 and 1992.

The detector comprises the following components (Figure 5.1):

Vertex Chamber. Installed in 1984, the vertex chamber has significantly added to the vertex locating power of the detector. Information from it can be combined with data from the main drift chamber to improve track reconstruction.

Main Drift Chamber. The main drift chamber is the heart of the detector. It isolates the curved paths of individual charged particles in the magnetic field, and measures their momenta. As well it supplies specific ionisation values necessary for particle identification.

Time-of-Flight Counters. The time-of-flight counters measure the flight times of particles originating at the interaction point. Combined with momentum and track information this provides an estimate of the rest

mass of the particle. In addition, the counters aid on-line luminosity monitoring.
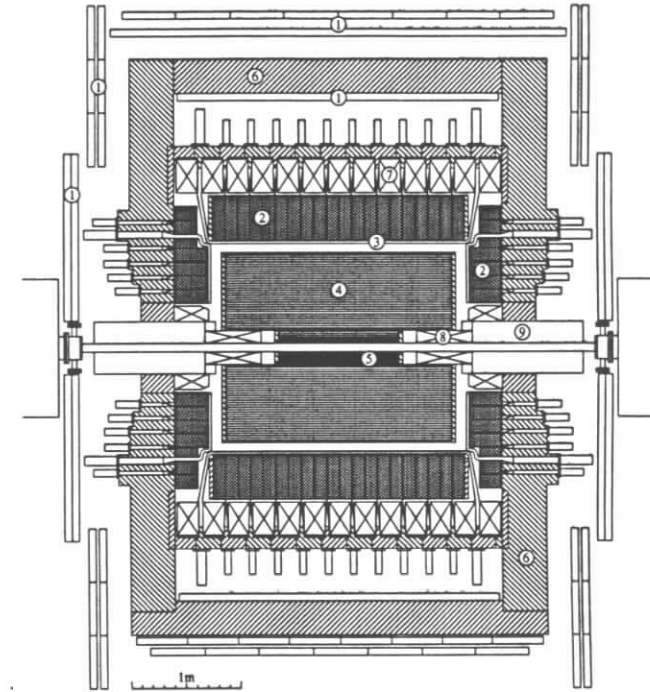
Figure 5.1: The ARGUS detector. 1. Muon chambers, 2. Shower counters, 3. Time of flight counters, 4. Drift chamber, 5. Vertex chamber, 6. Iron yoke, 7. Solenoid coils, 8. Compensation coils, 9. Mini beta quadrupole.

Electromagnetic Calorimeter. The electromagnetic calorimeter measures electron and photon energies. In addition, shower energies and shapes are used to distinguish between hadrons/muons and electrons.

Muon Chambers. The muon chambers lie outside the calorimeter and main coil. They detect the passage of penetrating charged particles.

Each of these components will be discussed in more detail in the following sections.

5.2 The Accelerator and Beam

ARGUS studies the Υ resonances through collisions of electron and positron beams supplied by the DORIS II storage ring (Figure 5.2). The beams
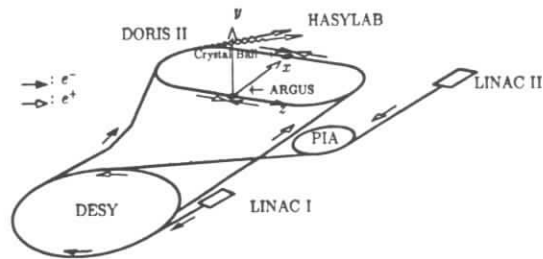
Figure 5.2: The DESY synchrotron and DORIS II storage ring.

are produced by separate small energy linear accelerators (LINAC). Because positrons are more difficult to produce than electrons, these have to be gradually accumulated in a small storage ring (PIA). Bunches of 2.7×10^{10} particles are then introduced into the main synchrotron DESY, accelerated to an energy compatible with that of the DORIS II storage ring, about 4.5GeV to 5.5GeV, and subsequently injected. The storage ring operates in single bunch mode at an RF frequency of 500MHz and is capable of storing currents of 30 to 50mA. Bunches collide once every microsecond, with r.m.s. beam dimensions of 480μm and 85μm in the x and y directions respectively. (A visual definition of the ARGUS coordinate system can be found in Figure 5.2.) An average luminosity of 3.3×10^{31}cm^{-2}s^{-1} is achieved [1].

5.3 Location of the Detector and Harnessing of the Beam

The ARGUS detector is located between two of the horizontal focusing quadrupoles of the DORIS II storage ring. DORIS II was constructed from the old double storage ring, DORIS I. As a consequence of this original design, the beam has to be diverted downwards with the use of vertical bending magnets, and interactions take place 20cm below the plane of the arcs. Thus, the detector components are spared the high intensity synchrotron radiation from the main horizontal bending magnets. The detector is further shielded from the low energy radiation from these vertical bends through the use of protective absorbers called "scrapers" and a thin layer of lead paint applied to the outside of the beam pipe.

Vertical strong focusing quadrupoles, termed "mini-β", are used to maximise the luminosity. To achieve the desired rate, it was found necessary to install the quadrupoles in a position where they protrude into the detector. Compensation coils surround them to prevent the ARGUS magnetic field from leaking in and degrading the luminosity.

5.4 The Magnetic Field

A 0.755T magnetic field strength is developed using thirteen 3m diameter coils that draw a total current of 4520A. This field value was chosen as a suitable compromise between good high momentum track resolution and good low momentum particle detection. A higher field creates larger track curvatures for fast particles allowing them to be more accurately reconstructed. However, too high a field causes low momentum particles to curl up too tightly to be detected in the vertex and drift chambers. The chosen field strength offers good wide range momentum resolution and allows detection of particles with transverse momenta as low as 30MeV/c. To ensure that the magnetic field does not deflect the beam, additional compensating coils have been placed just inside the mini-beta quadrupoles along part of the beam path.

In order to reconstruct accurately the momentum of any particle, it is imperative that the magnetic field strength be well known throughout the detector, especially in the main drift chamber where most of the information for momentum determination is obtained. Through the use of several Hall probes, the field was carefully mapped prior to the installation of the detector components in 1982 and found to be symmetric in the ϕ direction within the measurement uncertainty (0.1%). The field values were then corrected for an estimated misalignment of the probes and adjusted to satisfy Maxwell's equations. The field is presently modelled to within 0.2% with a polynomial parametrisation in each of the drift chamber layers. The uncertainty accounts for the balance of the systematic error on momentum measurement in the drift chamber.

5.5 Tracking and Vertexing Close to the Beam Line

5.5.1 The Axial Wire Vertex Chamber

Installed in 1985 around the beam pipe and between the compensation coils, the vertex chamber [43] is a high resolution drift chamber with a solid angle coverage of 95%. It is 1m long and has inner and outer radii of 5cm and 14cm respectively. Strung in the axial direction, 594 gold-plated tungsten-rhenium sense wires (20μm) and 1412 copper-beryllium field wires (127μm) combine to form the close-packed hexagonal cell structure displayed in Figure 5.3. In contrast to the main drift chamber, this configuration allows transverse coordinate measurement only. To reduce multiple scattering, the inner and outer cylindrical walls are constructed of a thin carbon fibre epoxy composite. The whole chamber is filled to a pressure of 1.5 bar with CO_2 doped with a 0.3% water vapour component to prevent wire degradation.

The spatial resolution as a function of drift distance is determined from the standard deviation of the distribution of residuals, a residual being the difference between the measured drift distance and the value obtained from the track fitting procedure. Resolution deterioration at small and large drift
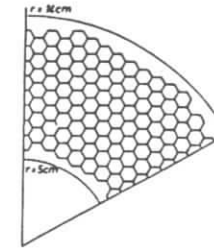
Figure 5.3: Schematic of a 60° section of the vertex chamber with the hexagonal cell structure explicitly shown. Sense wires are located at the centres of each hexagon, field wires at the corners.

distances can be accounted for by small ionisation statistics and non-circular isochrones respectively.

A very rough schematic of the field lines in the cell is provided in Figure 5.4. No attempt to include the influence of the magnetic field has been made, and the figure serves only to demonstrate the phi-dependence of both the strength and direction of the field. Particularly towards the boundary of each cell along the line joining two neighbouring sense wires, the isochrones are extremely poorly defined due to the weak field. This is discussed further in Chapter 7.

The chamber significantly increases the efficiency of locating K_S^0 and Λ^0 vertices decaying close to the interaction point. As well, any track information from it can be added to that of the drift chamber to improve momentum resolution.

5.5.2 The 3-D Micro-Vertex Detector

In 1989, the ARGUS vertex chamber was replaced with a superior micro-vertex drift chamber (μVDC) [44] employing a novel wire arrangement that enables three-dimensional track reconstruction (Figure 5.5). Stereo angles of $\pm45°$ are achieved by guiding wires around the chamber axis with the support of 5 radially-directed beryllium vanes of 0.89mm thick. The chamber contains 1070 wires strung so that in each 72° sector a planar arrangement of
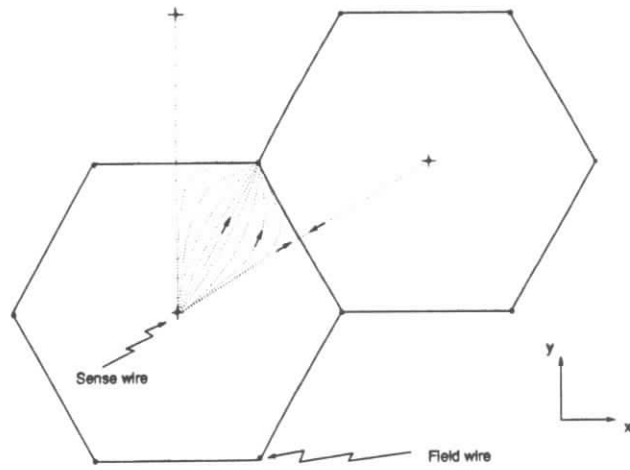
Figure 5.4: Schematic of field lines in a VDC cell. Deviations resulting from the effect of the magnetic field on the movement of charge in the cell are not included.
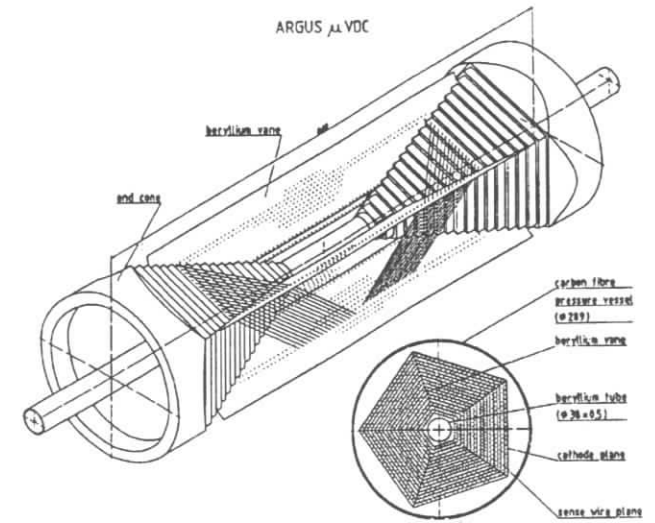
Figure 5.5: The ARGUS micro-vertex drift chamber installed in 1989.

sixteen drift cell layers is exhibited. Six pairs of stereo angle layers and four axial layers are used to do this, thus providing nearly equal track coordinate precision in the $r - \phi$ and $r - z$ projections. The wires are attached at each end to aluminium endcones having an accommodating pentagonal structure. Each axial wire begins and ends in the same sector, whereas each stereo wire traverses all five sectors along its path, passing through four of the five vanes. An axial layer of field wires is inserted between each of the sense wire layers, but no field wires are employed between the sense wires in a given layer. The cell size is rather small: 5.178mm from one sense wire layer to the next and 5.320mm between sense wires in each layer.

To improve the resolution at the vertex, the beam pipe was reduced from 40mm to 18.5mm inner radius, allowing track position measurements as close as 26mm from the beam line to be made. In addition, the beam pipe material was changed from aluminium to beryllium and halved in thickness.

The chamber was operated with a gas mixture of 80% CO_2 and 20% propane at a pressure of 3.1 bar. The elevated pressure helps compensate for the reduced ionisation statistics resulting from the the small cell size. The resulting spatial resolution is better than $40\mu m$ over most of the cell.

A total of $33pb^{-1}$ of data with the μVDC were collected in three separate running periods. Unfortunately, prior to installation an electric short in some drift wires occurred, and about ten percent of the chamber volume was ineffective for the first and most successful of these periods (about $17pb^{-1}$). Although the inefficient regions of the detector were revived for the ensuing running periods, the specific luminosity of the storage ring was very poor and an inadequate amount of μVDC data was added to the existing sample to allow any viable physics analysis. Moreover, in the second running period the beam pipe size was considerably reduced to allow the installation of a silicon detector around the beam pipe, which was then followed by an upgraded version in the final running period (see next section). The combination of smaller beam pipe and fluctuating beam and vacuum conditions in the storage ring led to serious background problems, necessitating a variety of changes to the trigger during data-taking. The fact that such a small amount of data was collected, and in such diverse running conditions, was

critical in the decision to abandon a lifetime measurement using μVDC data and focus on data collected with the VDC.

5.5.3 The Silicon Strip Detector

In 1991, a silicon vertex detector (SVX) was installed in ARGUS and upgraded the following year. The detector consists of seven single-sided silicon microstrip detectors of thickness 280μ and pitch 25μ, configured in an overlapping heptagonal form. To accommodate the SVX inside the inner μVDC wall, the beam pipe was reduced in radius from 2cm to 1.25cm.

In the middle of the 1992 running period, a magnet failed upstream of the ARGUS detector, resulting in the immediate loss of the beam. Injection was attempted several times before the cause of the failure was recognised. In the interim, the SVX suffered irreparable radiation damage and served solely as dead material for the rest of the run. Although a new silicon detector was built for the following year's running period, machine studies in April 1993 did not yield the improved luminosity deemed necessary for continuing, and ARGUS was shut down. A total of $7pb^{-1}$ of data with SVX readout were collected, not enough for any significant physics to be carried out.

5.6 The Main Drift Chamber

The drift chamber [45] serves as the central track finder for the ARGUS detector. Its excellent spatial resolution and highly efficient track finding capabilities combine to produce accurate event reconstruction. It also supplies good energy loss measurements for particle identification, and plays a central role in the operation of the slow trigger.

Located inside the calorimeter, the chamber extends 2m in the axial direction and has inner and outer diameters of 30cm and 172cm respectively. A total of 5940 sense wires and 24,588 field wires are strung between 30mm aluminium end plates to form a homogeneous small-cell pattern, essential for quick and efficient track reconstruction. This pattern consists of 36 concentric layers of drift cells, each cell having a cross section of $18 \times 18.8mm^2$ (See

Figure 5.6), nearly optimal for dE/dx resolution. The number of layers was
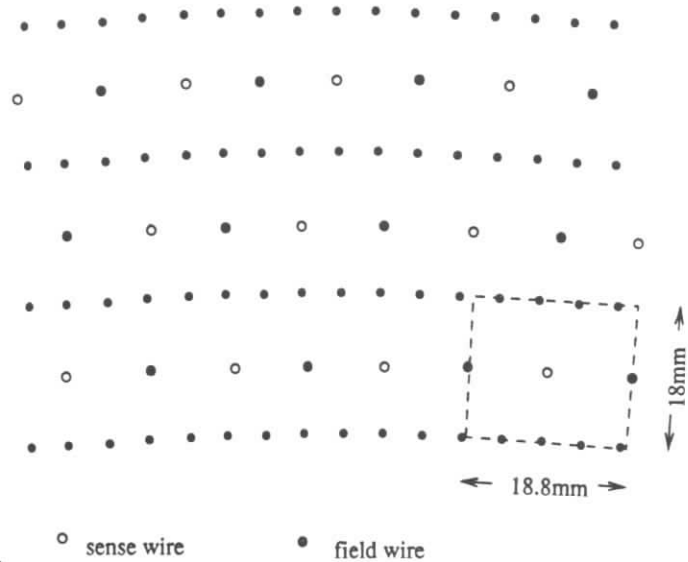
Figure 5.6: Cross section of the drift chamber perpendicular to the beam axis at z=0.

chosen as a suitable compromise between two competing factors: to improve track recognition and sharpen dE/dx resolution a large number of layers is preferable, while a smaller number helps to minimise multiple scattering and avoid excessive amounts of readout wires and electronics.

To determine the axial position of track hits, the sense wires possess successive stereo angles of $0°, +\alpha, 0°, -\alpha$, etc. with α increasing as $\sqrt{r}$ from 40 mrad to 80 mrad. These values were chosen in order to maintain almost circular drift time isochrones for most z values. The layer geometry is sketched in Figure 5.7.

The sense wires are made of gold-plated tungsten and have a diameter of 30μ. They are strung with a tension of 0.7N. In the absence of electrostatic effects this implies that the sag due to gravity reaches a maximum deviation
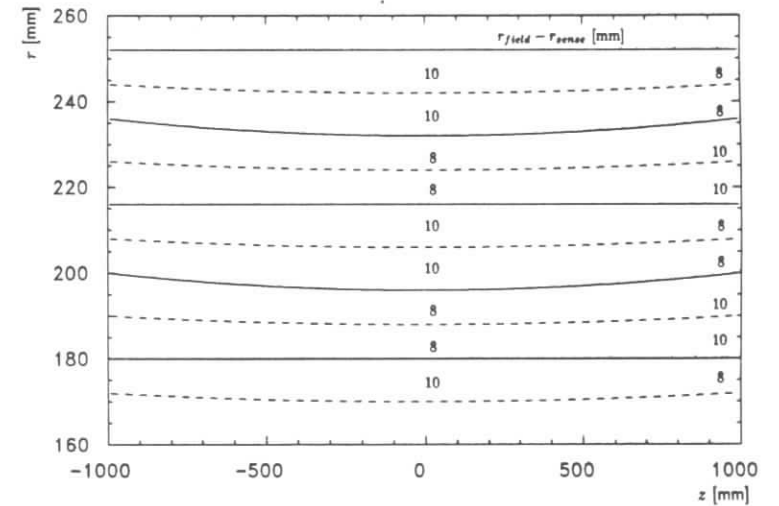
Figure 5.7: Schematic section through the innermost part of the ARGUS DC in the rz-projection. Solid lines are sense wire layers, dashed lines are field wire layers.

from a straight line of about 95 microns midway between the endplates. This has major consequences for the determination of the drift chamber wire positions as will be discussed in Chapter 7.

The chamber originally employed a mixture of 97% propane and 3% methylal as the amplifying gas. The large radiation length and slow diffusion rate of propane provide good momentum resolution, while its narrow Landau distribution optimises the dE/dx resolution for low momentum particles. An additional 0.2% of water vapour had to be added to this mixture to prevent the buildup of deposits on the field wires. Such deposits encourage charge buildup which eventually produces discharges resulting in large dark currents. This problem, known as the Malter effect, was cured by the water additive.

The sense wires are supplied with 2930V via $1M\Omega$ resistors with field wires kept at ground. This arrangement leads to a total gas amplification of 10^4 and creates ground wire surface fields of 25 kV/cm.

For track reconstruction purposes, it is important to be able to relate drift times to drift distances. This so called distance-time relation (DTR) is obtained from a sample of Bhabha scattering events using an iterative procedure. An approximate DTR is used to reconstruct the tracks of these events. The distances of closest approach are then compared to the TDC values and the functional relation smoothed to produce a better DTR approximation. Repeated application of this process produces the final parametrisation. A more detailed treatment of the drift chamber calibration can be found in Chapter 7. The mean spatial resolution of the chamber is about $130\mu m$, although for some periods the resolution is as good as $122\mu m$ or as poor as $170\mu m$. This variation is due to changes in threshold settings, different gas compositions, chamber ageing, varying reliability of the electronics, and a rather unfortunate problem which developed with the chamber endplates (see Chapter 7).

The momentum resolution of the drift chamber is directly dependent upon its spatial resolution, which can be determined by comparing measured drift distances with fitted track-wire distances from the reconstruction process. Results indicate that the resolution suffers from low ionisation statistics at

small distances and excessive deviations from circular isochrones at large distances. The momentum resolution at high momentum predominantly reflects uncertainties in track measurements and is given by

$$\sigma(p_T)/p_T = 0.009 p_T [\text{GeV}/c],$$

while for low momentum, multiple scattering dominates, leading to a resolution of

$$\sigma(p_T)/p_T = \sqrt{(0.01^2 + (0.009 p_T [\text{GeV}/c])^2)}.$$

The absolute momentum scale is determined and monitored by analysing $K_S^o \to \pi^+\pi^-$ decays. The resulting systematic error on the mass scale is less than 0.2%.

The distribution of charge deposited on each wire hit by a track is a measure of the ionisation power of a particle and is used to determine its specific energy loss or dE/dx. This energy loss is described by a Landau distribution.

Each dE/dx value needs to be corrected for two effects. First, the amount of charge collected on a wire is strongly dependent upon the angle the track makes with the wire because the track traverses a greater distance in the cell for smaller angles of incidence with respect to the sense wire. Second, owing to timing, the tails of avalanches having large drift distances escape charge measurement. Once these effects have been taken into account, the dE/dx values are averaged, leaving out the largest 30% and smallest 10% to ensure an approximate Gaussian distribution. The specific energy loss for a sample of multihadron events is shown in Figure 5.8.

The drift chamber dE/dx measurements are an important part of the particle identification process, discussed further in Section 5.14.1.

In 1989, the drift chamber was replaced with a version similar to the old. This was necessary because of chamber ageing.

5.7 The Time-of-Flight System (TOF)

The time-of-flight system [46] serves a three fold purpose. Its most important role is to measure charged particle flight times which, in conjunction with re-

dE/dx [keV/cm]
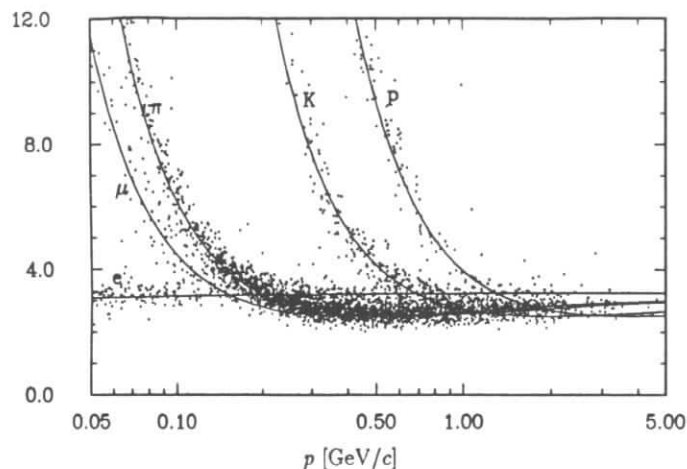
Figure 5.8: Specific energy loss for a multihadron sample of 10 000 events.

constructed track lengths, provide estimates of the particle velocities. These are combined with the drift chamber momenta to identify charged particles by their rest masses. Secondary, but still important, uses are to aid on-line luminosity monitoring and to contribute to the makeup of the fast trigger, both of which are discussed in later sections.

The TOF system forms a cylindrical shell covering 92% of the full solid angle and surrounds the drift chamber, flush with the inside face of the calorimeter. The barrel of the shell comprises 64 scintillation counters, and the endcaps each have 48. The signal from each barrel counter is led to a phototube at each end via light guides, while the endcap counters are viewed by a single phototube each. Because these phototubes require field-free regions to operate, they are located between the coils and the flux return yoke, and are protected from stray fields with 1cm thick soft iron. The light guide cross section must be constant and equal to the size of the phototube cathode. Therefore, the size of the counters was limited by the largest size hole that could safely be made in the yoke without disturbing the flux return.

In order to ensure homogeneous performance of the detector, each phototube is supplied with its own high voltage source. These are adjusted to match all the gains.

To measure the time-of-flight of a particle, a TDC counter is started for each scintillator when a coincidence occurs between the bunch crossing signal and the fast trigger (to be discussed below). The signal output from a counter that has been hit is split so that 80% of it is used to stop its TDC counter after a cable delay correction and a discriminator test. The other 20% is used to measure the charge on the photomultipler tube in order to correct the TDC value for a charge-dependent discriminator crossing time.

The TOF resolution for hadrons is 230ps. Monte Carlo studies, however, indicate that the lowest possible resolution is 170ps [47]. Uncertainty in the bunch crossing time, time instability of the phototubes, and a pulse height correction parametrisation which is invalid for high and low pulse values all account for the discrepancy between these last two values.

From the corrected TOF values and the momentum values obtained from reconstructed tracks in the drift chamber, it is a straight-forward problem to obtain mass estimates for different charged tracks. With this method alone, a three-standard-deviation separation of electrons from pions up to 230MeV/c, pions from kaons up to 700MeV/c, and kaons from protons up to 1200MeV/c can be made. In practice, however, not all charged tracks have mass estimates. In multihadron events, about 80% of charged tracks with p_T greater than 120MeV/c are associated with useful TOF information. Tracks with lower p_T curl up before reaching the TOF counters. In addition, multiple hits on a counter create ambiguity. Figure 5.9 shows M_{TOF}^2 vs momentum for a sample of fast lepton multihadron events.

5.8   The Electromagnetic Calorimeter

The ARGUS electromagnetic shower counters [48] perform the important task of determining the energies of electrons and photons as well as the directions of these photons. In addition, they provide a method for discriminating between hadrons or muons and electrons. Other roles in the ARGUS trigger

m^2_{TOF} [GeV^2/c^4]
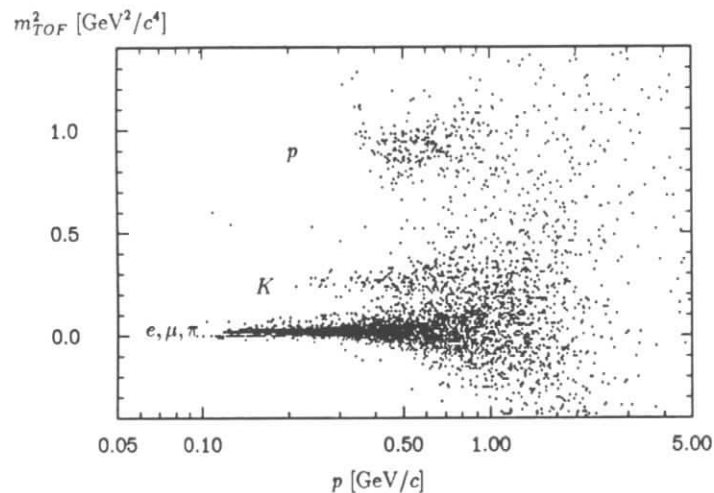
Figure 5.9: Mass squared versus momentum as derived from the ARGUS TOF system.

system and in luminosity monitoring will be discussed in later sections.

The electromagnetic shower counters form a cylindrical section located outside the TOF counters and inside the magnet coils. Installation of the calorimeter inside the solenoids dramatically reduces the amount of material between the counters and the interaction point (as low as 0.16 radiation lengths in the barrel region) thus providing excellent low-momentum photon detection efficiency.

Twenty rings of 64 counters each in the barrel, combined with 5 rings of varying number of counters in each of the endcaps break up the calorimeter into 1760 different segments. Each counter is made of alternating layers of lead and scintillator and has an overall length equivalent to 12.5 radiation lengths. Two different shapes are used to allow compact fitting into the detector. A wavelength shifter is connected to each counter to collect the signal and convey it to a small phototube via an adiabatic light guide. This assembly is then combined with another of the same shape to form a module, the wavelength shifters being sandwiched in the middle but separated by aluminised mylar to prevent cross talk. A quartz light fibre is connected to each counter to allow constant on-line monitoring of the phototubes.

The shower counters constitute an important input for the fast trigger. It becomes necessary therefore to treat variations in phototube gains and module light collection efficiencies in such a way as to equalise trigger thresholds. This is achieved in the same manner as in the TOF system, each phototube being supplied by its own separate, variable, high voltage supply.

The absolute energy calibration of the shower counters is a fairly involved procedure. An electron, positron or photon that is absorbed by the counters produces a pulse height in the photomultiplier output proportional to its energy. In any particular counter the amount of energy converted into light by the scintillators and detected is only a fraction of the actual energy deposited (roughly 30% on average), and depends on the location of the impact point owing to spatial variations in light collection efficiencies and signal transport. In addition, the energy of a particle is deposited over several counters, the amount detected by each varying according to the angle and location of impact. This is an obvious consequence of the non-projective geometry of the

calorimeter, and the interference of its support structure and other dead space contributors. Furthermore, losses along the scintillators and waveguide paths need to to be taken into account. Finally, the photomultipliers are subject to time-dependent gain variations which must be continually monitored in order to correctly interpret pulse heights.

The above complex interplay of factors demands that an iterative procedure be used to determine a set of constants that accurately interpret shower counter signal pulse heights. The electrons and positrons of a sample of 5×10^5 Bhabha events (selected in a manner that minimises the number of radiative Bhabha events) are tracked through the drift chamber in order to determine their positions, directions and momenta when they hit the calorimeter, although the momenta are known quite accurately already from the beam energy. With the aid of a Monte Carlo analysis, a set of three equations relating pulse heights, detector geometry, detector efficiencies, and time-dependent gain variations is solved iteratively to transform known input and output information into information about the effect of the calorimeter on the output signal.

The energy resolution of high energy electrons and positrons is determined from the Bhabha energy spectrum, while that of high energy photons is found similarly with the channel $e^+e^- \rightarrow \gamma\gamma$. Due to the excellent energy resolution for converted photons, the mass distribution of π^0 and η^0 mesons with one converted photon directly reflects the resolution for low energy photons. The resolutions are parametrised as follows:

$$\frac{\sigma(E)}{E} = \sqrt{\left(0.072^2 + \frac{0.065^2}{E[\text{GeV}]}\right)} \qquad \text{(barrel)} \qquad (5.1)$$

$$\frac{\sigma(E)}{E} = \sqrt{\left(0.075^2 + \frac{0.076^2}{E[\text{GeV}]}\right)} \qquad \text{(endcaps)} \qquad (5.2)$$

the constant factor being attributable to the support structure (Monte Carlo result).

While the directions of electrons and positrons in the ARGUS detector are easily derived from drift chamber information, photon directions can only

be determined from shower information. The method used involves weighting the positions of the counters hit with their pulse heights and determining the centre of gravity of the shower for both azimuthal and polar angles. The relation between these calculated values and the true values is determined through Monte Carlo simulation. The angular resolution is determined by applying this procedure to a sample of electrons and positrons from Bhabha scattering events where the directions of impact are known from drift chamber information. Results indicate that a resolution of 13 mrad (equivalent to an average of 1.5 cm in spatial resolution) exists in the barrel region whereas in the endcaps the resolution achieved is better by about 30% due to the smaller counter granularity. The resolution degrades with decreasing photon energy and is obviously physically limited by counter granularity.

The shower counters provide important information for particle identification, especially the separation of electrons from hadrons. First of all, electrons tend to deposit all or most of their energy in the counters. However, hadronic showers will often extend past the shower counters and into the flux return, with the result that only a fraction of the hadronic energy is deposited. Consequently, there is little or no correlation between shower energy and momentum for hadrons, while for electrons there is a strong correlation. Requiring the energy to be within a few standard deviations of the measured momentum excludes a large fraction of hadrons, while maintaining a high efficiency for electrons. Second, hadrons tend to spread their energy over a larger area than electrons. A lateral cut has been devised to take advantage of this fact. Essentially it involves weighting the location of the hit counters with their deposited energy to find the "centre" of the shower and then determining the variance of this distribution after leaving out the two counters with largest energy deposit:

$$E_{lat} = \sum_{i=1}^{n} \frac{(\vec{r}_i - \vec{r})^2 E_i}{<r>^2} \qquad (5.3)$$

$$f_{lat} = \frac{E_{lat}}{(E_{lat} + E_1 + E_2)} \qquad (0 < f_{lat} < 1) \qquad (5.4)$$

This cut only works at higher energies because hadronic showers do not develop below 600MeV. Muons can also be separated from hadrons and elec-

trons because of their high penetration. This manifests itself in a smaller number of counters being hit.

5.9 The Muon Chambers

The muon chambers [49] are capable of detecting charged particles which penetrate through the shower counters and magnet coil. The system of 218 chambers is arranged in three layers, two outside the detector and one just inside the yoke. In total, they cover 93% of the total solid angle. There is a large amount of material between the chambers and the interaction point (3.3 and 5.1 absorption lengths for inner and outer chambers respectively); this inhibits hadronic punchthrough and minimises misidentification. Practical application of the chambers located inside (outside) the coil is restricted to muons of momentum greater than 700MeV/c (1100MeV/c). With the help of off-line cosmic data analysis, the average efficiency for each layer has been determined to be 98%.

Each chamber consists of a side-by-side arrangement of eight proportional tubes of cross sectional area $56 \times 56\text{mm}^2$ and lengths varying between 1m and 4m. These are filled with a nonflammable argon-propane mixture (92:8) and supplied by a voltage which is sufficiently high (2.35 kV) so as not to limit the chamber efficiency. Beam tests indicate that the largest loss of efficiency occurs at the boundary walls of the tubes.

5.10 The ARGUS Trigger

Bunch crossings at DORIS II occur at the rate of about 10^6 per second, although not every bunch crossing results in an interaction observable in the detector. Most of the events that *are* observed are beam-wall or beam-gas interactions and can be rejected. Ideally, the decision to accept or reject an event should be made within $1\mu s$; otherwise, an event occurring at the next crossing will be lost. Limited computer speeds make it impossible to carry out a complete event analysis, and an efficient method must be employed to screen each event quickly. This is the role of the ARGUS trigger system.

Events which are accepted for off-line analysis need to pass a two-stage trigger test. The first-level trigger (fast pretrigger) has to complete the decision making process in one microsecond, and is therefore restricted to information from the TOF and shower counters. This is available within 200ns of the collision. The conditions required for the fast pretrigger to accept an event are discussed below. If an event fails to meet these criteria, all counters are cleared and the trigger returned to a "trigger ready" state. Otherwise, the signals are read out for analysis by the second level trigger (slow trigger). The fast pretrigger then lies in a dormant state until the event is completely transferred to the on-line computer or is vetoed by the second level trigger.

The ARGUS fast pretrigger has a mean output rate of 100Hz. It contributes no deadtime to the overall data taking procedure as its decision to accept or reject an event is made well within the bunch crossing interval. The slow trigger, or "Little Track Finder", reduces the trigger rate by an order of magnitude and introduces a mean deadtime of 0.2% into the detector operation. The largest deadtime contribution results from the transfer of the data to the on-line computer once an event has been accepted. Mean total deadtimes of about (3-10)% were observed during ARGUS operation, depending on background conditions and the first level trigger output rate.

5.10.1 The Fast Pretrigger

The fast pretrigger makes use of TOF and shower counter information by combining counter signals into independent trigger units each of which acts as a single output. These outputs have to satisfy certain conditions in order for the event to be considered further. Four different subtriggers are employed to do this, each having its own individual threshold requirements. Of these only the ETOT trigger uses the endcap regions of the detector.

The total energy trigger (ETOT) requires that the linear sum of shower counter energies in either hemisphere of the calorimeter be greater than 700MeV. (The hemispheres are defined by the plane perpendicular to the beam line through the origin of the detector.) It is used to detect events with balanced energy deposit, e.g. Bhabha scattering. It is also used for

on-line monitoring of the background conditions in the storage ring.

The high energy shower trigger (HESH) segments each hemisphere of the calorimeter into 8 groups of 10 adjacent rows of barrel counters with two rows of overlap between them. Designed to detect particles carrying a large amount of the total energy, it triggers only if the summed energy of any HESH group exceeds about 1GeV.

The charged particle pretrigger (CPPT) consists of 16 trigger units in each hemisphere of the detector. Each unit contains four TOF counters overlapped by six rows of shower counters with adjacent units sharing two rows of shower counters. The trigger searches for events with one or more charged track candidates in each hemisphere by requiring the coincidence of TOF and shower signals as well as a minimum of 50MeV energy deposit in at least one unit per hemisphere.

The coincidence matrix trigger (CMT) combines CPPT groups at the same azimuthal angle in each hemisphere into single CMT units. For a given CMT group signal, at least one of the seven CMT groups opposite in ϕ must also register a signal. This topology is characteristic of low multiplicity tau events and two-photon events.

These four subtriggers, along with an additional cosmic ray trigger (for testing of detector components during periods of no beam) and 0.1Hz pulser (to estimate random noise), are interpreted by the pretrigger collector. Provided the fast subtrigger signals are in coincidence with the bunch crossing signal and another event is not being currently processed (indicated by a "trigger ready" signal discussed below), the pretrigger collector will perform an OR on all pretrigger signals and start further event processing.

5.10.2 The Slow Trigger

The slow trigger or Little Track Finder (LTF) uses drift chamber and TOF information to find tracks in the $r - \phi$ plane. To minimise deadtime and still maintain trigger flexibility, a software supported hardwired device is used to analyse each event as it is accepted by the pretrigger. The chamber and TOF hits are read into wire input boards (WIB). The LTF then accesses

from memory a set of up to 2000 "masks" which contain the hit sequences of possible track roads. The masks are used in conjunction with the WIBs to search for acceptable hit patterns, also stored in memory, within these masks. If the required number of track candidates is found (dependent on pretrigger), the event is accepted and the information obtained by the LTF fed to the on-line computer; otherwise, the electronics are reset and the "trigger ready" state is returned. The procedure has a track finding efficiency of about 97%.

5.11 On-line Data Acquisition

The output from the various ARGUS detector components is collected and digitised by a CAMAC crate system. A system crate controller enables control over the many CAMAC modules according to commands received by the on-line computer.

Data from the CAMAC system is read out in an efficient manner by a fast microprocessor called a CAMAC booster (CAB). Each event can be processed into its final format in less than 1.2 ms. An additional 1.8 ms is required to synchronise the booster with the on-line computer and to transfer all event information to it. Without the booster, the event read-in time would be as high as 40 ms, severely increasing dead time.

The on-line computer, a DEC PDP 11/45, receives data from the CAB on an event-by-event basis and stores it in a buffer. In addition, it is responsible for running the entire data acquisition software, manipulating data flow according to parameters modifiable by the shift operator, and controlling on-line calibration procedures of the various detector components. Events are dumped to a VAX 11/780 in a direct memory access manner that permits high speed transfer of data so as not to impede the data flow rate. The buffering of data in the PDP allows for synchronisation between it and the VAX. The VAX performs some changes in the record format of the events, as well as some monitoring (see below), before dumping data to yet another computer, an IBM. The data are written to a disk data set which is periodically dumped to tape. In the process, the final event format is created and further monitoring carried out. Two raw data tapes, about 80,000 events,

are then concatenated to form permanent EXDATA tapes. These are used for off-line analysis (next section).

Continuous on-line monitoring of the machine, of the detector, and of the data acquisition process is absolutely essential in order to optimise performance and maintain the quality of data collection. This is an important role of the VAX 11/780 computer. As events pass through the VAX buffer, they are unpacked and used to create histograms of some of the more important variables. These are made available directly to the shift operator, allowing immediate recognition of any system failures. The monitoring process includes in part: hit frequencies and pulse heights for all detector components, as well as drift times for DC wires in order to detect ADC or TDC failures; frequency distribution of masks found by the LTF in order to uncover slow trigger failures; rates for all the triggers so as to get an idea of the storage ring background conditions. There is, in addition, a static monitoring system which watches for unacceptably large variations in detector temperatures, gas pressures, magnet current, high voltage, and electronic current supplies.

5.12   Data Analysis

The EXDATA tapes are used for off-line analysis by the ARGUS reconstruction program. This involves several stages of data analysis which will be briefly outlined below. A more detailed description can be found in Ref. [42].

A major step of the program is pattern recognition in the drift chamber. The following five parameters are used to parametrise the helical paths made by charged particles in the magnetic field: κ, the curvature of the helix; d_0, the distance of closest approach to the longitudinal (symmetry) axis of the detector (z − axis); ϕ_0, the azimuthal angle of the track tangent at closest approach; z_0, the z-coordinate of closest approach to the origin; and $\cot\theta$, the cotangent of the angle the track makes with the z − axis. The origin lies on the z − axis at the centre of the detector.

- **Two-Dimensional Pattern Recognition:** This first step of the reconstruction program uses hits among axial wires in the drift chamber

to recognise two-dimensional track projections; rough estimates for κ, d_0, and ϕ are obtained. No actual fitting is done at this stage. Rather, triplets of wire hits are combined and exhaustively searched for circular consistency and similar κ values.

- **Three-Dimensional Pattern Recognition:** This step includes the information from stereo wires as well. When completed, approximate values for all track parameters are available, and all hits are either associated with tracks or thrown out as background.

- **Track Reconstruction:** A rigorous least squares fit of the ideal track, as specified by the track parameters, is made to the drift distance data. Spatial variations of the magnetic field as well as energy losses due to ionisation are taken into account. The fit procedure yields the optimum track parameter values along with their uncertainties. See Chapter 6 for more details.

- **Vertex Chamber Reconstruction:** Each reconstructed track is extrapolated back into the vertex chamber, and a new fit is made with the additional information from VDC hits along its path. See Chapter 6 for more details.

- **Vertex Reconstruction:** The main interaction vertex is determined by fitting as many reconstructed tracks as possible to a common point of origin. Tracks that fit poorly to this main vertex are excluded. A search for secondary vertices (K_S^0 decay, Λ^0 decay, photon conversion) is then carried out using these rejected tracks. A final attempt is made to associate tracks from the main vertex with any of these new vertices. See Chapter 6 for more details.

- **TOF Reconstruction:** The reconstruction of particle times-of-flight is carried out. Tracks from the main drift chamber are associated with hits recorded in the TOF counters, and assigned velocities.

- **Shower Counter Reconstruction:** The energies and positions of particles interacting with the calorimeter are determined. The shapes

of the reconstructed showers are used for particle identification.

- **Muon Chamber Analysis:** An attempt is made to assign each hit in the muon chambers to a charged track. This information is then used for particle identification.

EXDATA events analysed by the ARGUS program, and which either 1) have at least two tracks pointing to the interaction region or 2) are consistent with $e^+e^- \rightarrow \gamma\gamma$, $e^+e^- \rightarrow \gamma\gamma\gamma$, or Bhabha events, are written to EXPDST tapes. This first criterion is an attempt to reduce beam-wall and beam-gas events. Beam-wall events arise from beam particles that suffer small momentum changes upstream due to bremsstrahlung or Coulomb scattering by residual molecules in the vacuum. These particles become poorly focused and can strike the beam wall. Beam-gas events are a result of imperfect vacuum conditions. The EXDATA tapes contain many unwanted background events due to these two types of interactions. Because these events generally originate far from the collision point for the beams, one can significantly reduce the number of unwanted events by demanding that at least some tracks be traceable to the interaction region.

Bhabha events are maintained in this selection so as to provide a means of calculating the luminosity as discussed in Section 5.13 below. These events, however, are excluded from the next and final stage of data selection relevant to this analysis, the creation of EXMUHA or multihadron tapes. Events selected in this stage must have at least three tracks pointing to the main vertex or an energy deposit of at least 1.7GeV in the shower counters.

5.13   Luminosity Measurement

The luminosity is determined from the pure QED, and hence well understood, Bhabha scattering process $e^+e^- \rightarrow e^+e^-$. By counting the rate of these events occurring within a given solid angle, the differential luminosity can be ascertained to be

$$L = \frac{dN_{Bhabha}}{dt} / \sigma_{Bhabha}.$$

Fast on-line luminosity measurements are carried out in order to get some idea of the rate of data intake and quality of machine performance. A more careful analysis of the luminosity is performed off-line.

The on-line monitoring process employs the endcaps of the calorimeter, as well as the TOF counters directly in front of them. Each endcap is segmented into 8 sectors of 22 shower counters and 3 TOF counters each. Bhabha events are isolated by requiring an energy deposit of at least 1Gev into each of two diagonally opposite sectors, along with a coincidence of TOF and shower counter signals for each sector. Using the Bhabha cross section for the endcap solid angle,

$$\sigma_{Bhabha} = 58\text{nb} \times \frac{100\text{GeV}^2}{E_{cm}^2},$$

the number of Bhabha events can be converted into an on-line luminosity measurement.

The off-line luminosity measurement involves fully reconstructed Bhabha events from the barrel alone. Tracks must have momentum greater than 1GeV/c, shower energy greater than 0.6GeV, and form an opening angle of not less than 165 degrees. Using a Monte Carlo simulation, the total radiatively corrected Bhabha cross section for these cuts is determined to be [50]

$$\sigma_{Bhabha} = 11.38\text{nb} \times \frac{100\text{GeV}^2}{E_{cm}^2},$$

correct to within about $\pm 1.8\%$.

5.14   Charged Particle Identification

5.14.1   Likelihoods for General Particle Identification

Charged particles are identified by reconstructing particle masses through the use of time-of-flight and dE/dx measurements combined with momentum information from the drift chamber. Depending on the particle momentum, unambiguous identification of a particle may not be possible. In practice, a likelihood function is developed enabling the experimenter to make probability cuts for allowed mass hypotheses. A track is considered to be a pion, for

example, if the normalised likelihood (defined below) for the pion hypothesis is greater than some value, usually of the order of 1% to 5%.

The likelihood function is developed from χ^2 values determined for each particle from dE/dx and TOF measurements. From specific energy loss measurements, one computes for each hypothesis,

$$\chi_i^2(dE/dx) = \frac{(dE/dx - dE/dx_i^{th})^2}{\sigma_{dE/dx}^2 + \sigma_{th}^2} \qquad (i = e, \mu, \pi, K, p) \qquad (5.5)$$

where dE/dx_i^{th} is the specific energy loss value expected from theory. The uncertainty in the theoretical values derives from the uncertainty in the momentum. From time-of-flight measurements a similar expression is constructed:

$$\chi_i^2(TOF) = \frac{(1/\beta - 1/\beta_i^{th})^2}{\sigma_{TOF}^2 + \sigma_{th}^2} \qquad (i = e, \mu, \pi, K, p). \qquad (5.6)$$

Here β is the particle velocity determined from TOF measurements and σ_{th} once again arises from an imperfect knowledge of the particle momentum. Because the two sets of χ^2 values are derived from completely independent measurements, one can combine them to form a single set of χ^2 values for each hypothesis,

$$\chi_i^2 = \chi_i^2(dE/dx) + \chi_i^2(TOF). \qquad (5.7)$$

The likelihood function for each hypothesis is then given by

$$L_i = exp(-\chi_i^2/2) \qquad (5.8)$$

and used to calculate normalised likelihood ratios:

$$\lambda_i = \frac{w^i L_i}{\sum_{k=e,\mu,\pi,K,p} w^k L_k}. \qquad (5.9)$$

Here, the weights w^i are used to take into account *a priori* relative particle abundances. About 80% of all measured charged particles can be unambiguously identified with TOF and dE/dx information.

5.14.2   Likelihoods for Lepton Identification

Section 5.14.1 describes how charged tracks are assigned possible mass hypotheses using TOF and dE/dx measurements. For lepton identification, information beyond TOF and dE/dx values is available and can be incorporated into the likelihood function to provide a better rejection of background [42].

The interaction of electrons with the shower counters is quite different from that of hadrons and muons. As has already been discussed in this chapter, there exists a strong correlation between electron momentum and shower energy deposit, but no such correlation exists for hadrons. Also, the lateral spread of showers is much more compact for electrons than it is for hadrons. Muons appear as minimum ionising particles in the counters and can be clearly separated from electrons. Based on these observations, a likelihood function particular to electrons was developed. From measured parameter values, the probability p_i^k that a track belongs to a particular hypothesis k is determined for each method i capable of distinguishing electrons, and a normalised likelihood function is computed as

$$\lambda^e = \frac{w^e \cdot \prod_{i=TOF,dE/dx,SC} p_i^e}{\sum_{k=e,\mu,\pi,K,p} w^k \prod_{i=TOF,dE/dx,SC} p_i^k} \qquad (5.10)$$

where the weights w^k reflect particle abundances. This likelihood function, termed $LHEWES$, is an extremely powerful tool for distinguishing electrons. The efficiency for identifying electrons is well over 90% for momenta greater than 500MeV/c and the misidentification rate less than half a percent.

Muons are identified with a similar likelihood function, but information from the muon chambers is used as well. If a reconstructed track cannot be assigned to a hit in the muon chambers, the muon hypothesis is immediately rejected. Electrons, which are always absorbed in the detector before reaching the muon chambers, cannot survive this restriction and are therefore not considered as one of the hypotheses in this likelihood function, which is given

by

$$\lambda^\mu = \frac{w^\mu \cdot \prod\limits_{i=TOF,dE/dx,SC,\mu} p_i^\mu}{\sum\limits_{k=\mu,\pi,K,p} w^k \prod\limits_{i=TOF,dE/dx,SC,\mu} p_i^k}. \qquad (5.11)$$

Once again, this is a very powerful method for distinguishing muons. Due to hadronic punchthrough and muons decaying in-flight, the misidentification rate is of the order of 2% for pions and kaons [42].

Chapter 6

Tracking and Vertexing Algorithms

6.1 Introduction

The information used to measure the tau lifetime in this analysis is obtained solely from the charged decay products of tau lepton pairs. These particles travel outwards from the interaction point and through the various materials in the detector, traversing two drift chambers along the way, the VDC and DC. As described in Chapter 5, these devices are capable of recording which cells in the ARGUS detector have had charge deposited in them, and when with respect to the event start this charge deposition occurred. They therefore provide the means of detecting charged particles and reconstructing their paths through space. This chapter describes in detail how this wire hit and timing information is translated into a precise geometrical description of each track at the beam line. This tracking information can then be employed to estimate where the tau particles are produced (vertexing).

6.2 The Track Parameters

It is easiest to describe the tracking approach at ARGUS by first dealing with an ideal detector and then handling the actual case. In what follows, the "detector" is to be understood as being a drift chamber.

6.2.1 The Ideal Detector

Neglecting all materials, particles travelling through the fiducial volume of a detector undergo no interactions other than their interaction with the magnetic field. If this is constant in magnitude and direction, then the particles travel in perfect helices about the field direction (assumed to be along the z axis). In general, any helix can be completely defined by specifying five parameters. A convenient set for tracking breaks down into parameters describing the projection of the helix onto the plane perpendicular to the magnetic field (a circle = 3 parameters) and those describing the motion projected onto the field direction (a line = 2 parameters). Thus, any track in this ideal detector can be described with five parameters.

Each drift cell traversed by a particle yields information capable of determining the closest distance a particle comes to it. Through a pattern recognition process, one tries to reconstruct each set of hits belonging to a common track. It is then a fairly simple matter to determine the helix parameters which best satisfy the hit information. For chambers having axial (z) wires alone, as is the case with the VDC, information about the track path in the z direction is unavailable and only the projection onto the plane perpendicular to the field can be reconstructed. Chambers with, in addition, wires tilted with respect to the magnetic field, as in the cases of the DC and μVDC, are also sensitive to the z-coordinate.

6.2.2 The Real Detector

Unfortunately, such an ideal tracking detector lies in the realm of fiction. More realistically, the wires in the detector are of finite size and the gas of reasonable density, therefore tracks lose energy and scatter in the detector volume and do not in general respect the strictly helical form. The wires provide sites for bremsstrahlung and photon conversion. The magnetic field varies with position and needs to be mapped. The wires are subject to sag, creep, electrostatic effects, imprecise positioning, and temperature changes in the endplates where they are seated. The chamber needs to be calibrated so that the timing information from hit wires yields correct drift distances,

but since this usually requires using the detector itself as a calibrator the end result can be plagued with systematic biases. Also, because the environment inside the detector volume (temperature, pressure, gas mixture, wire voltages) as well as the electronics environment outside (TDCs, ADCs, crates, cables) are constantly changing, several calibrations need to be done over the course of data-taking. This makes the real tracking detector a very complex device.

6.3 Defining and Tracing Tracks

6.3.1 Definition of Track Parameters

The geometric centre of the main drift chamber defines the origin of the ARGUS coordinate system. The x- and y-axes are in the horizontal and vertical directions, respectively, and the positive z-axis is along the symmetry axis of the chamber, in the direction of the positron beam (see Figure 5.2). In addition to this Cartesian coordinate system, a mixture of cylindrical and polar coordinates is employed. For a given point: r is the perpendicular distance from the z-axis to this point; ϕ is the angle that the vector from the origin to this point, projected onto the x-y plane, makes with respect to the x-axis; and θ is the angle that a vector from the origin to this point makes with respect to the positive z-axis. Mathematically, the relation between these coordinates is:

$$
\begin{aligned}
r &= \sqrt{x^2 + y^2} \\
\tan \phi &= y/x \\
\cot \theta &= z/\sqrt{x^2 + y^2}.
\end{aligned}
$$

Unit vectors along the x, y, z, r, and ϕ directions are denoted by $\vec{e_x}$, $\vec{e_y}$, $\vec{e_z}$, $\hat{r}$, and $\hat{\phi}$, respectively.

A track in the ARGUS coordinate system is defined by five parameters specified at a reference point $\vec{x}_o$ along the track. In the VDC and DC track fits, this is given by the point of closest approach of the track to the first hit wire. For tracks traced to the beamline, it is given by the point of closest

approach to an estimate of the beam position, typically chosen to be the origin of the ARGUS coordinate system. For the latter case, the five track parameters are:

- d_o - the distance from the origin to the reference point defined above, projected onto the x-y plane and multiplied by a sign factor defined below;

- z_o - the z-coordinate of the reference point;

- κ - the track curvature (inverse of the bending radius), endowed with the same sign as the charge of the track;

- $\cot \theta$ - cotangent of the angle the track makes with respect to the z-axis; and

- ϕ_o - the direction ϕ of the track tangent in the x-y plane.

The sign of d_o depends on which side of the origin the track passes. Explicitly,

$$
d_o = (\vec{x}_o - \vec{x}_{orig}) \cdot \frac{(\vec{e_z} \times \hat{t})}{\|\vec{e_z} \times \hat{t}\|},
$$

where $\hat{t}$ is the track tangent unit vector. For the DC and VDC fits $\vec{x}_{orig}$ is replaced with the point on the first wire that is closest to the track.

6.3.2 Tracking in a Constant Magnetic Field

Figure 6.1 shows the $x - y$ projection of the trajectory of a positively charged particle moving in a constant magnetic field directed along the positive z axis. The circular nature of the path can be easily derived using the Lorentz force acting on a charge Q moving with velocity $\vec{v}$ in an electric field $\vec{E}$ and magnetic field $\vec{H}$:

$$
\vec{F} = \frac{d\vec{p}}{dt} = Q(\vec{E} + \vec{v} \times \vec{H}). \tag{6.1}
$$

In the absence of an electric field this implies that the force on the charge is always perpendicular to its velocity $\vec{v}$ and lies in the plane perpendicular to the magnetic field with magnitude

$$
F_{field} = QvH \sin \theta = \frac{QpH \sin \theta}{m} = \frac{QHp_T}{m} \tag{6.2}
$$
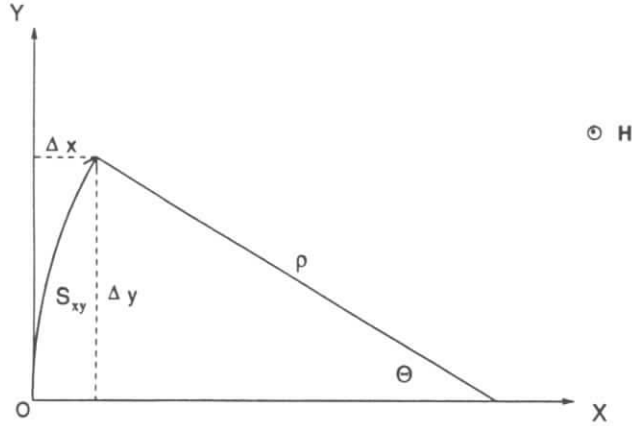
Figure 6.1: Projection onto $x - y$ plane of trajectory of positively charged particle moving in a magnetic field directed along the z-axis.

where p and m are the momentum and mass of the particle, respectively, and θ is the polar angle between the field and the particle direction. Equating this to the centrifugal force experienced by a particle of mass m moving in a circle with radius ρ and momentum p_T,

$$F_{centr} = \frac{p_T^2}{m\rho},$$ (6.3)

it follows immediately that the particle describes a circle with radius

$$\rho = \frac{p_T}{QH},$$ (6.4)

Hence, the radius is directly proportional to the momentum component transverse to the field. Because there is no longitudinal force, the particle executes helical motion about the direction of the field maintaining the same angle θ with respect to this direction at all times. The sign of ρ reflects the charge of the particle: for positive Q the track curves clockwise when viewed against the field direction, and counter clockwise for negative Q. It follows then (see

Figure 6.1) that if the particle starts at the origin

$$\vec{x}_o = \begin{pmatrix} 0 \\ 0 \\ 0 \end{pmatrix}$$ (6.5)

with direction

$$\vec{t}_o = \begin{pmatrix} 0 \\ \sin\theta \\ \cos\theta \end{pmatrix}$$ (6.6)

then after a projected step of $s_{xy} = s \cdot \sin\theta$ its new position will be

$$\vec{x}(\Theta) = \rho \begin{pmatrix} 1 - \cos\Theta \\ \sin\Theta \\ \Theta\cot\theta \end{pmatrix}$$ (6.7)

where s is the distance along the track in three dimensions, and Θ is the *turning angle*, a convenient (signed) parameter for tracing the track:

$$\Theta = \frac{s_{xy}}{\rho} = \frac{s \cdot \sin\theta}{\rho}.$$ (6.8)

Differentiation of this expression with respect to s yields the new direction:

$$\frac{d\vec{x}(s)}{ds} = \vec{t}(s) = \sin\theta \cdot \begin{pmatrix} \sin\Theta \\ \cos\Theta \\ \cot\theta \end{pmatrix}.$$ (6.9)

A more rigorous derivation of these equations can be carried out by solving Equation 6.1 directly. By taking the dot product of both sides of this equation it can be explicitly shown that the momentum, and therefore the velocity, of the particle is constant:

$$\begin{aligned} \vec{p} \cdot \frac{d\vec{p}}{dt} &= \vec{p} \cdot \left(Q\vec{v} \times \vec{H} \right) \\ \frac{1}{2}\frac{d}{dt}(\vec{p}.\vec{p}) &= \vec{p} \cdot \left(\frac{Q}{m}\vec{p} \times \vec{H} \right) = 0 \\ \Longrightarrow \vec{p}^{\,2} &= p^2 = constant. \end{aligned}$$

Using this fact, and making a change of variables in the derivative

$$\frac{d}{dt} \to \frac{1}{v}\frac{d}{ds},$$

which follows from the velocity relation for the particle

$$v = \frac{ds}{dt},$$

Equation 6.1 can be recast in simpler form in terms of the track tangent unit vector $\vec{t} = \vec{v}/v$:

$$\frac{d\vec{p}}{dt} = Q\vec{v} \times \vec{H}$$
$$m\frac{d\vec{v}}{dt} = Q\vec{v} \times \vec{H}$$
$$\frac{d\vec{t}}{ds} = \frac{Q}{mv}\vec{t} \times \vec{H}$$
$$\frac{d\vec{t}}{ds} = \frac{Q}{p}M\vec{t}, \tag{6.10}$$

where

$$M = \begin{pmatrix} 0 & H_z & -H_y \\ -H_z & 0 & H_x \\ H_y & -H_x & 0 \end{pmatrix} \tag{6.11}$$

For constant magnetic field this differential equation has the general solution

$$\vec{t} = e^{\frac{Qs}{p}M}\vec{t}_o \tag{6.12}$$

If the field is directed along the z axis, $\vec{H} = (0, 0, H)$, then the expression for $\vec{t}$ becomes

$$\vec{t} = e^{\frac{QsH}{p}\lambda}\vec{t}_o, \tag{6.13}$$

where

$$\lambda = \begin{pmatrix} 0 & 1 & 0 \\ -1 & 0 & 0 \\ 0 & 0 & 0 \end{pmatrix}. \tag{6.14}$$

Expanding the exponential into its Taylor series and using the fact that

$$\lambda^3 = -\lambda^5 = \lambda^7 = \dots = \lambda$$

and $\quad -\lambda^2 = \lambda^4 = -\lambda^6 = \dots = \begin{pmatrix} 1 & 0 & 0 \\ 0 & 1 & 0 \\ 0 & 0 & 0 \end{pmatrix} \tag{6.15}$

yields

$$\begin{pmatrix} t_x \\ t_y \\ t_z \end{pmatrix} = \begin{pmatrix} \cos(\frac{QHs}{p}) & \sin(\frac{QHs}{p}) & 0 \\ -\sin(\frac{QHs}{p}) & \cos(\frac{QHs}{p}) & 0 \\ 0 & 0 & 1 \end{pmatrix} \begin{pmatrix} t_x^o \\ t_y^o \\ t_z^o \end{pmatrix}. \tag{6.16}$$

For a track with initial direction $\vec{t}$ as in Figure 6.1, i.e. $(t_x^o, t_y^o, t_z^o) = (0, \sin\theta, \cos\theta)$, the final expression for the track tangent after a step s becomes

$$\begin{pmatrix} t_x \\ t_y \\ t_z \end{pmatrix} = \begin{pmatrix} \sin(\frac{QHs}{p})\sin\theta \\ \cos(\frac{QHs}{p})\sin\theta \\ \cos\theta \end{pmatrix} = \sin\theta \begin{pmatrix} \sin(\Theta) \\ \cos(\Theta) \\ \cot\theta \end{pmatrix}. \tag{6.17}$$

where

$$\Theta = \frac{QHs}{p}. \tag{6.18}$$

That this is the same Θ as in Equation 6.8 can be seen by substituting Equation 6.4 into Equation 6.8 and using $p_T = p\sin\theta$. Integrating Equation 6.17 using

$$\vec{t} = \frac{d\vec{x}}{ds} \tag{6.19}$$

yields

$$\begin{pmatrix} x \\ y \\ z \end{pmatrix} = \int_0^s \begin{pmatrix} t_x(s') \\ t_y(s') \\ t_z(s') \end{pmatrix} ds' = \frac{p\sin\theta}{QH} \begin{pmatrix} 1 - \cos\Theta \\ \sin\Theta \\ \Theta\cot\theta \end{pmatrix}, \tag{6.20}$$

which using Equation 6.4 yields Equation 6.7.

6.3.3 Tracking in Varying Magnetic Field

Although the magnetic field in ARGUS is directed along the z-axis of the ARGUS detector system at the beam line, in general it develops a small radial component for other positions in the detector. In such a position-dependent magnetic field $\vec{H}(\vec{x})$ the basic tracing equations 6.7 and 6.17 remain applicable provided the trace is broken up into segments within which the field is assumed to be constant. Thus the track can be described with a set of linked helices. For the ARGUS drift chamber track fit each link is typically of the order of 2cm in length, roughly the distance between wire layers in the drift

chamber, with a maximum link size of 4cm allowed. This is good enough to keep the tracking inaccuracy well below the resolution of the chamber.

Because the tracing equations are derived for the specific case where the field is directed along the z-axis, a local coordinate system is adopted in each helical segment. At the point $\vec{x}_i$ of the ith step this is defined by the following unit vectors:

$$\begin{aligned}
\vec{h}_i &= \frac{\vec{H}(\vec{x}_i)}{|\vec{H}(\vec{x}_i)|} \\
\vec{n}_i &= \frac{\vec{t}_i \times \vec{h}_i}{|\vec{t}_i \times \vec{h}_i|} \\
\vec{b}_i &= \vec{h}_i \times \vec{n}_i \,.
\end{aligned} \qquad (6.21)$$

The ordered vector triplet $(\vec{n}_i, \vec{b}_i, \vec{h}_i)$ defines an orthonormal righthanded coordinate system. The initial orientation of the momentum and field in this coordinate system is identical to that assumed for the $\vec{e}_x, \vec{e}_y, \vec{e}_z$ frame considered earlier. Therefore those results can be adopted immediately and a step from $\vec{x}_i$ to $\vec{x}_{i+1}$ in the ARGUS frame is given by

$$\vec{x}_{i+1} = \vec{x}_i + \rho \left[(1 - \cos \Theta_i) \cdot \vec{n}_i + \sin \Theta_i \cdot \vec{b}_i + \Theta_i \tan \lambda_i \cdot \vec{h}_i \right], \qquad (6.22)$$

with new tangent

$$\vec{t}_{i+1} = \cos \lambda_i \cdot (\sin \Theta_i \cdot \vec{n}_i + \cos \Theta_i \cdot \vec{b}_i + \tan \lambda_i \cdot \vec{h}_i), \qquad (6.23)$$

where the *dip angle* λ is defined through the relation

$$\sin \lambda_i = \vec{t}_i \cdot \vec{h}_i \,. \qquad (6.24)$$

For the special case where $\vec{h}_i$ is oriented along the ARGUS z-axis $\vec{e}_z$, the dip angle corresponds to the complement of the polar angle θ, i.e,

$$\lambda = \frac{\pi}{2} - \theta \,. \qquad (6.25)$$

6.4 Accounting for Energy Loss and Multiple Scattering

Equations 6.22 and 6.23 enable a track of known initial momentum and position to be traced step-by-step through a vacuum. (How these initial

conditions are determined is the subject of Section 6.5 wherein the DC and VDC track fits are described.) The volume inside the ARGUS beam pipe can safely be treated as a vacuum for tracking purposes, but this certainly is not the case for the rest of the chamber. As a particle traverses the drift chamber, for example, it loses energy, primarily through ionisation of the DC gas. It also suffers from multiple Coulomb scattering off nuclei. For a hadron there is the additional possibility of a strong interaction with the material, while for an electron or positron bremsstrahlung can take place in the field of a nucleus or wire. These interactions destroy the ideal orbit defined above. Fortunately, the two dominant effects, energy loss and multiple scattering, can be reasonably well determined. For a particle mass $m > m_e$ moving with velocity βc in a material of density ρ the Bethe-Bloch equation [1],

$$\frac{dE}{dx} = \frac{DZ\rho}{A} \cdot \frac{1}{\beta^2} \left[\ln \left(\frac{2m_e c^2 \gamma^2 \beta^2}{I} \right) - \beta^2 \right] \qquad (6.26)$$

describes the mean change in its energy per distance travelled, where Z and A are the charge and mass number of the medium, I is its average excitation potential, and D is a constant equal to $.3070 MeV \mathrm{cm}^2/\mathrm{gram}$. This formula can be used to determine the change in magnitude of momentum a particle suffers on average upon traversing a chamber wall, for example, allowing the momentum to be updated accordingly. To determine the change in momentum, however, an hypothesis for the particle identity is required to fix the mass. This is normally provided by the analysis of energy loss in the drift chamber described in Chapter 5, although a mass hypothesis can be forced. Multiple scattering is typically an elastic process which leaves the particle energy unchanged but modifies its direction. In performing a trace of a particle through the detector it is impossible to know *a priori* whether it scatters at some point and so no attempt to modify the track parameters is made as in the case of energy loss. Instead, the *errors* on the parameters ϕ and θ resulting from the track fit (described below) are inflated to reflect the increased uncertainty in direction. The distribution of angular deviations about the original direction, projected onto a plane, is unfortunately not Gaussian, but has long large angle scattering tails. However, the central

98% can be modelled by a Gaussian of width θ_o by [1]

$$\theta_o = \frac{13.6 MeV}{\beta c p} Z \sqrt{x/X_o} \left[1 + 0.038 \ln(x/X_o)\right] \qquad (6.27)$$

where p is the particle momentum and x/X_o the length of material traversed in radiation lengths. This formula is used to blow up the track angle parameters. The large angle tails are not taken into account.

In practice these adjustments for energy loss and multiple scattering are not performed every time a track is traced through a material in the detector. Instead, the various materials are considered to be grouped together into two scattering radii at 4.3cm and 14.9cm and the tracks adjusted at these points only. The first radius includes materials like the beam tube and inner VDC wall, the second the outer VDC wall and inner DC wall. The values for these radii are determined from weighted averages of the materials using their widths in units of radiation length.

6.5 Fitting Tracks

The ARGUS track fit is a three step procedure involving 1) a track fit in the main drift chamber using timing information from the DC wire hits assigned to the track; 2) inclusion of VDC hit information using a semi-independent VDC fit; and 3) a vertex fit procedure which attempts to associate each track with the main vertex or secondary vertex. The following is a short description of each of these steps. A more detailed description can be found in [42].

6.5.1 The DC track fit

Once the pattern recognition procedure has found a set of N wires common to a track, the following χ^2 expression is minimised with respect to the five-dimensional column vector, q, of the track parameters:

$$\chi^2 = (d_{meas} - d(q))^T W (d_{meas} - d(q)), \qquad (6.28)$$

where

- d_{meas} is the N-dimensional column vector of measured drift distances;

- $d(q)$ is the N-dimensional column vector of the fitted drift distances, calculated using the track parameter set q as described below; and

- W is the $N \times N$ diagonal matrix of the measured drift distance weights, $W_{ii} = 1/\sigma_i^2$, where σ_i is the uncertainty in the measured drift distance $d_{meas,i}$.

The vector d_{meas} and matrix W are specified by the measured drift times using the drift chamber distance-time-relation and resolution function (see Chapter 7). The vector $d(q)$ is determined by the fit: For a given set of track parameters q, the position $\vec{x}_i$ and tangent vector $\vec{t}_i$ of the track near wire i can be found using the tracing Equations 6.22 and 6.23. (Energy loss is taken into after each step in the track trace, by updating the track momentum using Equation 6.26.) Then, for a wire with direction $\vec{w}_i$ and passing through the point $\vec{W}_{o,i}$ in the $z = 0$ plane, the distance of closest approach of the track to the wire is given by

$$d_i = (\vec{x}_i - \vec{W}_{o,i}) \cdot \vec{a}_i \qquad (6.29)$$

where

$$\vec{a}_i = \frac{(\vec{w}_i \times \hat{t}_i)}{\|\vec{w}_i \times \hat{t}_i\|}$$

is the axis along which d_i is measured. A given measured drift distance $d_{meas,i}$ is assigned the same sign as its fitted distance, d_i.

Equation 6.28 is minimised by linearising its dependence upon the track parameter set q and iterating. For the nth iteration, an approximate expression for $d(q_n)$ can be written using the first two terms of its Taylor expansion about q_{n-1}:

$$\begin{aligned} d(q_n) &\approx d(q_{n-1}) + \sum_{\mu=1}^{5} \left.\frac{\partial d}{\partial q_\mu}\right|_{q=q_{n-1}} (q_n - q_{n-1})_\mu \\ &= A(q_n - q_{n-1}) + d(q_{n-1}) \\ &= A \Delta q_n + d(q_{n-1}), \end{aligned} \qquad (6.30)$$

where A is the Jacobian matrix of $d(q)$ evaluated at $q = q_{n-1}$,

$$A = \frac{\partial d}{\partial q}\bigg|_{q=q_{n-1}} = A_{i\mu} = \left(\frac{\partial d_i}{\partial q_\mu}\right)_{\substack{i=1,...,N \\ \mu=1,...,5}},$$

and Δq_n is the vector of changes in the track parameters given by

$$\Delta q_n = q_n - q_{n-1}. \tag{6.31}$$

For the first iteration, q_{n-1} is provided by the pattern recognition procedure. Substituting Equation 6.30 into Equation 6.28 yields

$$\begin{aligned}\chi_n^2 &= [d_{meas} - d_{n-1}]^T W [d_{meas} - d_{n-1}] \\ &\quad -2\Delta q_n^T A^T W [d_{meas} - d_{n-1}] + \Delta q_n^T A^T W A \Delta q_n.\end{aligned}$$

Setting the derivative of this with respect to q_n to zero (A is considered constant) yields a matrix equation for the parameter corrections Δq_n,

$$A^T W A \Delta q_n = A^T W [d_{meas} - d(q_{n-1})]. \tag{6.32}$$

Solving for Δq_n and using Equation 6.31 yields an improved solution, q_n, for the track parameters. This process is repeated until convergence. The parameter covariance matrix V is given by [1]

$$V = \left(A^T W A\right)^{-1}. \tag{6.33}$$

The above procedure requires the calculation of the derivatives $\frac{\partial d(q)}{\partial q}$, in order to determine the matrix A. These can be derived from expression 6.22. See reference [42] or [51] for more details.

For low momentum tracks, the track trajectory is broken up into segments to allow for N_{MS} multiple scattering kinks. The maximum length of these segments is set by the requirement that the expected deviation due to multiple scattering, within any segment, be small compared to the chamber resolution. The expression 6.28 is modified accordingly:

$$\chi^2 \rightarrow \chi^2 + \sum_i^{N_{MS}} \frac{\delta_i^2}{\sigma_{MS,i}^2}. \tag{6.34}$$

where δ_i is the ith kink angle in the x-y plane, and $\sigma_{MS,i}$ is the expected width of the angular deviation due to multiple scattering (see Equation 6.27). The track fit then becomes an $N_{MS} + 5$ parameter fit.

The fit described above is the heart of the procedure used to determine the parameters of a track. The full procedure involves several passes, and includes the following features:

- Once the fit converges, the sign of any measured drift distance is flipped to see if it yields an improved χ^2. If, for a given wire, no sign yields a satisfactory χ^2 contribution to the fit, the wire is discarded and the track fit is repeated.

- An attempt is made to include wire hits not assigned to the track by the original pattern recognition procedure.

- For very low momentum tracks, the order of the wires is reversed and the track fit repeated to see if it yields an improved χ^2.

- The pattern recognition procedure is repeated for wires rejected from the track fit, wires from tracks thrown out due to a poor track fit χ^2, and wires belonging to tracks containing too few hits.

The final parameter set q, along with its covariance matrix V, resulting from the above procedure, define a *DC track*. If VDC information is not available, or too few VDC hits can be associated with the track (see next section), the DC track is swum to the beam line for further consideration by the vertex fitting procedure. The track parameter swim has already been described. The track covariance matrix V is propagated along with the track parameters using the formula [1]

$$V(q_\rho', q_\sigma') = \sum_{\mu,\nu} \frac{\partial q_\rho'}{\partial q_\mu} \cdot \frac{\partial q_\sigma'}{\partial q_\nu} \cdot V(q_\mu, q_\nu). \tag{6.35}$$

This formula is completely general and is used to update the covariance matrix whenever a track is traced from one point to another.

6.5.2   The Semi-independent VDC track fit

In an attempt to include VDC information, each DC track is traced backwards into the VDC, taking into account energy loss in the inner DC and outer VDC walls. A pattern recognition process attempts to associate VDC wire hits with the DC track. For low momentum tracks, several possible "roads" are searched depending upon the expected r.m.s. angle deviation due to multiple scattering in the walls, and the road which picks up the most hits is used as input to the semi-independent VDC track fit. This is a fit to the VDC hit information, in a manner similar to the DC fit, but with an added term in the χ^2 expression which incorporates the DC track information as a constraint:

$$\chi^2 = \sum_{\substack{i=1 \\ VDC}}^{N} \frac{(d_{meas,i} - d_i(q))^2}{\sigma_i^2} + (q - q_{DC})^T V_{DC}^{-1} (q - q_{DC}). \qquad (6.36)$$

Here, q_{DC} and V_{DC} are the track parameter set and track covariance matrix, respectively, of the DC track, evaluated at the same point as that used to define the updated track parameter set q. This is normally the point of closest approach to the innermost hit wire of the VDC.

In the fit, one of two approaches is used to incorporate the kink introduced by the treatment of scattering in the walls. Either 1) the DC track covariance matrix is updated, during the swim through the walls, with larger uncertainties in the parameters σ_ϕ and $\sigma_{\cot\theta}$, as discussed in Section 6.4, or 2) the χ^2 expression 6.36 is updated to include a contribution from a multiple scattering kink in ϕ at the wall, in direct analogy to 6.34. The two approaches yield similar results. For the lifetime analysis, the latter approach is used.

In a manner similar to the DC track fit, the VDC fit is performed several times: the sign of the drift distances are switched to test for a better χ^2, an attempt is made to include hits not originally assigned to the track by pattern recognition, and hits are rejected if their χ^2 contribution to the fit is too high. However, kinks are not incorporated into the orbit to compensate for multiple scattering.

If not enough VDC hits can be assigned to the track (a minimum of four is the default), the VDC information is rejected all together, and the

track remains a DC track. Otherwise, the track parameter set resulting from combining DC and VDC information is considered for further analysis. This is termed a *VDC track*. Only VDC tracks are used in the lifetime analysis.

6.6   Vertex Fitting

6.6.1   Standard ARGUS Fit Algorithms

There are two standard methods available in the ARGUS reconstruction code, for carrying out vertexing: 1) a simple weighting procedure that uses only d_o and z_o track information (and the corresponding submatrix of the full covariance matrix) to find the most likely vertex for a set of tracks [42], and 2) a modified track parameter fit procedure that uses all the track information (5 parameters and complete covariance matrix), and forces the tracks to pass through a common point by adjusting the track parameters within the constraints of the covariance matrices. The first method is not used in the lifetime analysis, and the reader is referred to [42] for a more detailed description. The second method is employed solely for the purpose of rejecting background events that have secondary vertices (Section 8.4.7). As this is a minor part of the analysis, the reader is again referred to the literature for details [52, 53].

6.6.2   Beam Tube Fit Algorithm

To carry out the three-prong vertex fit, a new algorithm, based on the principle of method (2) above, was implemented by the author. The decision to write a new vertex fit algorithm came from a suggestion from [54]. The algorithm, termed the beam tube fit (BTF) algorithm, makes use of the fact that, to an excellent approximation, the magnetic field in the beam tube is constant in magnitude and direction, $\vec{H}(r, z) = H_o \vec{e_z}$. This allows a few improvements to be made over algorithm (2). For example, in algorithm (2), tracks are repeatedly traced until convergence, a procedure subject to rounding errors. This is avoided in the BTF algorithm, which is also faster, and yields a more accurate vertex parameter covariance matrix. However,

the improvement in vertex resolution is marginal because, in principle, the two methods are identical save for coding errors, rounding errors, and speed. The remainder of this section describes the BTF algorithm in detail.

The BTF principle is shown schematically in Figure 6.2. Each of the
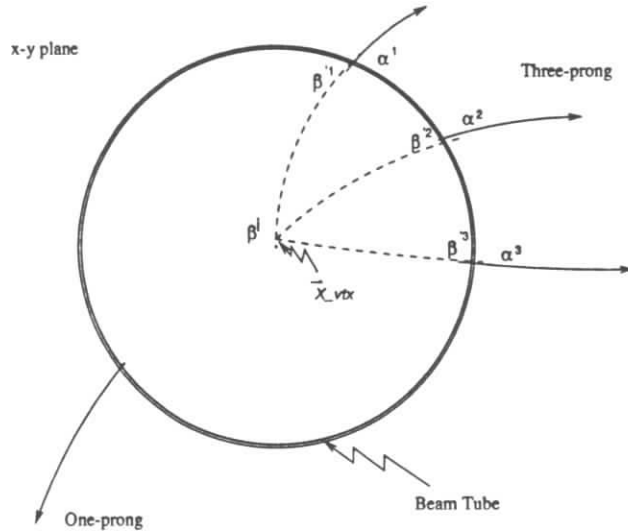
Figure 6.2: Schematic of beam tube vertex fit. The solid lines represent VDC tracks swum to just inside the beam tube. The dashed lines represent the best estimate of the track parameters, assuming the tracks originate from a common point. See text for further details.

three-prong VDC tracks is swum to a radius just inside the beam tube, and the track parameter sets α^i ($i = 1, 3$) and covariance matrices V^i stored. They provide constraints on the unknown values of the true track parameters and vertex position in the beam tube, and are considered constant matrices in what follows. Another constraint is introduced by the assumption that the three tracks originate from a common vertex $\vec{X}_{vtx} = (x, y, z)$. Accordingly, each track i is described mathematically as emanating from $\vec{X}_{vtx}$ with track parameters $\beta^i = (0, 0, \kappa^i, \cot\theta^i, \phi^i)$. (Here, d_o and z_o are zero by virtue of

choosing the track reference point to be $\vec{X}_{vtx}$.) The objective is to determine the vertex position, $\vec{X}_{vtx}$, and the three *vertex track* parameter vectors, β^i, that best match the VDC tracks at the beam tube, α^i. To make the comparison, the vertex tracks need to be extrapolated to the beam tube (see below). Then a χ^2 function can be constructed to quantify the match:

$$\chi^2 = \sum_{i=1}^{3} \left[(\beta'^i - \alpha^i)^T V^i (\beta'^i - \alpha^i) \right], \qquad (6.37)$$

where $\beta'^i = \beta'^i(\beta^i, \vec{X}_{vtx})$ are the vertex track parameters extrapolated to the beam tube. The values of β^i and $\vec{X}_{vtx}$ that minimise expression 6.37 provide the best estimate of the vertex track parameters and position.

The assumption of a constant, longitudinally-directed magnetic field greatly facilitates the determination of β'^i: the basic track step formulas, Equations 6.7 and 6.9, immediately yield analytic expressions for the vertex track parameters at the beam tube, as a function of β^i and $\vec{X}_{vtx}$. This eliminates the need to perform a more cumbersome, and potentially inaccurate, multi-step swimming procedure. Another advantage of the BTF approach is that the covariance matrices of the VDC tracks need to be calculated just once (at the beam tube), and are accurate *regardless of where the vertex lies in the beam tube*.

The minimisation of 6.37 is carried out by linearisation and iteration, in a manner identical to the ARGUS track fit.

Chapter 7

Calibration and Alignment

The technique employed to extract a tau lifetime measurement from ARGUS data relies heavily on the tracking abilities of the ARGUS main drift chamber and vertex detector. It is essential that these devices be calibrated properly for optimal precision and accuracy.

7.1 Calibration of the ARGUS Drift Chamber

7.1.1 Purpose of Calibration

As a charged track traverses a DC cell it ionises the chamber gas. These electrons (ions) immediately begin to drift towards the sense (field) wire under the influence of the electric field. Charge multiplication occurs as the first electrons arrive near the sense wire (typically within a few radii of it) and are accelerated by the increased electric field to energies large enough to spawn further ionisation. This sudden increase in free charge (avalanche) is detected with an electronic circuit connected to the wire and used to trigger the start of a TDC. This is later stopped at a predefined time after the bunch crossing. The farther a track passes from a sense wire the longer the time required for the electrons to drift and trigger the TDC. Therefore the TDC value provides an indirect measurement of the distance of closest approach of the track to the sense wire. It is the role of the calibration procedure to determine the actual relationship between the drift distance and drift time

(distance-time relationship or DTR).

7.1.2 The Calibration Philosophy

For each event, the DC provides a list of the wires hit, along with the corresponding ADC and TDC values. The drift distances are *a priori* unknown but can be determined with a simple bootstrapping method. This is possible because the TDC values in an event are not independent but correlated, the common link being that they are produced by charged particles which have (usually) smooth, continuous trajectories. The basic principle then is to find a DTR which makes all hits in a set of events as consistent as possible with their being produced by charged tracks. An iterative procedure is employed. An approximate initial DTR leads to relatively poor track fits characterised by large deviations between measured distances (derived from the TDC values using the initial DTR) and fitted distances (those resulting from the track fit). The DTR is updated using these deviations and used as input to the next iteration. The procedure converges rapidly because of the staggered cell design of the drift chamber which ensures that in general a track has roughly equal numbers of hit wires on either side of it, thus providing the optimal constraint on the track parameters. In the following section a more detailed description of the DC calibration procedure is provided.

7.1.3 Calibration Procedure

Calibration of the ARGUS drift chamber involves a rather complex chain of steps.

- **Selection of Calibration Data Sample** The best types of events to use for calibration are barrel Bhabhas. They are numerous, easily identified, and, from a pattern recognition point of view, unambiguous. Furthermore, the tracks have high momentum and do not suffer from multiple scattering which complicates the track fit. The high transverse momentum also implies that all cells hit are traversed with near-radial incidence thus permitting a single DTR to be used for all

cells. However, barrel Bhabha events are predominantly t-channel processes and therefore have a $\cos\theta$ distribution strongly peaked towards higher $\cos\theta$ values. In contrast, most physics processes of interest are roughly flat in $\cos\theta$. It is therefore advantageous to calibrate with a flattened Bhabha distribution in order to minimise the adverse effects of any polar anisotropy that may exist in the tracking and calibration procedures. The selection of such a flattened Bhabha data sample is the first step in the calibration procedure. To achieve such a sample events are randomly rejected subject to the condition that the track $\cos\theta$ distribution for the surviving events is flat.

During the iterative process several quality cuts are made before allowing a track to contribute to the DTR and resolution function determination. These include cuts on the track fit probability ($> 1\%$), number of hits ($\geq 12axial, \geq 12stereo$), transverse momentum($> 2GeV/c$), extrapolated distance of closest approach to the origin in $x - y$ (1cm) and z (5cm), and assigned number of multiple scattering kinks (< 1).

- **TDC timing corrections** To make the best use of the raw TDC values several timing corrections need to be applied. Two types of TDC corrections can be distinguished: those affecting the start time of the TDCs and those affecting the stop time. The following affect the stop time and are applied prior to pattern recognition on an event-by-event basis.

  - determination of crate shifts The DC TDCs occupy nine crates, each with its own controller. Although timing differences among the TDCs within a given crate can be kept to a minimum (using the Autotrim feature of the TDCs together with test pulses), there can be strong timing differences between crates due to the manner in which they process their signals. The stop signal may also arrive at the crates at slightly different times. To account for these offsets 9 crate time shifts are determined from the position of the leading edge of the TDC spectrum of each crate and used to correct the

TDC values. The spectra are obtained from the events in the calibration sample. An example is provided in Figure 7.1. The
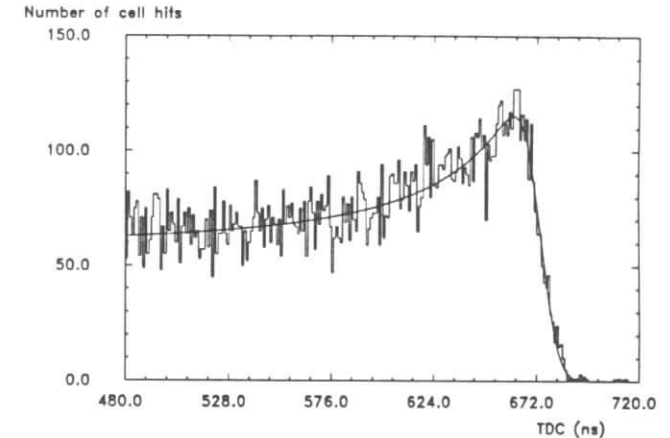
Figure 7.1: Trigger time corrected TDC values for all TDCs from one crate for a sample of calibration Bhabhas. Overlaid is the result of an empirical fit used to determine the crate shift.

shift in time between crates is typically 5-10ns but can be as much as 30ns.

- correction for bunch crossing and trigger jitter As mentioned earlier the TDCs in the DC are operated in common stop mode which means that all TDCs started by an event are stopped at the same delayed time after the bunch crossing, which is known very precisely. The actual stop signal is a delayed coincidence of this bunch crossing signal and the ARGUS trigger signal, and the various possible trigger types lead to different stop times. The time correction for each trigger combination is taken from a long-term average of stop signals using barrel Bhabhas. The TDC values are updated accordingly.

In contrast to these, the following timing corrections can only be applied once a rough estimate of the track position has been found. They affect the start times of the TDCs. In practice they are applied during the track fit after pattern recognition.

- correction for pulse travel down wire This correction requires the knowledge of the z position of the track along the wire. Once known, the amount of time it takes for the charge deposition signal to travel down the wire and arrive at the endplate where the TDC is mounted can be taken into account. The propagation speed has been found to be of the order of $v_{prop} = 24cm/ns$, hence ignoring this effect can lead to errors in TDC values up to $200cm/v_{prop} = 8ns$.

- correction for time of flight of track Low energy particles can have velocities significantly less than the speed of light and can take several nanoseconds to traverse the DC. Even high energy particles cannot traverse the DC in less than $(80 - 20)cm/c \approx 2ns$. The farther along a track a hit lies the later its TDC is started. Left uncorrected, this makes the track appear farther from the wire than it actually is. During the track fit, the TDC value of each hit is modified using its distance along the track. At the start the velocity β is set to one, and subsequently improved using the drift chamber dE/dx analysis.

Thus corrected, each TDC value is in principle in one-to-one correspondence with a drift distance. It will be referred to from now on as the drift time t. The determination of the distance-time relation (DTR) can then be carried out.

- **Initial DTR and Resolution Function** An initial estimate of the true DTR $d(t)$ can be derived from the drift time spectrum assuming that the drift cells are uniformly irradiated by tracks in a Bhabha

sample. In this case the following approximation can be made

$$\frac{dN}{dt} = \frac{dN}{dd(t)}\frac{dd(t)}{dt} \approx \frac{N}{d^{max}}\frac{dd(t)}{dt}. \tag{7.1}$$

Therefore, integrating the time spectrum $\frac{dN}{dt}$ yields a first estimate for $d(t)$:

$$d(t) \approx \frac{d^{max}}{N}\int_t^{t_{max}}\frac{dN}{dt'}dt'. \tag{7.2}$$

Note that equation 7.1 implies that the time spectrum is essentially a plot of drift velocity vs time. Indeed, Figure 7.1 displays the expected increase in drift velocity as the wire is approached (large times), consistent with the increase in field intensity near the wire.

- **Determination of DTR and resolution functions**

  - Update of DTR

    Using this first approximation for the DTR the Bhabha calibration dataset is reconstructed. At this initial iteration stage each hit assigned to a track assumes the same weight in the track fit, i.e. a constant resolution function is used (a typical starting value is 250 microns). For each time value, the difference between the unsigned fitted and measured drift distances (distance correction),

    $$\Delta d(t) = |d_{fit}| - d(t),$$

    averaged over all track hits and all events, is calculated and used to improve $d(t)$ for the next iteration:

    $$d'(t) = d(t) + \overline{\Delta d(t)} \tag{7.3}$$

    Care must be taken in extracting the form of $d(t)$ near the wire due to ionisation statistics. This can be immediately understood by considering tracks that pass through the wire, i.e. at zero drift distance. (For the purpose of this argument assume the wire has infinitesimally small radius.) Imagining for the moment that the track ionises the chamber gas continuously, there would always be

an ionisation right at the wire. This would immediately avalanche and produce a signal. The time for drift would be negligible. In reality, however, the gas is not ionised continuously, but with a well defined average of n_p primary ionisations (as opposed to secondary ionisations resulting from the collisions of these primary particles with the gas) per centimetre. For Bhabhas in propane, this number is about $n_p = 38/cm$, implying that on average an ionisation takes place about every 260 microns. The average time for the charge to drift will therefore be greater than zero despite the mean fitted distance being zero. This implies that the mean distance correction is always greater than zero near the wire and accordingly that $d(t)$ can never satisfy $d(t) = 0$, a somewhat undesirable condition. The solution is to do the inverse and calculate the average *drift time* near the wire as a function of fitted distance and invert the resulting function. At a distance far enough from the wire (.3cm is used) the two functions match and are smoothed with a cubic spline to yield the new DTR. The entire procedure is then repeated using the new DTR until it ceases to change.

– Update of Resolution Function At this stage, a plot of the r.m.s. values of the residuals as a function of drift time indicates that the cell has variable resolution. At very large distances field distortions become important, and the isochrones deviate strongly from circles. At distances close to the wire, ionisation statistics lead to a large jitter in the TDC start. To get the most out of the track fit it makes sense to incorporate these r.m.s. values as drift distance weights. Caution is needed in this endeavour, however. The fitted track, not the true track, is used to determine the residuals and because the fitted track is the one that minimises the residuals the true resolution is underestimated by the r.m.s. values. To correct for this the residuals are individually scaled by a factor derived from the track fit covariance matrix, and the r.m.s. values of these scaled residuals, after being smoothed with a cubic spline fit, are

used. Further iterations of the calibration procedure update both the DTR and the resolution function. Examples of the final forms of these functions are shown in Figure 7.2.

• **Layer Time Corrections** Despite the timing corrections applied to the raw TDC values, small timing variations from cell to cell are still observed. These are parametrised on a layer by layer basis using the average distance correction observed in each layer, and used to update t accordingly:

$$\Delta t_{layer} = \frac{\overline{d(t)}_{layer}}{v_{drift}}, \tag{7.4}$$

where v_{drift} is calculated directly from the DTR. Only distance corrections from the best timing region are included in the calculation, i.e. the region with well defined DTR and good spatial resolution. These 36 timing shifts are determined and applied during the calibration iteration procedure. Convergence is rapid and stable.

• **Threshold Corrections**

The calibration procedure as described so far was improved significantly through a careful study of the effect of ionisation density on the TDC rise times. The exact time a given TDC stops is governed by a voltage threshold V_{thresh} which the signal voltage due to a hit must meet in order to trigger the TDC stop. The threshold voltage needs to be set reasonably high to avoid background noise from electronics. Because the shape of the signal voltage as a function of time can differ depending upon the form and amount of ionisation deposited in a cell, the exact time V_{thresh} is satisfied is signal dependent. For example, a large deposition of charge in a cell produces a signal which rises quickly to trigger the TDC stop, whereas smaller depositions lead to signals which rise more slowly in time and trigger the TDC stop later. This phenomenon not only affects the DTR but the resolution function as well because smaller signals suffer from a larger threshold crossing jitter.

Although the calibration procedure as it has been described so far takes the above effect into account in an average way, a considerable improve-

d(t) [cm]
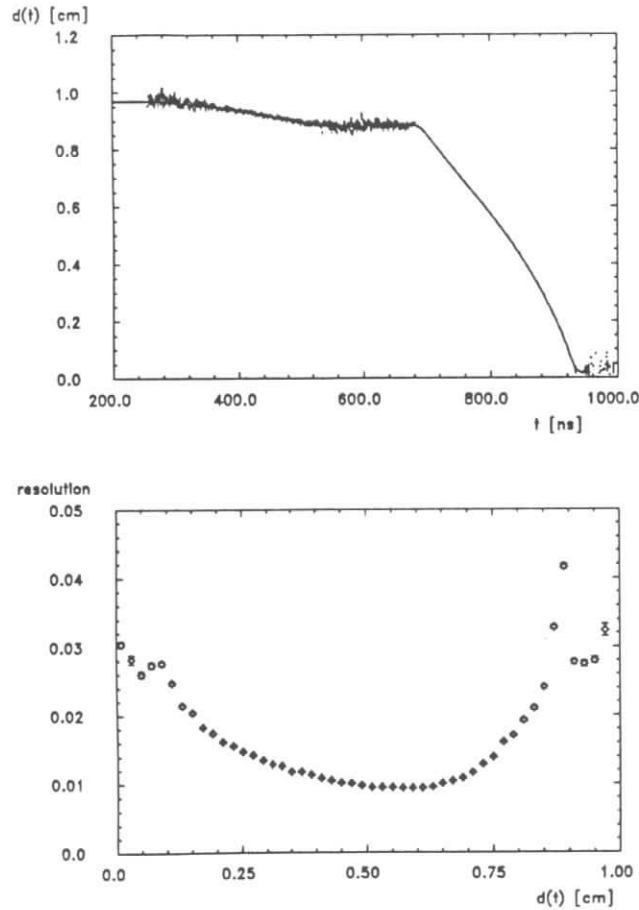
Figure 7.2: Example distance-time and resolution functions resulting from the drift chamber calibration procedure for a particular calibration period.

ment is gained when two sources of signal deposition variation, namely the polar angle θ and the mean energy loss of a track, are taken into account. For a given rate of track energy loss and distance of closest approach to a wire, the ionisation density (ionisations per unit length travelled) in the plane perpendicular to the wire increases for smaller angles of incidence with respect to the wire (Figure 7.3). Similarly,
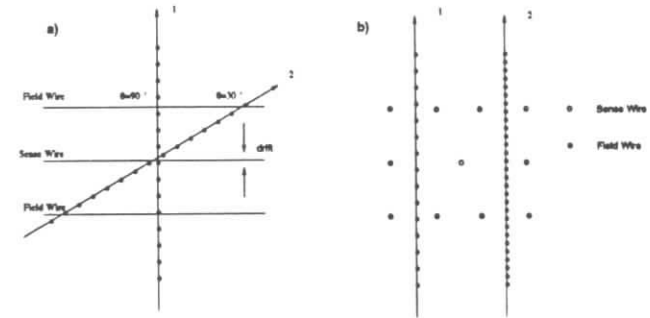
Figure 7.3: Schematic view of $\sin \theta$ threshold dependence for a drift drift chamber cell. Two views of the cell are shown: a) in profile (r-z), and b) in cross section (x-y). The track traversing with smaller θ has a higher ionisation density in the plane perpendicular to the wire.

the ionisation density is higher for tracks suffering a larger energy loss. Therefore, in the absence of saturation the rate of voltage rise has the following expected dependence on energy loss and $\sin \theta$:

$$\frac{dV}{dt} \propto \frac{dE/dx}{\sin \theta}. \tag{7.5}$$

If one in addition assumes the time dependence is linear, an expression for the timing correction follows immediately. In reality the time dependence of the pulse is not linear, nor is the effect of saturation absent. Therefore, the actual corrections are extracted directly from the experimental data using the average distance correction as functions of $\sin \theta$ and energy loss. A quadratic fit to the mean threshold time correction Δt_{thr} vs $\sin \theta$ is used to parametrise the timing dependence

on polar angle, where

$$\Delta t_{thr} = \frac{\overline{d(t)}}{v_{drift}}. \tag{7.6}$$

Similarly, the mean resolution versus $\sin \theta$ suggests the form of correction to the resolution function, likewise parametrised with quadratic time dependence. The dependence on energy loss is similarly taken into account. In practice these threshold corrections are determined once after the calibration procedure described above has converged, and there is no attempt to improve the parametrisations through iteration.

It should be mentioned that the DTR and $\sigma(t)$ dependence on θ is the primary motivation for using a flattened Bhabha sample for calibration. In an earlier version of the calibration procedure unflattened samples of Bhabhas were used and no θ correction applied. Thus the DC calibration systematically produced a resolution function which was too good, leading to large discrepancies between the observed resolution of the chamber and that predicted by the calibration. For a further discussion on this see Section 8.7.

7.2 Calibration of the ARGUS Vertex Chamber

The calibration of the ARGUS vertex chamber proceeds in much the same manner as that of the drift chamber. However, there are significant differences:

- only one TDC crate collects the drift time signals, therefore there are no individual crate shift constants to calculate,

- the TDC values are kept "zeroed" by feeding test signals to the preamps on a daily basis, eliminating the need for corrections equivalent to the DC layer constants,

- the chamber is operated near saturation therefore no dE/dx correction is required, and

- the chamber has only axial wires.

Despite these seeming simplifications, the chamber is more difficult to calibrate for the following reasons:

- The chamber is a physically separate entity from the DC and its exact position and orientation in space with respect to the DC (which defines the global coordinate system) is *a priori* unknown and must be determined. (See alignment section below.)

- Fewer hits on average are associated with each track, therefore the boot-strapping calibration mechanism is not as powerful and converges slowly. This also implies that the scale factors for the residuals in the resolution function determination are large compared with unity and hence less reliable.

- Although the VDC calibration is carried out as independently of the DC as possible, the chamber does not provide a large enough lever arm for a good curvature measurement, κ. This parameter and the longitudinal track parameters z and $\cot \theta$ (to which an all-axial wire chamber is in principle insensitive) need to be taken from the DC. Therefore, the chambers are not completely decoupled in the calibration process, which thus becomes vulnerable to any systematic effects originating in the DC.

- Because the hexagonal cell structure has a translational symmetry not a rotational symmetry as in the DC, cells are not all irradiated with the same orientation by Bhabha tracks. There is a six-fold ϕ-dependence in the angle of attack which translates into a six-fold ϕ-dependence in the DTR and resolution function due to the non-circular isochrones of the cells.

- A very aggravating aspect of the VDC is the cell configuration along the rays at $(30 + 60n)$ degrees for $n = 0$ to 5. (Figure 5.3). Tracks having ϕ values in these regions have an overwhelming imbalance in

the number of left and right hits and are poorly constrained, compromising the self-calibrating method. Excluding this region and placing the burden of calibration on the rest of the chamber is not a legitimate approach because the DTR is ϕ-dependent and can only be properly and completely determined using all attack angles.

- Sizeable tails in the distribution of residuals play havoc with the resolution function. These tails are much larger than their DC counterparts and arise from several sources. For example, the isochrone curvature is much larger because of the small size of the drift cells, making the jitter in the signal rise time more susceptible to ionisation statistics across a greater proportion of the cell. Also, there is a significant background hit population in the VDC due to synchrotron radiation and electronics noise, which leads to bad hit assignments. In the first iterations of the calibration procedure, when the resolution has a large and constant value (250 microns at start), the pattern recognition window is wide open and vulnerable to this background. Furthermore, the field in the outer region of the cell diverges severely from radial (see Figure 5.4) and the DTR is ill-defined, leading to a wide spectrum of drift distances associated with a given TDC.

- The chamber has a better intrinsic resolution than the DC and is therefore more sensitive to small systematic perturbations.

In light of these points it is not surprising that the track fit probability distribution for a sample of calibration Bhabhas is not flat but typically looks as it does in Figure 7.4.

The procedure for calibrating the VDC involves the following features.

- **Selection of calibration data sample** The VDC is calibrated with the same flattened Bhabha data sets used to calibrate the DC. However, these data sets are first reprocessed using the improved DC calibration just described. DC and VDC track quality cuts are applied.

- **TDC timing corrections** Trigger jitter corrections as well as corrections for pulse travel time down the wires are applied to the TDC
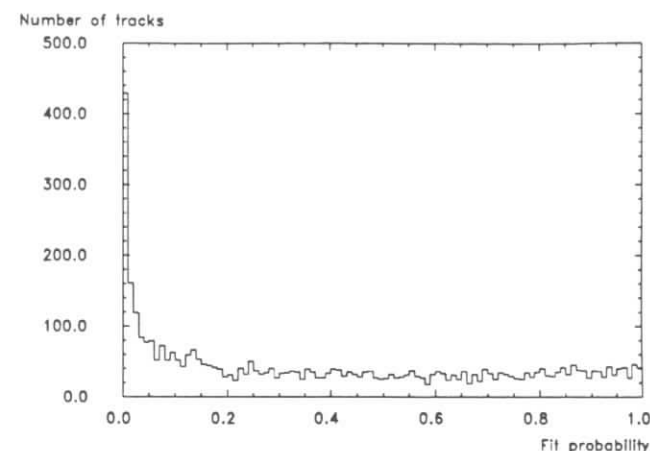
Figure 7.4: VDC track probability distribution for a sample of calibration Bhabha events.

values.

- $\sin\theta$ **correction** Despite the fact that the VDC is operated near saturation there is nevertheless a $\sin\theta$ dependence similar to that observed for the DC, albeit much smaller. A correction is applied, although the improvement introduced is not as marked as for the DC. No dE/dx correction is applied.

- ϕ**-correction** To account for the cell asymmetry in ϕ a correction to the drift distance is made. The correction is determined from the average residuals observed as a function of ϕ and t. No ϕ-dependent correction to the resolution function is made because attempts to apply such a correction result in extremely erratic and unreliable convergence of the calibration procedure.

7.3   Alignment of the ARGUS Vertex Chamber

In order to define the positions of tracks in space a coordinate system is required. The ARGUS coordinate system is defined as having its origin at the center of the drift chamber with z-axis along the common symmetry axis of the inner and outer walls. The x- and y-axes are fixed through the definition of the ϕ values of the wires in the chamber, the y-axis lying in the vertical direction. Therefore, barring small uncertainties in the wire positions within the design tolerance, the drift chamber is by construction perfectly aligned - the DC local coordinate system is adopted as the ARGUS coordinate system. The VDC however has its own coordinate system through which its wire positions are defined. Because the VDC is a physically separate component from the DC these two coordinate systems do not in general coincide and the relation between the two must be determined in order to properly include VDC hits in the track fit. This section briefly describes the alignment procedure used to determine the position and orientation of the VDC with respect to the ARGUS coordinate system.

To define the orientation and position of a body in space 6 parameters are required: three for the position of some reference point in the body, and three to define how the local coordinate system of the body is rotated with respect to the global coordinate system. Since the VDC is insensitive to translations along the wire direction only two coordinates are needed to specify the position of the chamber, and these are taken to be the displacement Δx and Δy of the geometrical centre of the VDC with respect to the ARGUS coordinate system. The orientation is then specified by the rotations about each of the coordinate axes which are required to bring the ARGUS frame into coincidence with the VDC frame.

For an extremely misaligned chamber, tracks swum from the DC into the VDC would fail to be associated with the correct VDC hits, if any, because the positions of these hits in the ARGUS coordinate system would be wrongly specified. A slightly misaligned chamber would find these hits but the mean track fit probability would be poor. The procedure is therefore fairly sim-

ple. Beginning with an initial approximate set of alignment parameters $\vec{b}$, a sample of $ntrk$ Bhabha tracks is reconstructed using DC and VDC track hit information. Using the dependence of the mean track fit probability (or more directly the sum of track fit χ^2 values) on the alignment parameters, a new set of parameters can be computed and used as input to a second iteration. Mathematically, one minimises the expression

$$\chi^2_{tot} = \sum_i^{ntrk} \chi^2_i = \sum_i^{ntrk} \sum_j^{nhit_i} \left(\frac{d_j(\vec{b})}{\sigma_j} \right)^2$$

in a manner similar to that outlined in Chapter 6 for the track fit. The procedure is repeated until convergence, which for a "cold start" and 3000 Bhabhas is well within ten iterations. It is not necessary to use Bhabhas, although they are normally used for alignment at ARGUS. For the current analysis four-prong data were employed instead.

The VDC was first installed fully instrumented in 1985. It was removed for servicing after the 1985 run and then replaced in the interaction region where it remained until it was superceded by the μ VDC in 1989. In principle, therefore, only two sets of alignment parameters are required. However, as will be discussed further in Section 8.8, owing to problems with fluctuating wire positions in the main drift chamber, it was necessary to realign the VDC more often. This also compensates for a possible movement in the VDC mounts due to temperature changes or mechanical stress.

7.4   Determination of the DC Wire Positions

A plot of the normalised d_o track parameter sum

$$\delta = \frac{d_o^+ + d_o^-}{\sqrt{\sigma_+^2 + \sigma_-^2}}$$

for DC di-muon tracks (VDC information ignored) swum to the beamline indicates a rather disturbing bias in the tracking (see top plot of Figure 7.5). The negative shift in the mean of the distribution implies that, on average, the muon tracks, which originate from a common point, are not reconstructed

to meet at the beam line but systematically miss each other. This unphysical phenomenon is also displayed in lower momentum tracks and has the potential to seriously bias a lifetime measurement. Although offsets like this are common among the various HEP experiments, the magnitude of the shift at ARGUS, some 60-80 microns, is unacceptably large for a legitimate lifetime measurement using vertex impact parameters of the order of 100 microns. An event-by-event correction of this order of magnitude cannot be justified without compromising the accuracy of the result, and a correction for this offset was devised.

The track offset was originally discovered with VDC tracks and quickly traced to the DC. A long and agonising process of searching for the source of the offset then began. No offset exists in Monte Carlo data therefore the track reconstruction algorithm was not a candidate. A new state-of-the-art calibration of the drift chamber (that described in detail above) had no effect. (This might have been predicted *a priori* because no aspect of the calibration or TDC to drift distance conversion has the potential to introduce any significant left-right (azimuthal) shift in the track positions in space, essentially a consequence of equal numbers of hits constraining a track on each side.) If the ϕ symmetry of the detector and magnetic field is accepted, neither an incorrect energy loss application nor a faulty field mapping can account for this offset because any problems in these areas would manifest themselves in the same way for both tracks. This would lead to a common shift at the beamline, and not manifest an offset.

The simplest conclusion is that the differences between the true and designed wire positions are badly correlated and combine to produce the observed shift rather than averaging out to contribute simply to an overall degradation of the resolution. The tolerances for wire positions are about 100 microns, making it entirely plausible that this is a source of the offset. In fact, when the endplate holes were being drilled it was noticed that the procedure had the potential to introduce systematic offsets and it was interrupted and modified. Perhaps the final procedure was not the optimal one. Any misalignment of the two endplates with respect to each other would also cause a discrepancy between the coded and true positions. Another possible
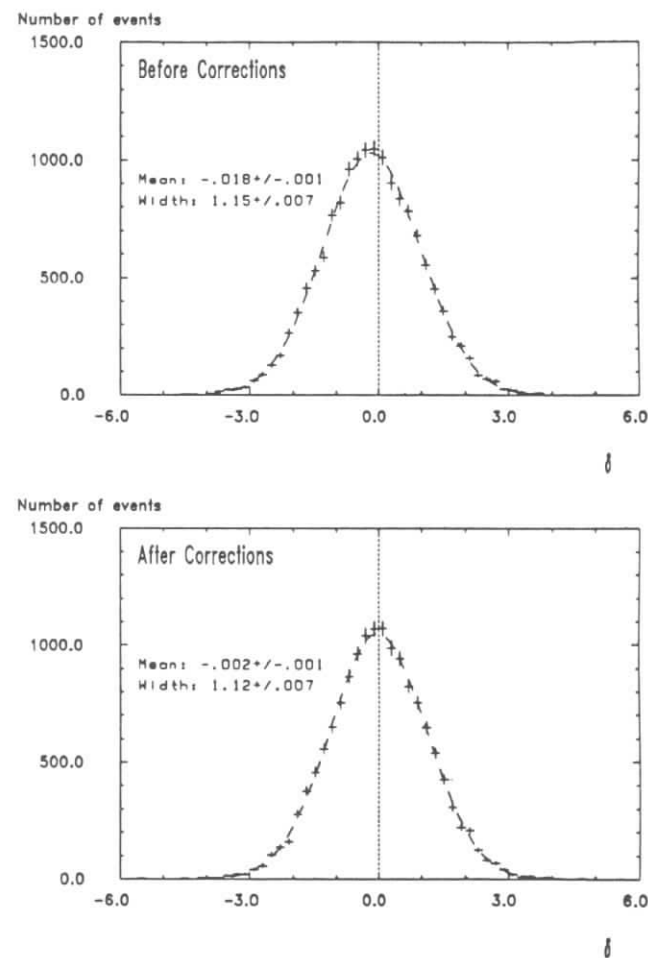
Figure 7.5: Distribution of normalised missed distances for a sample of dimuon events using a) uncorrected wire positions and b) corrected wire positions. The non-zero mean reflects tracking inconsistencies traceable to the DC wire positions. VDC information has been ignored.

explanation can be found in the manner in which the DC wires were strung (Figure 7.6). A weight under the force of gravity was used to achieve the
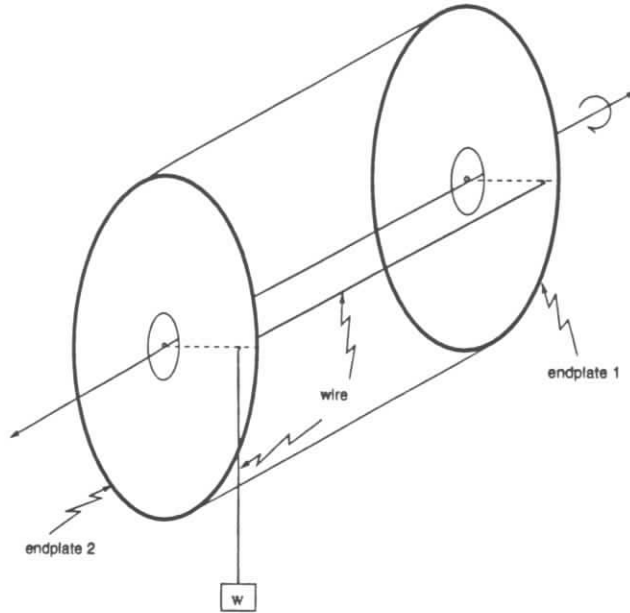
Figure 7.6: Schematic indicating the orientation of the DC during wire stringing.

correct wire tension before crimping. The chamber was then rotated in azimuth before repeating the procedure. Thus the wires have the potential to be systematically shifted in the azimuthal direction towards the edge of their holes. As this is a common shift in *distance* and not angle, the effect would be to have each layer displaced in ϕ by a different amount, and this would produce the observed track offset at the origin [55]. A further possibility is that electro-static effects take advantage of the slack in the wires due to sag (about 95 microns) and shift the wires around to bring the chamber field configuration to a lower energy state. No correction for such an effect, which

is in principle calculable, is performed in the tracking code. Given that the plastic feedthroughs for the wires have an inner diameter of 120 microns and the sense wires are only 30 microns in diameter, the manner in which the wires are crimped at the end plates also has the potential to introduce correlated wire shifts. In addition stereo wires would have the tendency to push up against the inner wall of the feedthroughs. (This would only have the effect of reducing the stereo angle slightly, however, leaving the position of the wire at the centre of the chamber undisturbed.)

The true wire positions were estimated using a method developed by the author, dubbed ORIFIT (for ORIgin FIT). The method builds on an approach outlined in [56] for determining the wire positions of the new DC that replaced the one with which the data for this thesis were collected. In that approach the Bhabha track momentum is constrained to the beam energy by varying the track parameters within their errors. The updated track parameters are then used to retrace the track in the DC, recalculating the residuals for each hit. Non-zero average residuals suggest a discrepancy between true and coded wire positions and these are updated accordingly.

This approach cured a ϕ-dependence observed in the reconstructed momentum of di-muon events in the new drift chamber. No offset at the origin is observed for those data. When applied to the old drift chamber data, however, this method fails to correct the offset at the origin. This is understandable considering the constraint that the tracks meet at the beam line is not implicitly employed. An extension of the method was devised to correct this weakness. The procedure is sketched in Figure 7.7. In place of Bhabhas, di-muon events are employed, because they are relatively free of radiative corrections and detector interactions. All five track parameters at the beam line are required to be consistent with the muons being produced back to back from a common point and with the same energy. This is achieved by adjusting the tracks within the constraints of their covariance matrices. Details of the fit procedure can be found in Appendix B. Armed with this new estimate of the true di-muon production point and momentum, the tracks are then swum back into the DC and an updated residual for each hit calculated. (No new hits were assigned to the track during this swim, and none

STEP 1:

Swim tracks to beam line
and compute track parameters
and covariance matrix for
each track there

STEP 2:

Calculate best common
set of updated track parameters
using old track parameters
and covariance matrices

STEP 3:

Swim tracks back into DC
using updated parameters
and calculate new residual
for each hit
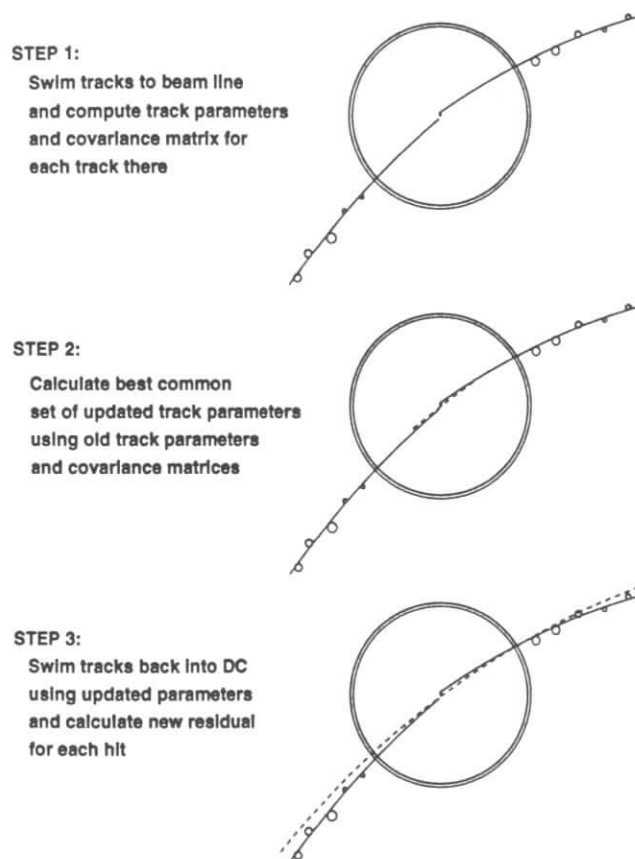
Figure 7.7: The steps taken in the iteration procedure for the determination of the wire positions. The double circle represents the inner DC wall. The VDC and beam tube are not shown. Dimensions are not to scale and the track displacements are exaggerated for clarity.

were thrown out.) The average new residual for each wire is then an indication of the wire offset from its coded position. (Recall that the track residual is a measure of how far to the left or right of the measured drift distance the fitted distance is. If the residuals for a cell are consistently of one sign, this implies that the reference point for the measured distances, i.e. the wire position, is in fact displaced from where it is believed to be.) These updated residuals are used to correct the wire positions (see below) and the entire process is repeated with this new set of positions. The procedure converges rapidly and only a few iterations are required.

Because di-muons at ARGUS are nearly straight this method only indicates how the wires are shifted in ϕ and is insensitive to any shift that might exist in the radial direction. Given that there are 5960 wires in the drift chamber, a considerable number of di-muons are required to resolve each wire shift. A sample of fifteen thousand events was found to be adequate. Shown in Figure 7.8 is the distribution of the mean updated residuals as a function of the wire angle ϕ_W for one of the axial layers in the drift chamber. The sinusoidal nature of the distribution is quite representative of the other layers as well. The top plot shows the updated residuals for the first iteration, i.e. the one in which the designed wire positions were used. The sinusoidal form can be "explained" in terms of an overall shift in x and y and a rotation in ϕ of the entire layer, although this is an empirical description and it is not clear why this should be so. Nevertheless, a parametrisation in terms of such shifts was made of the mean updated residual distribution, each layer assigned its own set of shifts $(\Delta x, \Delta y, \Delta \phi_W)$. Figure 7.9 shows how these offsets are defined. Due to these shifts a wire with position $\vec{W}$ having radius r and angle ϕ_W assumes a new position in the $x - y$ plane given by

$$\vec{W}' = (r\cos(\phi_W + \Delta\phi_W) + \Delta x, r\sin(\phi_W + \Delta\phi_W) + \Delta y).$$

Using Equation 6.29 for the distance of closest approach of a track to a wire in the $x - y$ plane, it follows that the residual of an axial wire in a layer at radius r is changed by (for a stereo layer the same calculation applies after correcting the residuals for the small stereo angle)

$$\delta = \epsilon' - \epsilon$$
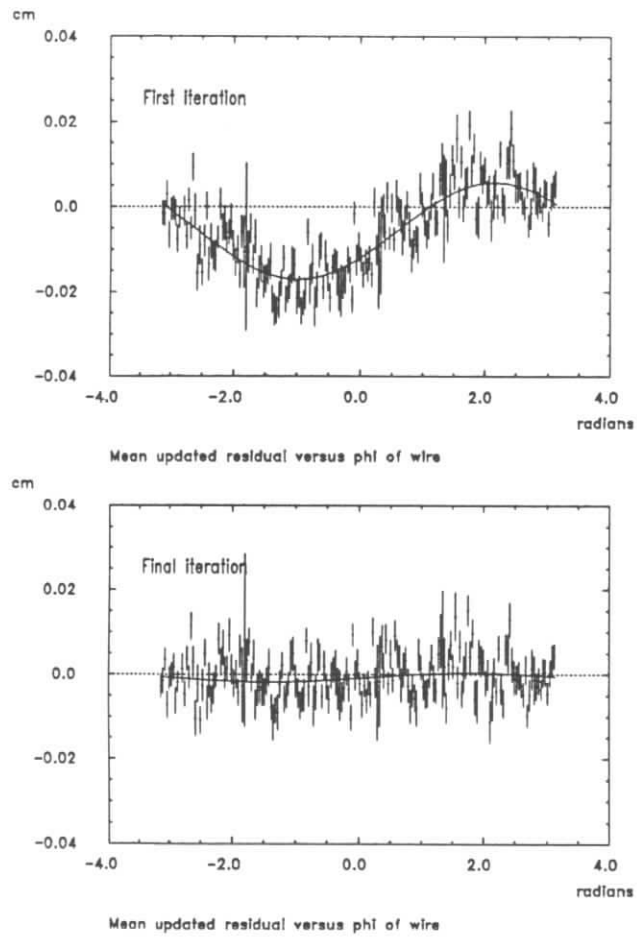
Figure 7.8: The mean updated residual as a function ϕ_W for each of the wires in an axial layer of the DC. The plots show the distributions before and after the wire correction procedure.
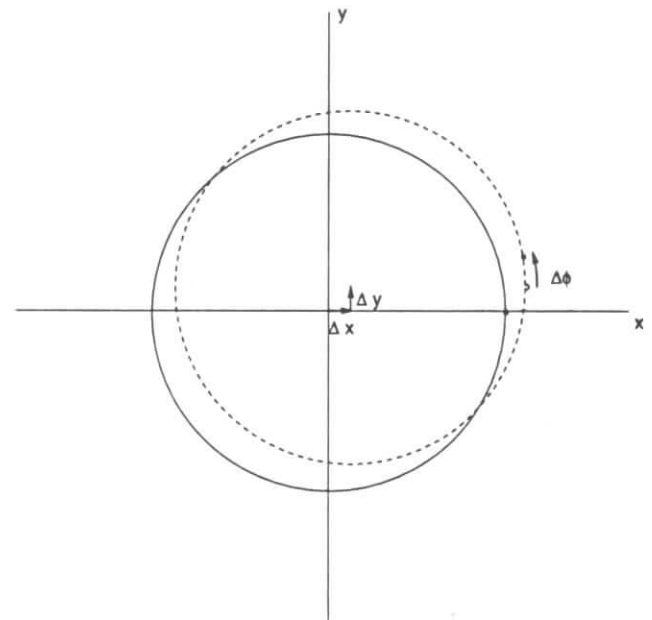
Figure 7.9: Definition of Δx, Δy, and $\Delta\phi_W$.

$$= d' - d$$
$$= (\vec{W} - \vec{W}') \cdot \vec{a}$$
$$= [r\cos\phi_W - r\cos(\phi_W + \Delta\phi_W) - \Delta x] \cdot a_x$$
$$\qquad + [r\sin\phi_W - r\sin(\phi_W + \Delta\phi_W) - \Delta y] \cdot a_y$$
$$\approx [r\sin\phi_W \sin\Delta\phi_W - \Delta x] \cdot (-\sin\phi_W)$$
$$\qquad + [-r\cos\phi_W \sin\Delta\phi_W - \Delta y] \cdot (\cos\phi_W)$$
$$= r\sin\Delta\phi_W + \Delta x \sin\phi_W - \Delta y \cos\phi_W, \tag{7.7}$$

which has the sinusoidal dependence upon ϕ_W that is observed. Here the approximations that the muon tracks are essentially radial and that $\Delta\phi_W$ is very small have been made. Expression 7.7 is used to fit the updated residual plots for each layer as a function of the wire ϕ_W values. The wire positions are then updated using the layer shifts and rotations resulting from the fit, and used as inputs to the next iteration. Typical values of the layer corrections Δx, Δy, and $\Delta\phi_W$ after the third (and final) iteration are shown graphically in Figures 7.10, 7.11, and 7.12, respectively. The bottom plot in Figure 7.5 shows the normalised missed distance distribution using the new wire positions. There is a clear improvement in the tracking quality. In fact, with the updated positions the resolution of the chamber is improved as much as 4% and there is a slight increase in the mean number of hits per track. Furthermore, the shifts determined using statistically independent samples of di-muons are consistent, strengthening the hypothesis that the wire positions are responsible for the offset in d_{miss}.

To make certain that the ORIFIT algorithm is in fact finding the wires correctly, the procedure was tested on a Monte Carlo dataset of 15 000 di-muon events. In the simulation of this dataset the DC layers were rotated and shifted from their normal values by amounts similar to those found in the data, but reconstructed without these rotations and shifts taken into account. The ORIFIT algorithm was then applied to see if it could bring the layers back into alignment. Within the errors, and barring a common overall offset in the Δx, Δy, and $\Delta\phi_W$ values which is not prevented by the algorithm, the procedure was successful. These global offsets are much
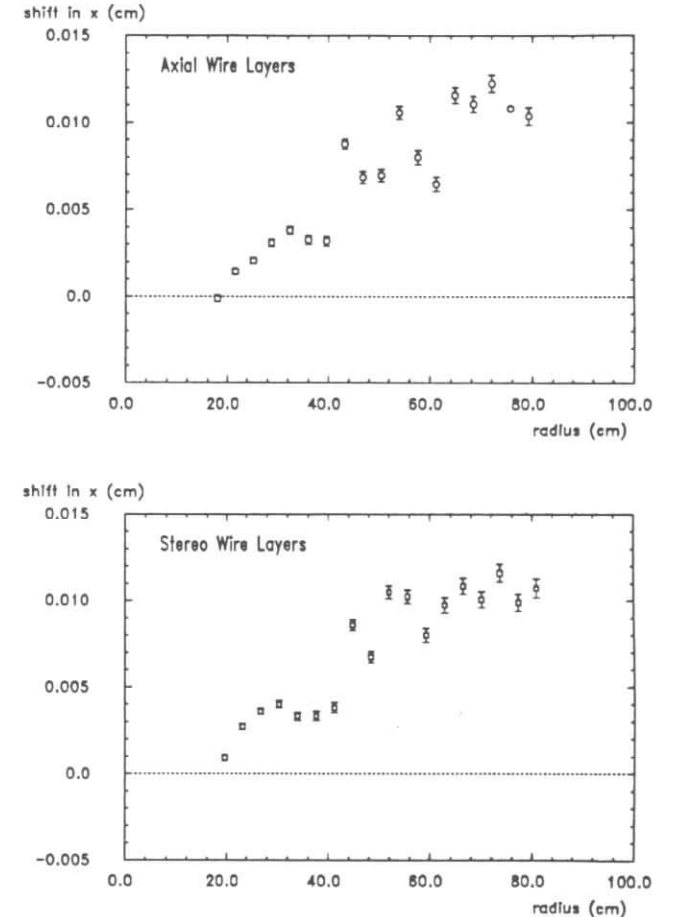
Figure 7.10: Typical values of Δx for each of the layers in the DC.
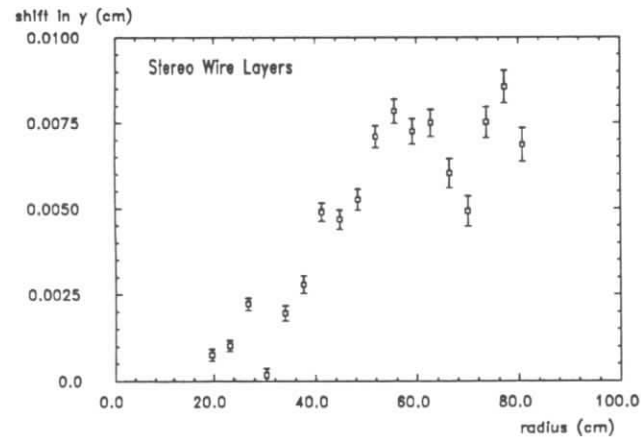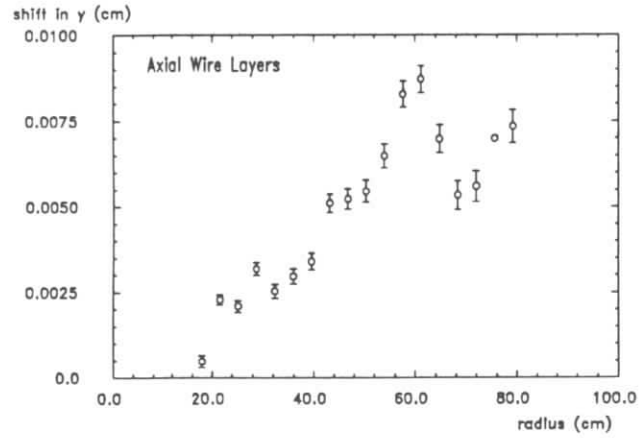
Figure 7.11: Typical values of Δy for each of the layers in the DC.
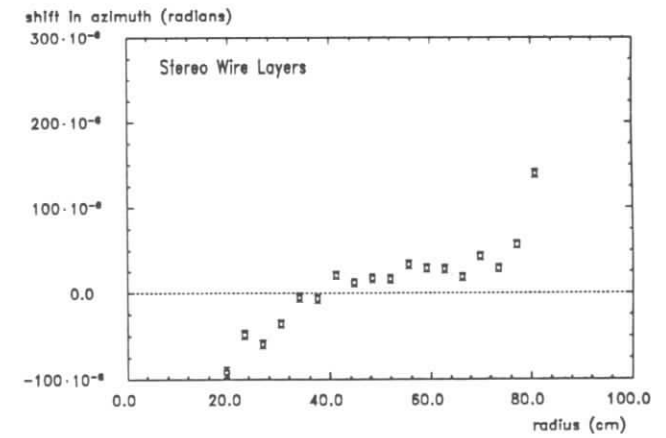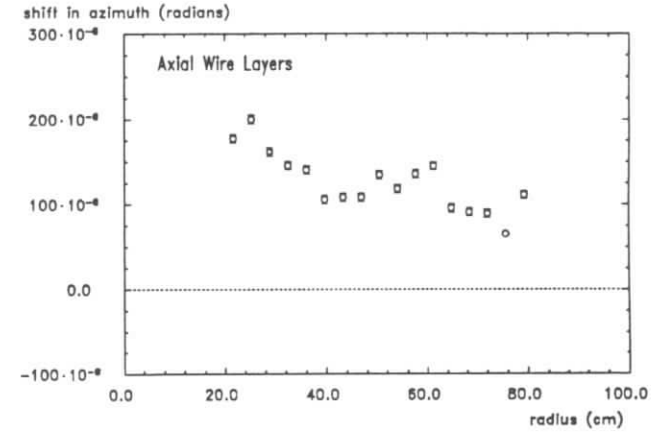
Figure 7.12: Typical values of $\Delta\phi_W$ for each of the layers in the DC.

too small to affect the matching of tracks to hits in the shower counters or TOF counters. They do, however, affect the alignment with the VDC. As discussed above a realignment procedure is, in any case, applied to the VDC using the new wire positions so this effect is compensated for.

Unfortunately, the wire finding procedure is not capable of completely correcting the track offset problem, and adjustments to the track positions at the beam line still need to be made. These residual offsets are particularly evident for reconstructed lower momentum tracks. This is not unexpected because

- the positions of wires were not individually found but rather were found as members of global layer rotations and shifts, an empirical solution which cannot be checked without more knowledge of the actual drift chamber construction procedure;

- using fast tracks, the method is only sensitive to the position of wires in the azimuthal direction, and radial offsets, which come into play for lower momentum tracks, remain;

- it is implicitly assumed that the layer shifts and rotations are valid for all values of z, i.e. only the *mean* deviation in the $r - \phi$ plane is determined and corrected for, and this is definitely not the case (see below); and

- statistically significant variations in the missed distance exist as a function of run within the muon samples used to determine the wire positions, implying a time-dependent DC tracking accuracy which obviously cannot be cured with the constrained fit method.

The last two items are particularly damaging to the method and they are elaborated on further in the next two subsections.

7.4.1 Longitudinal Dependence of Wire Positions

If the wire shifts are in fact due to a faulty drilling procedure then one would expect each endplate to exhibit a different configuration of biased wire positions (or to at best have mirror images of the same configuration). This

would then imply the existence of a z-dependence in the wire offsets. The same holds true if the positions are in fact the result of electrostatic forces. Such a longitudinal dependence is in fact observed. Figure 7.13 shows the distribution of residuals for all wires in one axial and one stereo layer as a function of z for a sample of di-muons. The distributions for the other layers look similar. It appears as though the wires tend to bow in the azimuthal direction, the sign of this direction alternating with layer, i.e stereo layers all bow in one direction and axial layers in the opposite. The form and magnitude of the z-dependence is roughly consistent with the existence of slack in the wire due to sag, but to determine whether electrostatic effects are in fact the cause would require an in-depth calculation of the field configuration. The wire geometry of the chamber is rather complex, however, and there was not enough time to calculate the expected deflections due to the forces on the wires.

Various attempts to correct the wire positions for this z-dependence yielded less than satisfactory results and in the end it was considered wiser to leave the z-dependence of the deviations uncorrected.

7.4.2 Time Dependence of Wire Positions

Another aspect of the wire positions is that they appear to be time dependent. This was first noticed through monitoring the Bhabha missed distance distributions as a function of DC calibration period. Figures 7.14 to 7.16 provide a comparison of the wire layer offsets determined for two of the five data-taking periods used in this analysis. In interpreting these distributions, allowance should be made for a possible common global offset in the Δ values for the two periods. For example, in Figure 7.16, all the open data points (top and bottom plots together), could be shifted downwards by a common value, to bring the comparisons with the filled data points into better agreement. These shifts correspond to an overall translation or rotation of the drift chamber, and are degrees of freedom that are not prohibited by the ORIFIT procedure. Although the trends are similar, there are statistically significant variations. There are a few reasons why this apparent time
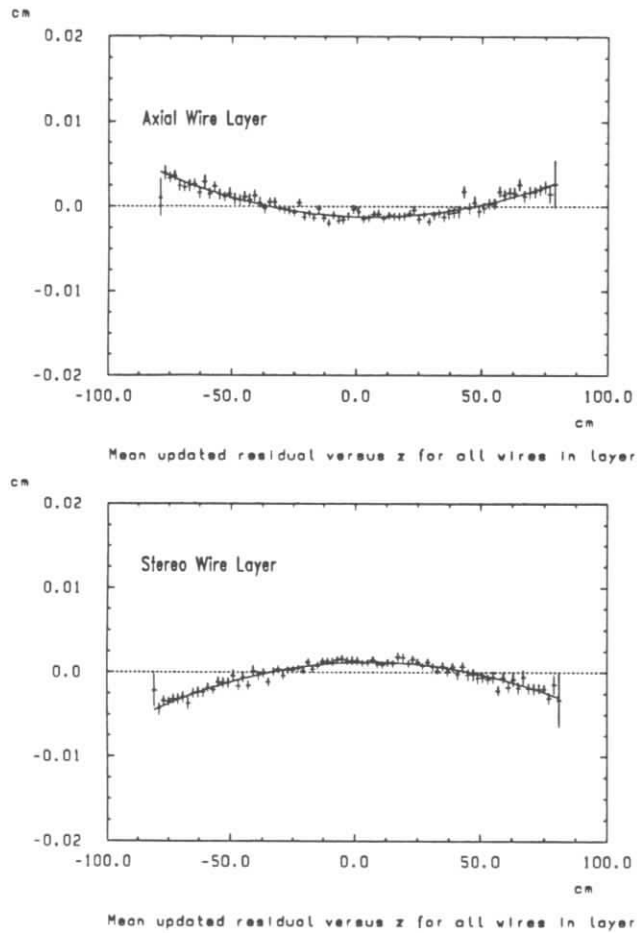
Figure 7.13: Distribution of wire residuals as a function of z for an axial and a stereo layer in the DC. All wires in the layer contribute.
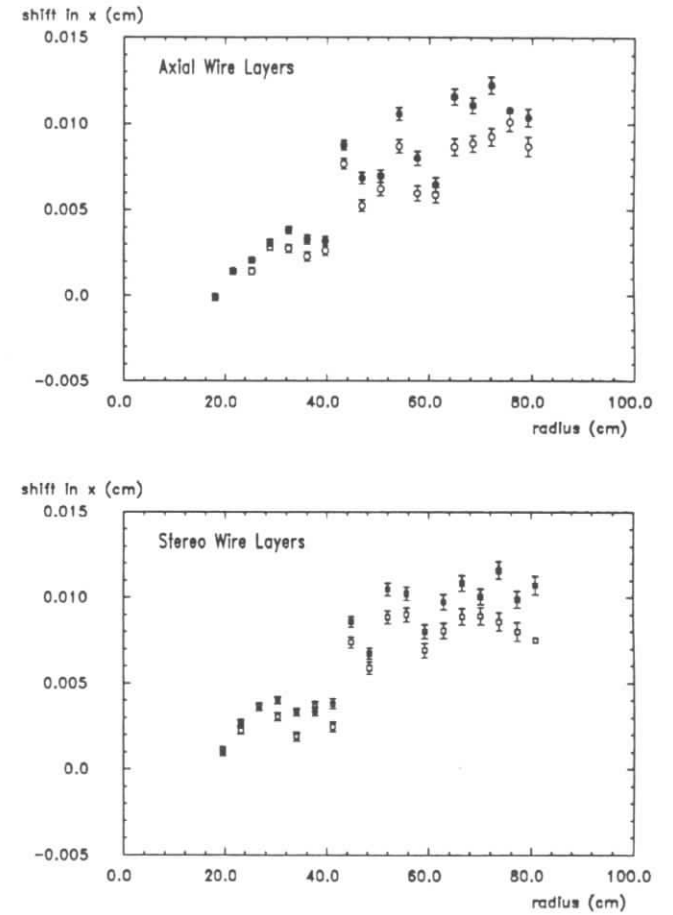
Figure 7.14: Comparison of DC layer Δx values for two different data-taking periods (open and filled data points). See text.
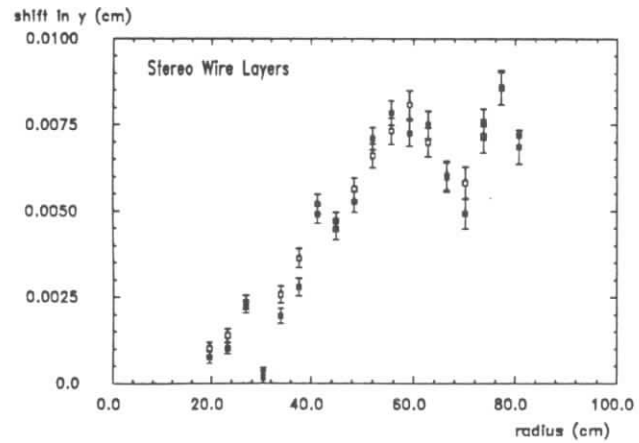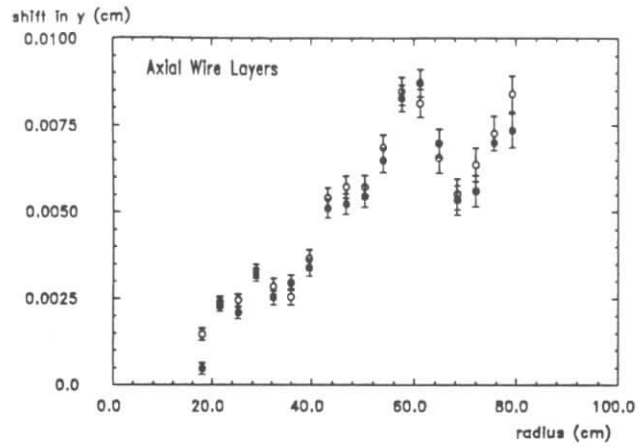
Figure 7.15: Comparison of DC layer Δy values for two different data-taking periods (open and filled data points). See text.
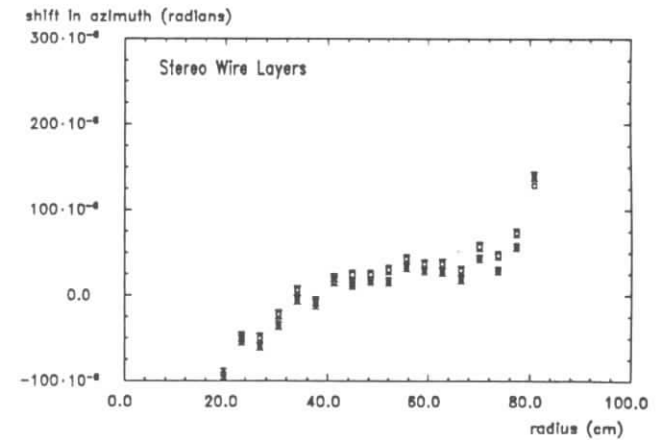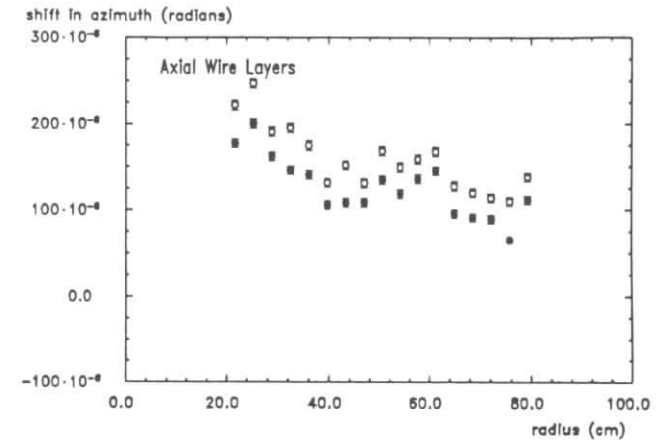
Figure 7.16: Comparison of DC layer $\Delta \phi_W$ values for two different data-taking periods (open and filled data points). See text.

dependence might exist.

- As a result of a long shutdown of over a year and a half in 1987-1988 the epoxy glue used to seal the chamber endplates around the wire feedthroughs lost its elasticity and failed to maintain a proper seal. This made it difficult to keep the gas pressure and composition constant and uniform throughout the fiducial volume. The resulting mechanical stresses would affect the wire positions in a time-dependent manner.

- Despite attempts to keep the temperature of the chamber constant, fluctuations persist. Temperature changes in the aluminium endplates, particularly non-uniform ones, would cause distortions readily transmittable to the wires.

- During some periods of data taking the wire voltages were lowered to try to compensate for high background conditions. This would change the forces on the wires and modify the wire positions.

It is difficult to adjust the wire positions of the DC to correct for these effects. Instead, the gross trends are accounted for by partitioning the data into five groups (limited by the number of di-muons available) and determining a separate set of layer shifts for each. The VDC is also realigned for each of these groups because a change in the DC wire positions throws it out of alignment. This also compensates for any possible movement of the VDC with respect to the DC as a result of temperature changes or mechanical stress. Four-prong data is used for the alignment procedure rather than Bhabhas. After this is done, the remaining track offsets at the beam line are corrected for on an event by event basis. The method used to determine these residual offsets is outlined in Section 8.8.

Chapter 8

Analysis

8.1 Introduction

This chapter describes the application of the *vertex impact parameter* method to ARGUS data.

8.2 Experimental Data

Although ARGUS collected over 500pb^{-1} during its lifetime not all the data were used for this analysis. Only those running periods when the VDC was installed and instrumented were considered. These data were recorded by the ARGUS detector at DESY during 5 separate running periods between 1984 and 1988. The sample comprises data taken on the $\Upsilon(4S)$ and in the nearby continuum. These have centre-of-mass energies in the range $10.43GeV$ to $10.61GeV$, with a mean energy of $10.55GeV$. Runs falling in periods of poor VDC or DC calibration were rejected, as well as runs during which the detector was in a compromised state (e.g. due to hardware failures). The total luminosity for this restricted data sample is 285pb^{-1}, corresponding to about 260 000 produced tau pairs.

The selection cuts applied to these data in order to achieve a reasonably clean sample of tau events for a lifetime measurement are described in detail in Section 8.4.

8.3 Monte Carlo Data

8.3.1 Event Generation

The production and decay of tau pairs were modelled using the KORALB (version 2.2) and TAUOLA (version 2.4) packages [57], respectively. Both initial and final state radiation were included. The branching ratios used for the various tau decay modes follow as closely as possible the PDG96 values given in Table 2.1. The values for the tau mass and tau lifetime were respectively $1.7771GeV/c^2$ and 303fs.

Continuum $q\bar{q}(\gamma)$ events, which form the bulk of the background component of the experimental data sample, were generated using the Jetset version 6.3 package [41].

8.3.2 Detector Simulation

The events generated with the packages described above were fed through the ARGUS detector simulation program SIMARG [58] which uses Monte Carlo methods to model detector efficiencies, acceptances, and resolutions. The program is built upon version 1.3 of the GEANT [59] package which supplies a general framework for modelling geometry and tracking. KORALB and JETSET supply the initial-state direction and energy of each particle in an event and SIMARG models the interactions that take place with the detector along its trajectory. After adjusting for trigger effects (TRIGGR), the output information from SIMARG can be considered equivalent to the output from the actual ARGUS detector. This is then analysed with the same ARGUS reconstruction program that is used for real data (Section 5.12).

For the purposes of this thesis many months were spent debugging and upgrading both the detector simulation program SIMARG and the reconstruction program ARGUS. This is because lifetime measurements at ARGUS are not typical (only two others have been carried out, both in 1986) and more conventional analyses do not tax the performance of the tracking packages at the same level. Bugs that were found and cured primarily involved tracking code. As an indication of the improvement gained, prior

to debugging, Monte Carlo tracks generated at the origin of the detector coordinate system and run through SIMARG would be systematically reconstructed up to 60μ from their production point, depending upon energy and direction. Afterwards, offsets of the order of 0.5μ or less were observed, and this is considered to be the accuracy in the Monte Carlo tracking code (simulation and reconstruction combined). As is discussed in Section 8.8 and Chapter 7 the same cannot be said of real data tracking - although the track reconstruction code is the same for Monte Carlo and data, an inaccurate knowledge of the wire positions in the DC compromises the track position accuracy.

Upgrades (by the author) to the simulation and reconstruction packages include

- a realistic Monte Carlo model, derived from data, of the DC and VDC cell hit efficiency as a function of drift distance,

- an accurate simulation of the hits made in the tracking chambers and their digitisation,

- a new vertex reconstruction procedure which does not rely on repeatedly swimming tracks, and which is therefore less prone to rounding errors,

as well as other more minor improvements.

8.4 Data selection

At the $\Upsilon(4S)$ centre-of-mass energies, Bhabha events, two-photon interactions, beam-gas interactions, $B\overline{B}$ events, and $e^+e^- \to q\bar{q}$ events all potentially contribute to the contamination of a four-prong tau sample. Except for the $e^+e^- \to q\bar{q}$ component each of these backgrounds is reducible to a negligible level through a variety of cuts to be discussed in detail in the following sections.

At ARGUS the continuum component is difficult to reduce to a level below about 4% without a detrimental reduction in statistics. This will

become more clear in what follows. In contrast the superior luminosity (both integrated and specific) of the CESR storage ring makes it possible to apply hard cuts to CLEO data in order to reduce this background to a manageable level. At LEP, efficiencies and purities of the order of (50-80)% and (97-99)%, respectively, are possible for tau decays [60]. The primary reason for this is that the $q\bar{q}$ process undergoes a far greater amount of fragmentation at LEP energies, leading to much higher particle multiplicities and thus making this background easily distinguishable.

8.4.1 Initial Selection

An initial data set was selected from the restricted data pool by requiring exactly four DC charged tracks of total charge zero extrapolated to the beam line within 1.5cm in the $r - \phi$ plane and $6cm$ in the plane perpendicular to the beam line. For the purpose of making these loose tracking cuts, the position of the interaction point was considered to be $x_{beam} = -0.12$cm, $y_{beam} = 0.25$cm, and $z_{beam} = 0.0$cm. (This choice is motivated by a previous determination of the ARGUS beam positions [53], and justified by Figure 8.9.) Each track was required to have a minimum transverse momentum of 0.06GeV/c in order to ensure good track reconstruction and trigger conditions. VDC information was not a consideration at this stage of selection. Extra tracks which did not extrapolate into the required region were ignored at this point and left to be considered at a later selection stage. To capitalise on the heavily boosted decay products of each of the tau particles in the event the following tau topology cut, standard for four-prong tau physics at ARGUS, was also applied:

$$\cos(\vec{p}_1, \vec{p}_i) \quad < \quad 0 \quad (i = 2, 3, 4)$$
$$\cos(\vec{p}_1, \vec{p}_{3pr}) \quad < \quad -0.5$$

where $\vec{p}_1$ denotes the momentum of the one-prong particle and $\vec{p}_{3pr}$ is the sum of momenta of the tracks in the three-prong hemisphere, $\vec{p}_{3pr} = \sum_{i=2}^{4} \vec{p}_i$. This topology also ensures that events have a well defined 1-3 structure. Events in which more than one track could be interpreted as the one-prong candidate were rejected. A total of 104 636 events remain after this pre-selection, with

the acceptance for tau four-prongs at about 14%, or 36 000 events. Therefore a large event background is present and further cuts are required.

8.4.2 Anti-QED Cuts

Radiative Bhabha and di-muon events where a photon undergoes conversion to e^+e^- in the detector can mimic the 1-3 topology of four-prong tau decays because the photon prior to conversion is most likely to be along the direction of the electron or positron. A typical Bhabha candidate is shown in Figure 8.1. However, in contrast to tau decays where both tau neutrinos are
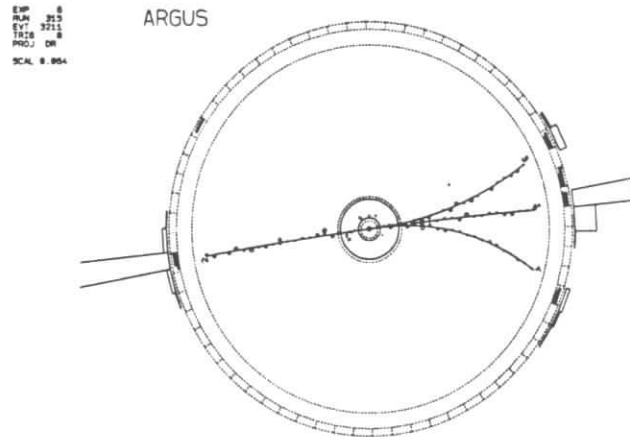
Figure 8.1: Example of radiative Bhabha in ARGUS detector which has 1-3 structure and passes the initial selection cuts. The height of the open rectangles on the outer rim scale in proportion to the energy deposited in the shower counters.

undetected, QED processes tend to conserve total momentum and (in the Bhabha case) deposit all their energy in the calorimeter. This then makes them fairly easy to isolate. Additionally, the e^+e^- conversion pair is highly unlikely to have invariant mass much different from $2m_e$ (discounting detector resolution) and can therefore be inferred from a signal near zero in the two track mass plot, assuming the electron hypothesis.
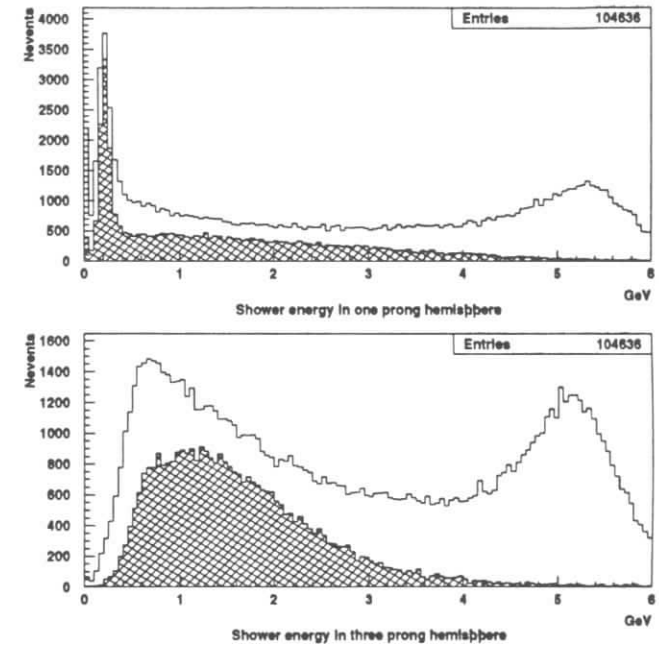
Figure 8.2: Total shower energy deposited in the one-prong and three-prong hemispheres. The broad enhancements around 5GeV are attributable to Bhabha events. The hatched histogram is the corresponding distribution for Monte Carlo tau events (arbitrary normalisation).

Shown in Fig. 8.2 are the distributions of total calorimeter energy in the one-prong and three-prong hemispheres for the initial selection sample. The hemispheres are defined with respect to the direction of the total three-prong momentum $\sum_{i=2}^{4} \vec{p}_i$, e.g. the one-prong hemisphere is the ensemble of directions lying more than 90 degrees from $\sum_{i=2}^{4} \vec{p}_i$. The enhancements at about $5GeV$ are due to radiative Bhabha events. The large width is primarily a reflection of the shower energy resolution. Cuts on the shower energies in each hemisphere were applied to reject this contribution:

$$E_{sh}^{1,3} < 0.4 \cdot E_{cms}. \tag{8.1}$$

Shown in Figure 8.3 is the distribution of total scalar momentum, $P_{tot} =$
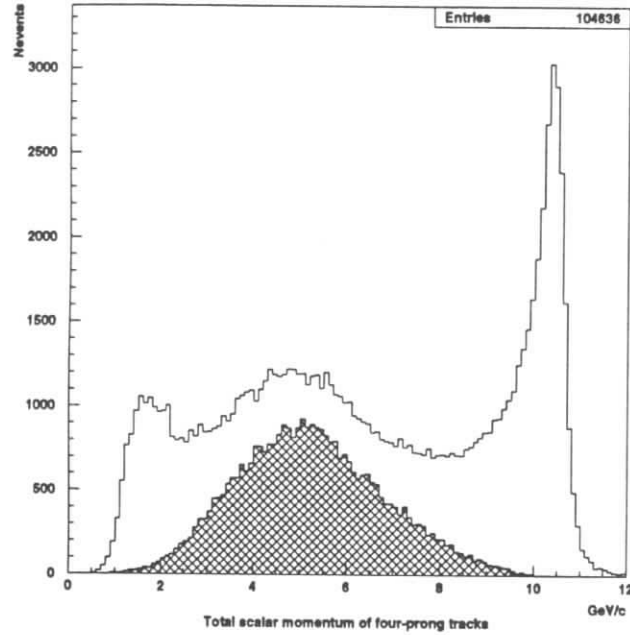
Figure 8.3: Distribution of total scalar momentum of four-prong system for initial data pool. The peak at high momentum reflects a strong QED contamination, that at lower momentum a large two-photon contribution. The hatched histogram is the corresponding distribution for Monte Carlo tau events (arbitrary normalisation).

$\sum_{i=1}^{4} | \vec{P}_i |$, where the sum is over each of the four-prong charged tracks. For electrons, positrons, and reasonably fast muons $| P_i | \simeq E_i$ to a very good approximation and so for QED processes P_{tot} is basically the total energy of the event. Therefore only events with

$$P_{tot} < 0.92 E_{cms}/c \qquad (8.2)$$

were selected for further analysis, thus ensuring further suppression of radiative Bhabha and di-muon events.

The invariant mass plot of all oppositely charged two track combinations on the three-prong side is shown in Figure 8.4. The electron mass hypothesis
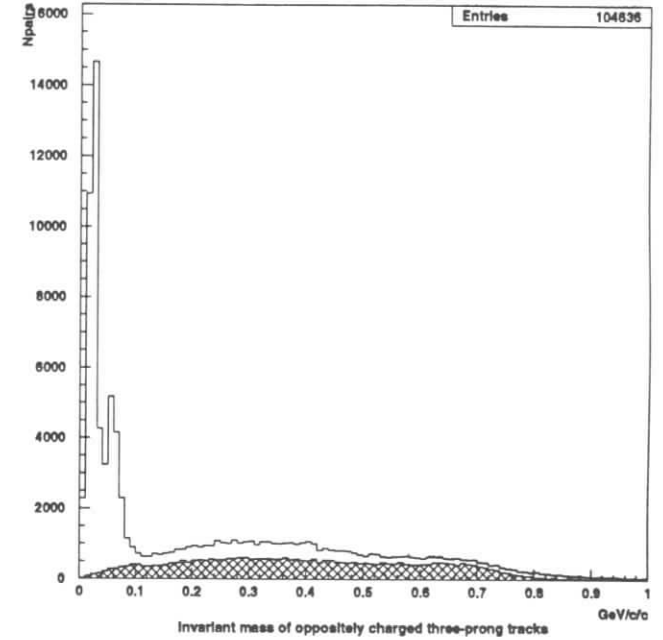
Figure 8.4: Invariant mass of oppositely charged particles in the three-prong hemisphere. The large peak at zero results from photon conversion in the detector. The smaller associated peak comes from combining one of the converted photon tracks with the primary QED particle. The hatched histogram is the corresponding distribution for Monte Carlo tau events (arbitrary normalisation).

was used for both tracks. The peak below $0.1 GeV/c^2$ results from photon conversion in the detector, primarily from radiative Bhabha events. All events having photon conversion candidates with invariant mass less than $0.1 GeV/c^2$ were rejected.

8.4.3 Anti-Two-Photon Event Cuts

Four-prong events can also occur as a result of two-photon (or $\gamma\gamma$) collisions. In this process the beam particles each emit a virtual photon which subsequently interact to produce particles. The probability for emitting a virtual photon is largest for lowest photon energy, therefore the cross section peaks towards low $\gamma\gamma$ invariant masses, with the beam particles continuing to travel down the beam pipe undetected, and carrying most of the event energy. The signatures of such events are therefore (1) low energy and (2) balanced total transverse momentum, $|\sum_1^n \vec{p}_{Ti}|$. The peak at low total scalar momentum in Figure 8.3 is attributed to such events and a cut of

$$P_{tot} > 2.7 GeV/c$$

was applied to capitalise on (1). This cut also suppresses beam gas events. To take advantage of (2), rather than cut directly on the transverse momentum balance, a "parabola cut" was devised [61]. This has a higher background rejection power and better tau selection efficiency. Because it is also important in reducing contamination from multihadron events the description of this cut will be left to the next section.

8.4.4 Anti-Multihadron Cuts

While it is true that $q\bar{q}$ events have a high average charge multiplicity and would therefore appear as unlikely four-prong candidates, the reality is that the cross section for these processes is large and the back-to-back jet nature of the events lends itself easily to satisfying the 1-3 topology, making this the most difficult background to contend with. In contrast, not only do $B\overline{B}$ events have a similar charge multiplicity, their production cross section is comparatively low and their event topology spherical. Consequently, after all selection cuts, they contribute at a negligible level.

Two aspects of the multihadron background that make it vulnerable to suppression are (1) a large total visible energy in the detector and (2) a large number of photons. Because of the the fact that tau events are always accompanied by (often large) missing energy in the form of at least two neutrinos,

the total visible event energy is capable of distinguishing multihadrons from tau events to some extent. The second feature must be true on average if the events are to have only four charged tracks, i.e. an increase in neutral pion production must compensate for the reduced charged multiplicity. In any case the photon multiplicity of multihadrons is much higher than in tau events.

To exploit (1) a standard ARGUS cut on the relationship between transverse momentum balance and total visible momentum was applied,

$$|\sum_1^n \vec{p}_{Ti}| > \left(4.5 \cdot (\sum_1^n |\vec{p}_i|c/E_{cms} - 0.55)^2 + 0.1\right) GeV/c,$$

where the sums include all charged and neutral particles in an event. Observing that the value of the expression in large parentheses is always greater than $0.1 Gev/c$ this cut also rejects two-photon events which, as noted above, tend to have balanced transverse momentum. A further explanation of this cut can be found in [61].

The photon cuts applied to the data were (see Figure 8.5)

$$n_\gamma^1 < 3$$
$$n_\gamma^3 < 3$$
$$n_\gamma^1 + n_\gamma^3 < 4$$

where n_γ^1 and n_γ^3 are the number of photons found in the one and three-prong hemispheres respectively. Here, the definition of a photon is any shower with energy greater than 80MeV (to avoid fakes from noise) and not associated with a charged track (to avoid fake photons from track showers which split in the calorimeter). Accepting two photons on either side allows for the possibility that a neutral pion was produced in the decay of the tau. A single observed photon is also a likely possibility because above about 0.8GeV the photon showers from neutral pion decay are merged in the calorimeter and indistinguishable. To accept more than three photons in total increases the background fraction.
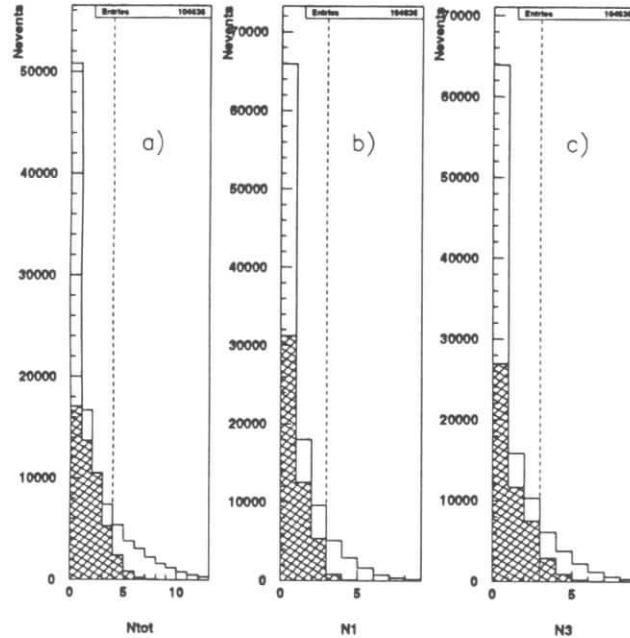
Figure 8.5: Shower multiplicities for experimental data (histogram): a) total number of showers in an event, b) number of showers found in one-prong hemisphere, and c) number of showers found in three-prong hemisphere. The hatched overlay shows the corresponding distributions for tau Monte Carlo data (arbitrary normalisation). The large excesses observed in the zeroth bin of the experimental data are due to radiative QED processes. The dashed lines indicate where the cuts were applied.

8.4.5   Track Quality Cuts

Only events with good quality tracking were considered for further analysis. A cut on the one-prong polar angle of

$$\cos\theta_1 < 0.75$$

was made to ensure good trigger conditions and to ensure that the one-prong track crosses most of the layers in the drift chamber. A total of 18 916 events survive this and all other cuts discussed to this point. Additionally, at least four hits per track in the VDC were required. This reduces the data sample to 14 551 events, from which a naive estimate of 94% for the average VDC reconstruction efficiency can be derived. Also, the cuts on the d_o and z_o impact parameters at the beam line were tightened marginally to $d_o < 1.0$cm and $z_o < 4.0$cm. These are extremely loose cuts (the mean tau path length in the ARGUS detector is 250 microns) but because of the varying position of the nominal interaction point over the data-taking period it was deemed wiser to make a harder cut using the reconstructed three-prong vertex instead (see below). Finally, the error on the one-prong impact parameter d_o, provided by the covariance matrix from the ARGUS track fit, was required to satisfy $\sigma_{d_o} < 0.075$cm.

8.4.6   Anti-Scatter Cuts

No mention has yet been made of tracks in the event sample which do not point back to the interaction point. While it may seem a desirable procedure to reject all events with extra tracks, some are worth keeping. For example, those tracks which result from backscatter in the calorimeter do not affect the physics of the four-prong tracks in any way and need not be rejected. Nor should cosmic ray tracks. Therefore, if a track was not a four-prong member, began and ended in the calorimeter, and came no closer than 25cm to the beamline, it was considered an acceptable extra track. The last criterion avoids the possibility that the track was poorly reconstructed and in fact originated in the inner DC wall, which lies at a radius of 18cm.

Events with any number of valid backscatters were accepted. Events with any other type of extra track were rejected. This includes events in which, for example, a track has inelastically scattered in the wall of the DC or VDC and produced other tracks in the process. The loss in energy to the primary particle affects its curvature and ultimately its reconstructed impact parameter at the beam line, therefore these events are worth rejecting even if they are true tau events. 13 011 events remain after the application of these cuts.

8.4.7   Vertex Cuts

Events with any combination of two charged tracks forming a secondary vertex outside a radius of $r = 3$cm from the beam line were rejected. These include events that have converted photons in the detector which escape the kinematical mass cut described earlier, events with very long lived particles decaying far from the beam line, and events where a particle interacts with the walls to produce a shower. As with the cuts on d_o and z_o noted above, this cut is purposely very loose in order to be absolutely certain that no bias to the tau lifetime measurement is introduced. A cut at $r = 1.5$cm from the beamline, for example, could conceivably reject long-lived tau events with badly reconstructed vertices or events where the tau production point is significantly displaced from the nominal beam line. The value of $r = 3$cm is suggested by a study of Monte Carlo data and was chosen to include the rejection of interactions in the beam pipe wall, which lies at a radius of 4cm. Following the application of these secondary vertex cuts the sample is further reduced to 12 728 events.

Shown in Figure 8.6a) is the distribution of χ^2 values for the three-prong vertex fit for the reduced data sample. The long tail is a result of non-Gaussian track errors (particularly in the case of the VDC) and of large angle multiple scattering. Overlaid is the corresponding distribution for Monte Carlo tau decay. A cut of $\chi^2 < 60$ was chosen. Figure 8.6b) shows the distribution of errors on the vertex impact parameter *dca*, the distance of closest approach of the one-prong to the reconstructed three-prong vertex
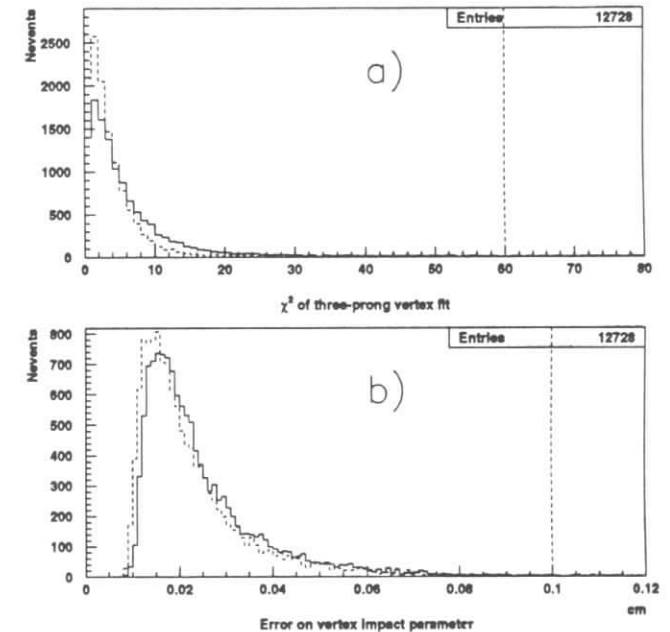
Figure 8.6: Distributions at the vertex: a) the χ^2 of the three-prong vertex fit, and b) the error ascribed to the vertex impact parameter *dca* by the track fit. Both experimental (solid histograms) and Monte Carlo (dashed histograms) data are shown. The vertical dashed lines indicate the location of the cuts applied. See text.

for the same sample. Only events having $\sigma_{dca} < 0.1cm$ were considered for further analysis. The discrepancy between experimental and Monte Carlo data is a result of detector effects not taken into account in the Monte Carlo simulation (e.g. large angle multiple scattering tails and imperfect wire positions). The potential for this discrepancy to bias the lifetime measurement is addressed in Section 8.10. After these vertex cuts 12 215 events remain.

8.5   The Multihadron Background Component

The cuts described in the previous section reduce the QED, $B\overline{B}$, and two-photon components of the data sample to levels well below 1%. Because these cuts closely parallel those of previous ARGUS analyses, e.g. [62], the reader is referred to these for full justification of this statement. In partial justification, the spectrum of likelihoods for any of the the three-prong tracks to be an electron was examined and found to show no indication of Bhabha content, and the angle between the one-prong and three-prong directions showed no indication of a peak at 180°, a signal for Bhabha events.

There still remains a significant multihadron background component to be considered. Shown in Figure 8.7 is the invariant mass of the three-prong assuming each of the tracks is a pion. Because the invariant mass of the three-prong system cannot be greater than the tau mass, all events above $1.8 GeV/c^2$ are assumed to be multihadrons. The shape of the multihadron three-prong mass distribution was derived from a large sample of Monte Carlo $q\overline{q}(\gamma)$ events. This is the hatched region in Figure 8.7, shown normalised to the total number of events above the kinematical mass limit of $1.8 GeV/c^2$. From this the fraction of background events below $1.5 GeV/c^2$ was determined to be

$$f = (3.7 \pm 0.5)\%. \tag{8.3}$$

Only events below this lower mass were accepted for further analysis.

The three-prong mass spectrum also provides a means of determining, using experimental data only, whether the multihadron background contains any particles with finite lifetime. The dca spectrum was examined for events falling above the kinematical limit for tau decay, i.e. $M_{3prong} > 1.8 GeV/c^2$.
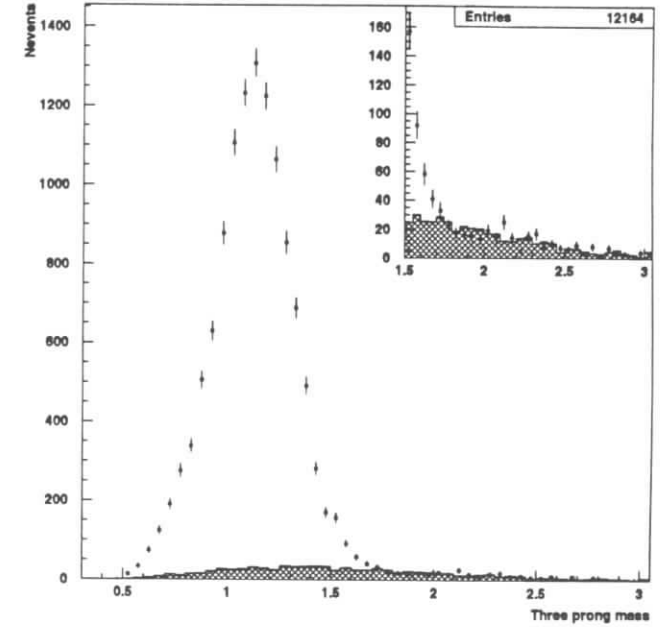
Figure 8.7: The invariant mass of the three-prong system assuming the pion hypothesis for all tracks. The hatched region represents the corresponding multihadron distribution derived from Monte Carlo and has been normalised to the the total number of events above $1.8 GeV/c^2$. The inset histogram provides a closer view of the high mass end of the spectrum.

Figure 8.8a shows the mean *dca* values as a function of M_{3prong} for events
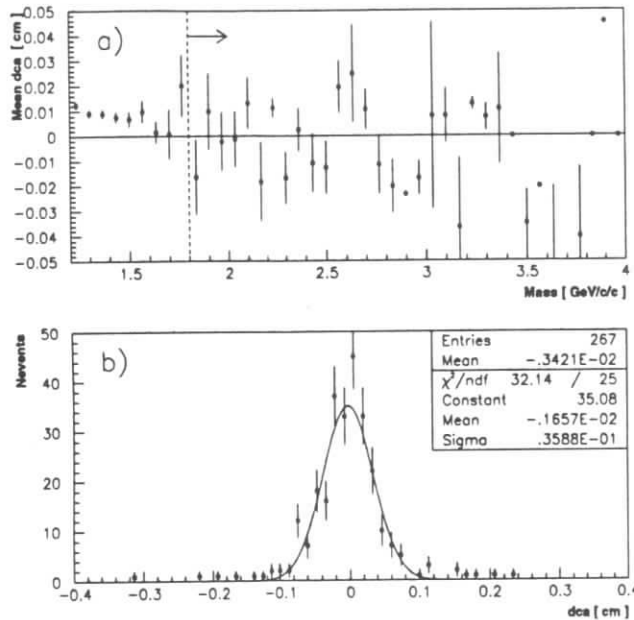
Figure 8.8: Distance of closest approach of the one-prong to the three-prong vertex (*dca*) for the high three-prong invariant mass region. Figure a) shows the mean *dca* value as a function of mass. The dotted vertical line indicates the region used for Figure b) which shows the distribution of *dca* values for the high mass region.

above $1.2GeV/c^2$. Clear positive offsets from zero are observed for bins below about $1.6GeV/c^2$, consistent with the presence of tau events in this mass range. Above $1.6GeV/c^2$ the spectrum appears to be roughly flat and consistent with zero lifetime, although the error bars are large and a stronger statement than this cannot be made. Figure 8.8b gives the distribution of *dca* values for all events falling above $M_{3prong} = 1.8GeV/c^2$, i.e. all events to the right of the dotted vertical line shown in Figure 8.8a. A single Gaussian fit (overlaid) yields -17 ± 24 microns for the mean, consistent with zero

lifetime and in disagreement with the Monte Carlo prediction of (70 ± 14) microns (2.5 standard deviations). A double Gaussian fit with means fixed (not shown) yields a mean *dca* of -9 ± 25 microns. This approach of examining the high mass *dca* spectrum is the one followed in the previous ARGUS analysis of the tau lifetime [34] and the latest tau lifetime measurement by CLEO [63]. In each of those analyses a background lifetime consistent with zero is also observed in the data. However, the cuts used in those analyses are somewhat different from those applied here, and the method used is also different (decay length method). Furthermore, the data sample of the previous ARGUS analysis is not independent of the sample used in the current analysis. Finally, it is not clear that what holds for the upper mass region will necessarily hold for background events in the lower mass region populated by tau events. Therefore, in this analysis the multihadron background component is not assumed to have zero lifetime but rather to have a fraction of lifetime events equal to the Monte Carlo prediction of 30%, and a mean flight path in the $x - y$ plane equal to the Monte Carlo prediction of 490 ± 20 microns (see Chapter 4). The discrepancy between Monte Carlo and experimental data is treated as a systematic error and discussed in Section 8.10, where a possible explanation for the discrepancy is also given.

8.6   The Final Event Sample

After restricting the measured *dca* values to a range consistent with expectations from Monte Carlo taking into account the finite resolution of the detector, i.e.

$$| dca - 0.01 | < 0.4cm,$$

the final data sample comprises 11 494 events. This is the event pool used to measure the tau lifetime at ARGUS. A summary of all cuts applied in obtaining this sample is provided in Table 8.1. Figure 8.9 shows the distribution of fitted three-prong vertices in the $x - y$ plane. Also shown is the position of the DORIS beam pipe. The reconstructed vertices lie well within the beam pipe, and more than 99% of them lie within a circle of radius 0.6cm centred on the beam line position used for the event selection

List of Cuts Applied to the Data

Data quality cuts

$10.43 GeV < E_{cms} < 10.61 GeV$
only runs with good DC and VDC calibration periods
only runs with good detector state

Topology cuts

4 charged tracks, total charge 0
no suspicious extra tracks
$\cos(\vec{p}_1, \vec{p}_i) < 0 \qquad (i = 2, 3, 4)$
$\cos(\vec{p}_1, \vec{p}_{3pr}) < -0.5$
$\cos\theta_1 < 0.75$
$n_\gamma^{1,3} < 3$ and $n_\gamma^1 + n_\gamma^3 < 4$

Kinematic cuts

$p_T > 0.06 GeV/c$
$E_{sh}^{1,3} < 0.4 \cdot E_{cms}$
$2.7 GeV/c < P_{tot} < 0.92 E_{cms}/c$
$|\sum_1^n \vec{p}_{Ti}| > (4.5 \cdot (\sum_1^n |\vec{p}_i| c / E_{cms} - 0.55)^2 + 0.1) GeV/c$
$m_{ij} > 0.1 GeV/c^2$ (electron hypothesis)
$M_{3prong} < 1.5 GeV/c^2$ (pion hypothesis)

Track and vertex cuts

At least 4 VDC hits per track
No secondary vertex within $r = 3.0$cm of beamline
$d_o < 1.0$cm and $z_o < 4.0$cm
$\chi^2_{VTX} < 60$
$\sigma_{d_o} < 0.075$cm
$\sigma_{dca} < 0.1$cm
$|dca - 0.01| < 0.4$cm

Table 8.1: List of selection cuts applied to the data.
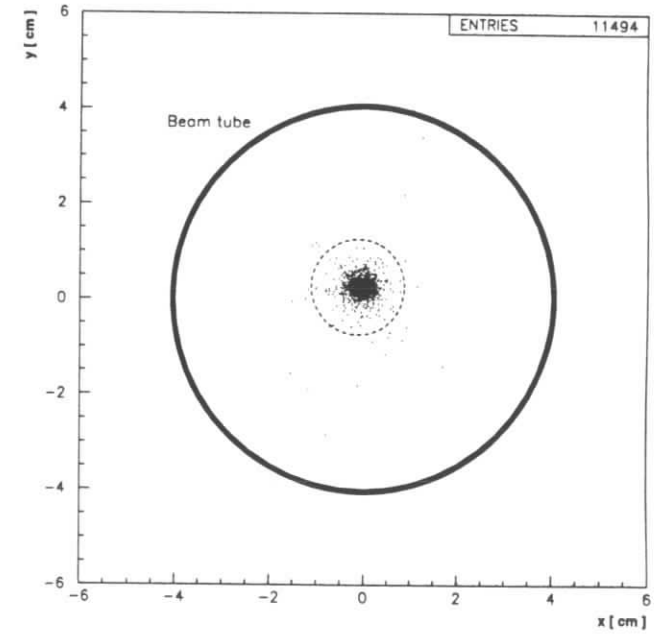
Figure 8.9: Distribution of three-prong vertices for the events used to measure the tau lifetime. Also shown is the position of the beam pipe and the location of the d_o cut (dashed circle) applied to the tracks. See text for further details.

$(x_{beam} = -0.12\text{cm}, y_{beam} = 0.25\text{cm})$. The dashed line at a distance of 1.0cm from this position indicates where the cut was applied on the d_o values of the four-prong tracks during event selection. This distribution gives some confidence that there is little influence from the beam position introduced by the event selection procedure.

Shown in Figure 8.10 are the dca and ψ spectra for these events. The
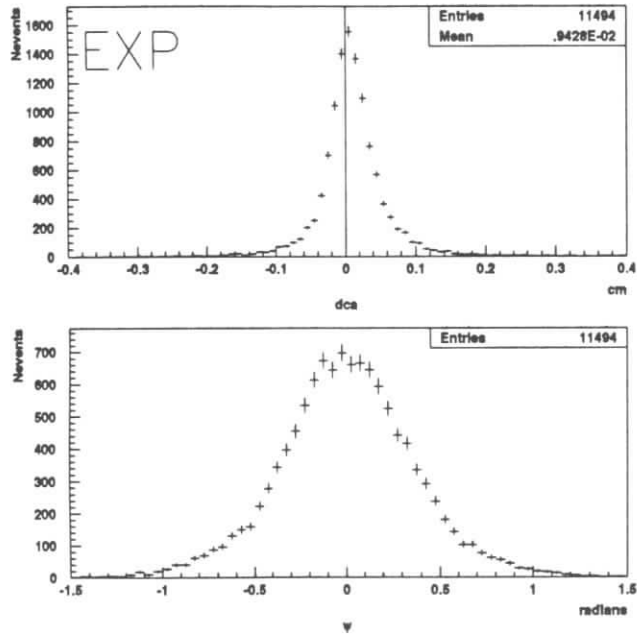
Figure 8.10: The final dca and ψ spectra for the events used to determine the tau lifetime.

dca distribution has a mean shifted from zero of $dca^{EXP} = (94 \pm 5)$ microns, reflecting the lifetime of the tau lepton. The corresponding distributions for a fully simulated Monte Carlo sample of tau events generated with lifetime 303fs and for a fully simulated Monte Carlo sample of multihadron events generated with the LUND 6.3 generator and passing the same cuts as required

of the data are shown in Figures 8.11 and 8.12, respectively. The mean dca
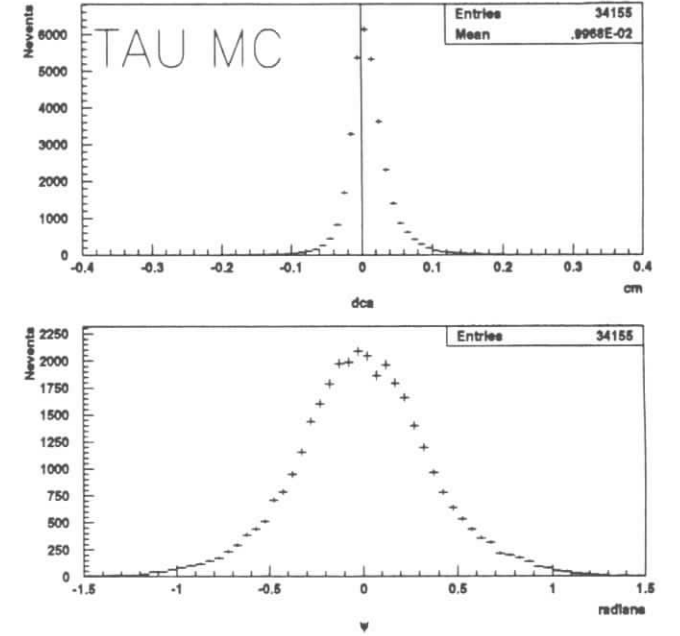
Figure 8.11: The dca and ψ spectra for a fully simulated Monte Carlo tau sample generated with TAUOLA and KORALB and passing all cuts.

values for this Monte Carlo data are $dca^{MC} = (99.7 \pm 1.7)$ microns and $dca^{q\bar{q}} = (70 \pm 14)$ microns for the tau and multihadron samples, respectively. In conjunction with the fraction f of background events (Equation 8.3) these numbers yield a preliminary tau lifetime value of

$$\tau_\tau = dca^{EXP} \cdot \frac{303fs}{[(1-f) \cdot dca^{MC} + f \cdot dca^{q\bar{q}}]} \qquad (8.4)$$
$$= (289 \pm 16)fs \qquad \text{(statistical error only)}.$$

This agrees well with the current world average [1] of $\tau_\tau = (291.0 \pm 1.5)fs$, providing some confidence in the data selection procedure and background fraction determination.
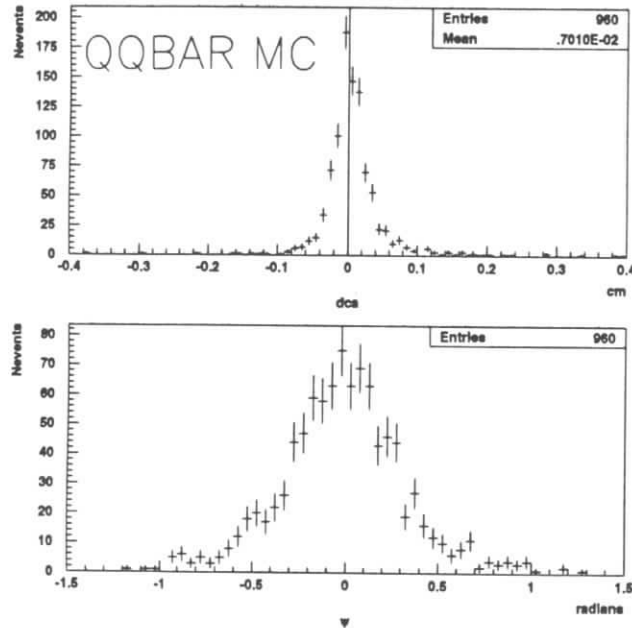
Figure 8.12: The *dca* and ψ spectra for a fully simulated sample of $q\bar{q}$ data generated with the LUND 6.3 program and passing all cuts.

Before discussing the results of applying the more powerful VIP method to the data, the strategy for determining the resolution function for the *dca* variable needs to be described. This is done in the next section. Following that is a brief outline of the method used to correct the data for the track offsets not cured by the ORIFIT procedure.

8.7 Determination of True Track Resolution at the Beam Line

The chamber resolutions provided by the DC and VDC calibrations are used to assign errors to the measured drift distances during track reconstruction. These are then propagated through to errors on the fitted track parameters as described in Chapter 8. The track parameters are used to swim the tracks to the beam line, with the errors blown up according to Equation 6.35. The accuracy of these errors can be investigated by comparing the track parameters of two-prong events at the origin. Di-muon events are ideal for this purpose since they suffer little from from radiative processes, unlike Bhabha events. In principle, then, the two tracks in a di-muon event should come to a common point at the beam line, have the same momentum there, and be back to back in ϕ and θ (within errors). However, the distribution of normalised missed distances at the beam line

$$\delta = \frac{d_o^+ + d_o^-}{\sqrt{\sigma_+^2 + \sigma_-^2}}$$

shown in Figure 7.5, indicates that this is not quite the case, and that the errors are underestimated by about 10-15%. With an earlier calibration procedure this discrepancy was much worse (50%) and an enormous amount of effort went into reducing the discrepancy. To bring the errors into closer agreement is a rather daunting task and for conventional analyses the AR-GUS approach has been the usual one of applying a scale factor to the errors. This implicitly assumes the errors are Gaussian, however, and for a lifetime analysis based on the maximum likelihood method a more accurate description of the resolution function is needed.

Fast muon tracks are not representative of the low energy tracks found in three-prong tau decays (almost entirely pions), and the scale factor required for di-muons or Bhabhas may not be generally valid. The normalised missed distance distribution for low energy two-prong events (typically two-photon events) displays large tails accompanying a central Gaussian core (see Fig-
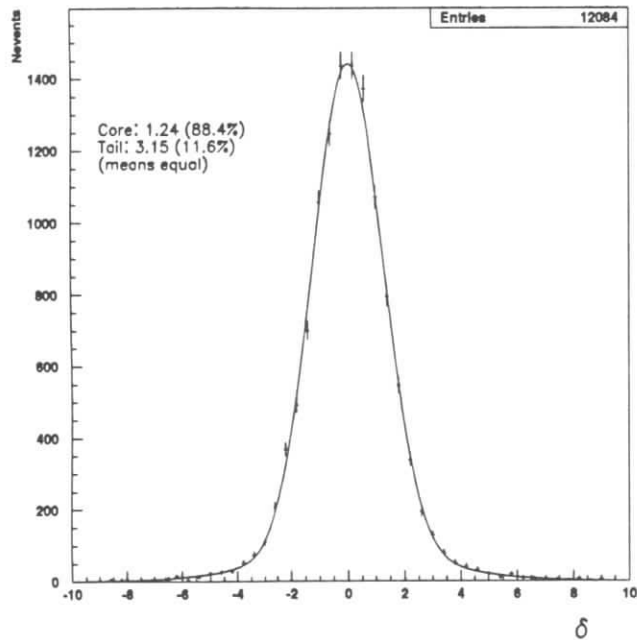
Figure 8.13: Normalised missed distance distribution at the beam line for a sample of low energy two-prongs.

ure 8.13), clearly demanding a more complicated approach than an overall scale factor. There are several reasons for the emergence of tails and a degradation of the resolution for lower energy data. Some of them are listed in the following:

- Poor data taking and calibration - Poor data taking periods are for the

most part rejected for the purpose of this analysis. However, because it is impossible to keep track of and correct for all undesirable influences on the data, periods of poor data taking can creep into the selected data pool. Also, the changing pressure and temperature of the chambers, fluctuations in high voltages, electronics failures, and other destabilizing effects make a proper calibration of the chambers challenging even for good data periods, and the resulting imperfections are reflected in the resolution function. This of course applies for higher energy tracks as well.

- Cell attack angle - Because lower energy tracks have a stronger curvature in the drift chamber they pass through the cells with generally non-radial angles of attack. The calibration procedure uses straight Bhabha tracks which always pass through the cells with essentially radial incidence and the resulting calibration constants are less applicable for other attack angles, i.e. lower momentum tracks. Attempts have been made to develop a ϕ correction to the DTR but the results have been less than satisfactory and not applied in the recalibration of the data.

- Multiple scattering - Multiple scattering in the ARGUS detector is taken into account during the DC track fit, the semi-independent VDC fit, and the swim through the various materials to the beam line. However, the scattering angles are assumed to be Gaussian and this does not account for large angle scatters. Also, the error increase during the swim is performed by modelling the detector materials as bunched up at two scattering radii, which is only approximately realistic. Multiple scattering effects are strongest at low momentum (see Equation 6.27) and therefore play a significant role only in the low energy resolution function.

- dE/dx - Fast tracks are relatively unaffected by fluctuations in energy deposition, while changes to the curvature of lower momentum tracks, which suffer much larger energy losses, lead to large changes in the

impact parameter of the track at the beam line. Fluctuations in energy loss, however, are not taken into account in the track error calculation.

- Wire positions - The wire position determination procedure outlined above uses a layer-by-layer parametrisation of wire shifts. However this way of modelling the shifts is only correct on average for fast tracks. Because of their curvature, lower momentum tracks pass through a much more varied combination of cells than the radially-directed muons used in the ORIFIT procedure, and are therefore more susceptible to flaws in this approach. Also, fast muons are only sensitive to azimuthal shifts in the wire positions whereas lower energy tracks are sensitive to the radial position as well.

The track momenta in two-photon events is unfortunately also outside the range of momenta populated by tau events (too low) and cannot therefore be of service in the extraction of the resolution function. Even if such events could be used there would still remain the question of how to propagate this simple resolution function (derived from the missed distance of the two tracks at the beam line) to the much more complicated 1-3 topology case with the three-prong fit to a common vertex. It is far better to use a sample of four-prong events having similar topology to that of tau decay. To achieve such an independent sample one possibility is to reverse one of the cuts used to select the tau data. Unfortunately, this approach suffers from low statistics and cannot be taken.

A large independent sample of data, having track momenta similar to that in tau decay, exists in multihadron events. These events typically have high charged multiplicity so that a large number of events with $n_{ch} > 4$ is available. By rejecting $n_{ch} - 4$ tracks the events can be converted into four-prongs. Cuts are then applied to the subsystem of four tracks to ensure that only those having topology similar to the tau four-prongs are accepted. This procedure leads to a large number of "events" ideal for the determination of the resolution function for the *dca* variable. In the remainder of this section the details of the selection procedure are given, followed by a description of the method used to determine and parametrise the resolution function for

the *dca* variable.

To maximise the size of the resolution event sample, the $n_{ch} - 4$ tracks were not thrown out at random but rather in a well-defined manner. First, the tracks in an event were ordered according to the magnitude of their momenta, one ordering each for positively and negatively charged tracks. Starting with the pair with highest momentum in each group, the topology of the combined set of four tracks was checked to see if it matched the 1-3 topology structure defined in section 8.4.1. If so this set of tracks was accepted for further consideration. Otherwise, the combination of next-to-highest momentum track pairs was considered. This exercise was repeated until 1) the topology criterion was met (event accepted), 2) the set of possible combinations was exhausted (event rejected), or 3) the number of combinations tried exceeded a pre-defined limit (event rejected). This procedure implicitly ensures that the four-track system has net zero charge, as in tau events. Consideration of the highest momentum tracks first helps to keep the momentum of the subsystem comparable to that in tau events.

The events surviving the above criteria had to satisfy cuts similar to those applied in the data selection procedure:

- $5 \leq n_{ch} \leq 9$

- the number of extra tracks (tracks not members of the four-track system) on the one-prong (three-prong) ≤ 3 (≤ 2) (to avoid multiple occupancy in the DC and VDC cells)

- no combination of tracks on the three-prong side consistent with photon conversion

- at least four VDC hits associated with each four-prong track

- $M_{3prong} < 1.5 \text{Gev/c}^2$ (assuming pion hypothesis for tracks)

- $\cos_{1prong} < 0.75$

- $d_o < 1$cm and $z_o < 4$cm for all four tracks

• some further vertex cuts described below (similar to those applied to the tau data)

The four-track subsystems surviving these cuts look similar to four-prong tau events although the one- and three-prong momentum spectra are shifted to lower values than their tau counterparts.

Assuming for the moment that all tracks in the four-prong system originate from a common vertex, the resolution function for the dca variable can be extracted directly by fitting the three-prong to a common vertex and measuring the missed distance of the one-prong to the three-prong, d. (Here the sign of d is not the same as that of dca but assigned solely according to whether the track passes to the left or the right of the vertex as viewed in the $x - y$ plane.) The same vertex cuts as in the tau event sample were applied to the events, i.e.

• $\chi^2_{VTX} < 60$

• $\sigma_{d_o} < 0.075$cm

• $\sigma_d < 0.1$cm

• and $| d - 0.01 | < 0.4$cm.

In reality multihadron events contain a lifetime component, predominantly charm, that does not respect the assumption of a common production point for all four tracks. This results in a broadening of the distribution of d, or equivalently d/σ_d, which must be taken into account in extracting the true resolution function. The influence of this lifetime component on the missed distance distribution was determined from a large sample of Monte Carlo multihadron data satisfying the same cuts required of the experimental data. A *broadening function* was constructed to carry out the deconvolution. This is defined as the function which upon convolution with the Monte Carlo resolution function yields the observed Monte Carlo normalised missed distance distribution. An empirical parametrisation was used: the sum of a delta function (for the zero lifetime) component and an exponential reflected about $d = 0$ (for the lifetime component) . To determine the parameters of

the broadening function the mean and fractional contribution of the exponential were left free in a fit to the Monte Carlo missed distance distribution.

Plotted in Figure 8.14 is the normalised resolution, i.e. d/σ_d, for the final
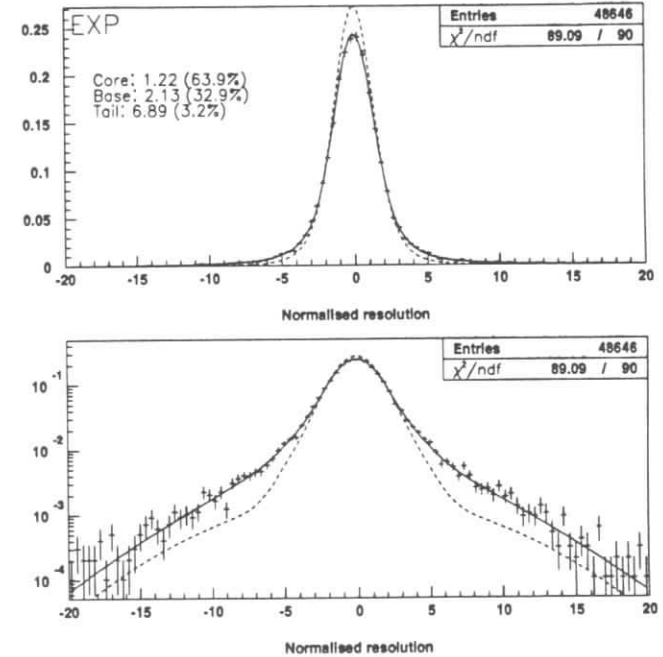
Figure 8.14: Normalised multihadron missed distance distribution for one of the five data-taking periods used in this analysis. Both linear and logarithmic y-axis representations are shown. See text for an explanation of the overlaid functions.

selection of multihadron events from one of the five data-taking periods. A sum of three Gaussians with means equal was used to empirically parametrise the resolution function. Accordingly, this form was convoluted with the Monte Carlo broadening function and a fit to the normalised missed distance distribution made. The broadening function parameters were kept fixed in the fit and the areas and widths of the Gaussians left free. The overlaid

solid lines in Figure 8.14 show the result of this fit. The dashed lines show the corresponding triple Gaussian function alone. This function is taken as the resolution function for this particular data-taking period. The other four data-taking periods display similar forms. The widths and relative areas of the Gaussians are also shown in the figure. As noted earlier, the ideal situation would be to have this distribution a Gaussian of unit width but this is evidently not satisfied.

There are certainly difficulties with this approach to finding the resolution function. In particular, the fact that the corresponding one-prong and three-prong momentum distributions are softer for the multihadron data sample implies that the overall width of the resolution function is potentially over-estimated. (Although the r.m.s. width of the normalised missed distance distribution was found to be reasonably insensitive to the the one-prong and three-prong momenta, there are not enough data to confirm this.) Another problem is that the four-prong angles differ from those in tau decays, despite attempts to select similar topologies. Furthermore, only one resolution function is used for a given data-taking period, ignoring possible changes within the running period, and no attempt is made to take into account dependency on angle, momentum, etc.. Therefore, to compensate for the potential inaccuracy in the resolution function a second free parameter in the VIP likelihood fit is introduced which scales all widths in the resolution function simultaneously by a common factor. This allows the overall width of the resolution function to change, but not its shape. The effect of a change in shape is considered in the systematic error analysis in Section 8.10.

8.8   Determination of Residual Track Offsets at the Beam Line

It can be expected that in four-prong tau events, the three-prong side of the event is relatively immune to residual track offsets because 1) the tracks all point into the same general area of the detector and therefore undergo a roughly common absolute shift and 2) a vertex is reconstructed from the three-prong tracks and this has the advantage of keeping the influence of any

relative offsets in check. In contrast, the missed distance of the one-prong to the three-prong vertex can be seriously affected by tracking inconsistencies because it effectively is a measure of the missed distance of tracks traced from opposite sides of the detector and this has already been shown to have a bias. The strategy for correcting this effect was to determine the average shift for each of the five data-taking periods using the same 1-3 topology "events" selected for the resolution function determination, and correct the variable *dca* on an event-by-event basis. Although it is unlikely that the assumption of a single offset correction for a given data taking period is valid, a finer gradation was not possible due to a lack of statistics. The measured shifts are all of the order of 10 microns, considerably smaller than the shifts first observed in the data before correcting the DC wire positions. Although a 10 micron shift is large compared to the mean *dca* value of 100 microns, the sign convention for *dca* does an excellent job in compensating for its presence and the resulting bias on the tau lifetime measurement is small.

8.9   Extraction of the τ Lifetime Using the VIP Method

In this section the result of applying the VIP method is discussed. First the raw lifetime value, that given by the likelihood fit, is presented. A correction for the method bias observed in Monte Carlo is then applied to yield the final tau lifetime measurement.

The VIP method was applied to the final data sample of 11 494 events using the likelihood function $F(dca, \psi, \sigma)$ of Eq 4.8, reproduced here:

$$F = (1 - f) \cdot F_\tau + f \cdot [(1 - \alpha) \cdot F_{q\bar{q}}^o + \alpha \cdot F_{q\bar{q}}^t].$$

The methods used to determine F_τ, $F_{q\bar{q}}^o$, and $F_{q\bar{q}}^o$ have been outlined in detail in Chapter 4 and Appendix A. Each is based on an underlying distribution, derived from Monte Carlo, which is smeared with the detector resolution function. In each event the measured value of σ_{dca} dictates the shape of the two-dimensional probability density function for observing the variables *dca* and ψ. A relative probability is then assigned to the event based on the

observed values, and the value predicted for the lifetime (defined through its linear relation to the decay length parameter ℓ_o) is the one which maximises the product of all the event probabilities. Instead of maximising that quantity, the equivalent path of minimising the negative of its logarithm was taken using the the MINUIT package [40] which is capable of minimising multivariate functions and providing an estimate of the parameter covariance matrix. The fit is performed with two free variables, an overall scale factor e_{scale}, applied to σ_{dca}, and the lifetime. The reasons for allowing the extra degree of freedom were discussed earlier. The *dca* values are corrected for the shifts observed in the multihadron control samples (see above) prior to determining the relative probabilities. The result of this procedure yields

$$\tau_\tau^{raw} = (281 \pm 10)fs \qquad e_{scale} = 0.981 \pm 0.009 \quad ,$$

indicating a slight tendency to overestimate the errors. The correlation between the two parameters is -26.7%.

Shown in Figure 8.15 is the function corresponding to the VIP fit to the data. This is not a result of a direct fit to the *dca* spectrum but is determined through sampling the shape of the probability density function predicted by the fit values for τ_τ^{raw} and e_{scale}. The agreement is reasonably good. There is, however, a slight indication in the peak and trailing edge of the spectrum that the function does not have the shape required to describe the data.

As shown in Chapter 4 the VIP method when applied to Monte Carlo data underestimates the lifetime by $\Delta_\tau^{MC} = (2.1 \pm 1.3)\%$ (statistical error only). Although barely significant this correction is nevertheless applied to the raw lifetime value. Because the error on Δ_τ^{MC} is due to a lack of Monte Carlo data it is included in the statistical error.

Applying this correction to the raw lifetime value yields the final result for the VIP method,

$$\tau_\tau = (287 \pm 11)fs \quad ,$$

in agreement with the world average. The value is also consistent with the expression derived earlier from the simple *dca* mean of $(289 \pm 16)fs$. However, the VIP method improves the precision by 30%.
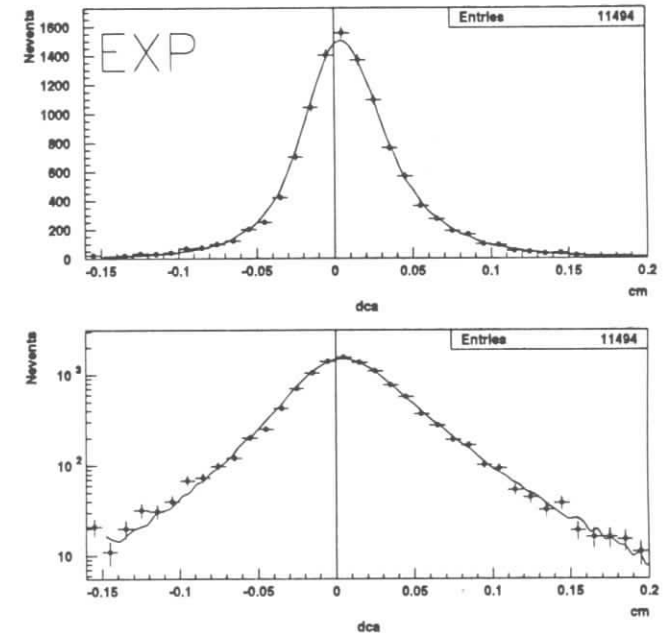
Figure 8.15: Experimental *dca* spectrum with the function corresponding to the likelihood fit overlaid. Linear and log scale views are shown.

In the next and final section of this chapter a description of the various checks made to determine the accuracy of the measurement is given.

8.10 Systematic Error Analysis

Given the statistical precision of the VIP lifetime measurement compared to the LEP, SLD, and CLEO measurements, an exhaustive systematic error analysis would seem unwarranted. However, because the VIP method is being introduced for the first time, it is worthwhile examining the potential accuracy of the method.

8.10.1 Resolution Function

The uncertainty in the resolution function is by far the largest systematic error in this analysis. As with other likelihood function methods for measuring lifetimes, the VIP method is rather sensitive to its form. Leaving the errors free in the fit to scale by an overall factor e_{scale} does help to compensate for any inaccuracy in the overall resolution scale, but cannot correct for a poorly modelled shape.

The technique of allowing the errors to scale by an overall factor was tested on the Monte Carlo data sample. With the scale left free, the VIP method preferred a scale factor of (1.004 ± 0.006) and a lifetime value smaller by 1fs, well within the error of 3.9fs. This test also serves to check the validity of the Monte Carlo resolution function (determined by matching simulated to generated tracks). A value of 1fs was ascribed to the uncertainty in applying this technique.

To estimate the influence of the resolution function shape on the lifetime the parameters of this function were systematically changed and the VIP method repeated using the altered forms. A 10% variation in the Gaussian width of the central core yielded a change of 2.5 fs in the lifetime; a 25% variation in the width of the Gaussian modelling the base yielded a 4.5fs change; and doubling or halving the width of the tails produced an average change of 8fs. The quoted degrees of variation are overconservative estimates

of the ability to define the shape of the resolution function, and safely bracket the sensitivity to the form of the broadening function. More time would be required to do a more complete study of this systematic error. Ideally, a better procedure should be found for extracting the resolution function, so that greater confidence in its reliability can be achieved. This would considerably reduce the systematic error, which is taken to be 6fs.

8.10.2 Physics Functions

One of the main drawbacks of the VIP method is its dependence on Monte Carlo. Inaccuracies in the simulation of tau decays, carried out by the TAUOLA and KORALB packages, are not considered in the estimation of the systematic error because they are expected to be considerably smaller than those due to the modelling of the underlying physics functions. The empirical fits to these distributions (Figure 4.7) are not perfect. This is one of the reasons for the slight bias observed in the VIP method when applied to Monte Carlo.

- Tau Physics Function

  The best of the fits is to the angular distribution of ϕ_1 (χ^2 of 77 for 53 degrees of freedom). By examining the effect of one standard deviation changes in the parameters of this fit, an uncertainty of 1fs in the lifetime value is ascribed to this parametrisation.

  The ϕ_3 fit is by far the worst (χ^2 of 180 for 56 degrees of freedom). Trying two or three Gaussians does not improve the fit much. A different type of function is needed to improve the fit quality. Rather than trying this, the effect of changing the width was studied. Because the fit is poor, a three standard deviation change was considered. This yielded less than a 1fs change in the lifetime. Therefore, a value of 1fs is taken for this systematic error.

  The accuracy of the fit to the distribution of ℓ is more difficult to determine without trying a different functional form. A sum of two exponentials yields a far better fit to the distribution than just one and

in retrospect should have been employed from the start. The single exponential fit has a χ^2 of 128 for 55 degrees of freedom. A three standard deviation change in the parameter l_o changes the lifetime by 3.5fs, which is taken as the systematic error.

- $q\bar{q}$ Physics Function

One standard deviation changes in the total multihadron background produced a lifetime change of 1.5fs, which is taken as an estimate of the uncertainty in the background determination method.

As mentioned earlier there is some uncertainty concerning the fraction of events having lifetime in the multihadron background. The data and the literature suggest a fraction close to zero. The LUND Monte Carlo suggests about 30%. The events having lifetime in a LUND Monte Carlo sample were examined carefully. A K_L^o was present in more than 90% of the events, which were mostly from charm production. This particle has the ability to produce a shower in the calorimeter, and thus mimic a photon. This makes it possible to exclude some events containing them via the photon cuts applied in the event selection stage. If interactions with the detector are not properly simulated a larger fraction of these events have the potential to survive the shower cuts. A quick investigation of the ability of the Monte Carlo simulation program to record K_L^o particles in the shower counters did not indicate anything obviously wrong. Nevertheless, allowing for the possibility that the detector simulation falters for K_L^o particles, and given that the cross section for K_L^o interaction with matter is not well known, it was decided to repeat the the lifetime measurement with the assumption that the background has no lifetime component. This yielded an increase in the lifetime of 1.6fs, which is taken as the systematic error for the uncertainty in the lifetime component of the multihadron background, including both its percent contribution to the total background and its shape.

It is worth mentioning here that in considerably larger sample sizes (e.g. those available at CLEO) which admit tighter cuts without com-

promising the competitiveness of the precision of the measurement, the multihadron background component could be reduced to a harmless level.

From these considerations, the total systematic error ascribed to the physics functions is 4fs.

8.10.3   Vertex Cuts

The cuts at the vertex can bias the lifetime result if they reject long lived taus. They are also sensitive to any non-tau lifetime component in the data, e.g. K_S^o mesons, which increases the vertex fit χ^2 values and the errors on dca. Also, because the detector simulation does not describe the detector perfectly the effect of making these cuts may be slightly different for experimental and Monte Carlo data. For these reasons the cuts are made rather loose. To determine what remaining biases might exist, reasonable variations on the vertex cuts applied to the data were made and systematic errors assigned accordingly. Variations in the cuts on χ^2_{VTX} (30-80), σ_{dca} (0.06-0.12cm), σ_{d0} (0.05-0.08cm), and $|(dca - 0.01)|$ (0.28-0.44cm) lead to systematic error assignments of 0.7fs, 0.2fs, 0.2fs, and 1.5fs, respectively. Taking into account correlations, the overall systematic error assumed for the vertex cuts is 1.5fs.

8.10.4   Tracking and Vertexing

- Monte Carlo

A tremendous amount of work by the author went into ensuring that no bias is introduced by inaccurate tracking in the Monte Carlo data. An assignment of $0.5\mu m$ to the systematic error on the dca variable in Monte Carlo translates into a 1.5fs error on the lifetime.

- Track offsets

The influence of the residual track offsets was determined by 1) applying a common shift of $\pm 20\mu m$ to all offsets (about twice the magnitude of the observed offsets on average), 2) applying the offsets with opposite sign, 3) applying no offsets. The lifetime value was changed by about

1fs in each case. A more complicated procedure of breaking up the data into smaller offset correction periods, or applying random shifts to the data, was not tried. In any case, the sign convention for *dca* makes it fairly insensitive to these track offsets, and a systematic error of 1fs is ascribed to their presence.

• VDC alignment

The VIP method is similarly stable against a misalignment of the VDC. Repeating the measurement with the VDC misaligned within the alignment errors yielded changes of less than 1fs. A much more drastic test was also carried out. Bhabhas from several run regions spread roughly uniformly within the five-data taking periods were selected. The VDC was then aligned using these data for each of these five periods, and the VIP method repeated with the new alignment. A 4fs change was observed in the lifetime. As a check, the alignment procedure was repeated with the di-muon data belonging to each of the data-taking periods. The same 4fs shift was observed. This suggests a strong sensitivity to the alignment. However, as shown in Figure 8.16, the *dca* distribution is significantly broader for this sample, suggesting that the alignment constants are not optimal for the lifetime data sample. As discussed in detail in Chapter 7, there are arguments for why the DC calibration, including the adjustment of the wire positions, may be less valid for lower energy data than it is for Bhabhas and di-muon events. Therefore, a 4fs systematic error is certainly an overestimate of the inaccuracy of the VIP measurement due to the VDC alignment. Instead, a smaller but still rather conservative estimate of 2fs is taken.

• Zero Lifetime Check

The combined ability of the detector and the reconstruction algorithm to reproduce a lifetime of known value was tested. For this purpose, a clean sample of 3379 four-prong $\gamma\gamma$ events was selected according to the criteria outlined in [64]. The sample comprises almost entirely $\rho^\circ\rho^\circ$ production events, and therefore should have a measured lifetime consistent with zero. To maximise the statistics, in events which did not
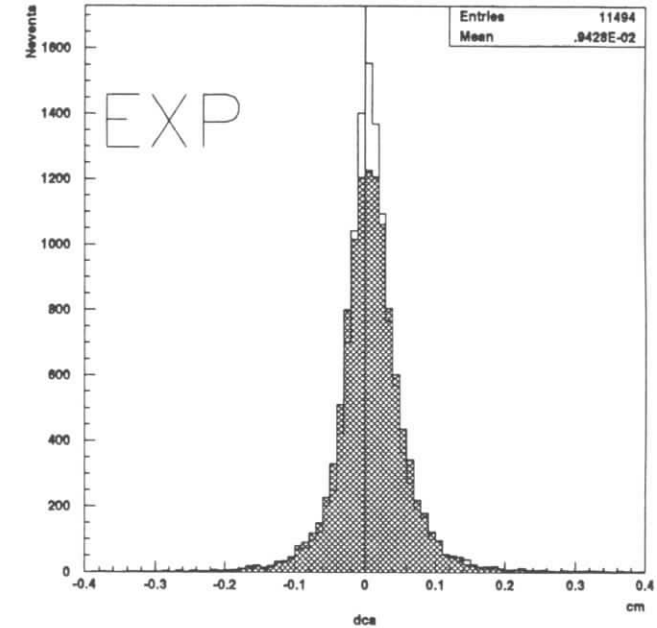
Figure 8.16: Comparison between the experimental *dca* spectra resulting from aligning the VDC with four-prong data (open histogram) and di-muon data (hatched histogram).

satisfy the 1-3 topology of Section 8.4.1, the fastest track was taken as the one-prong. The observed *dca* spectrum for this sample is shown in Figure 8.17, together with a two Gaussian fit (means equal but free) to
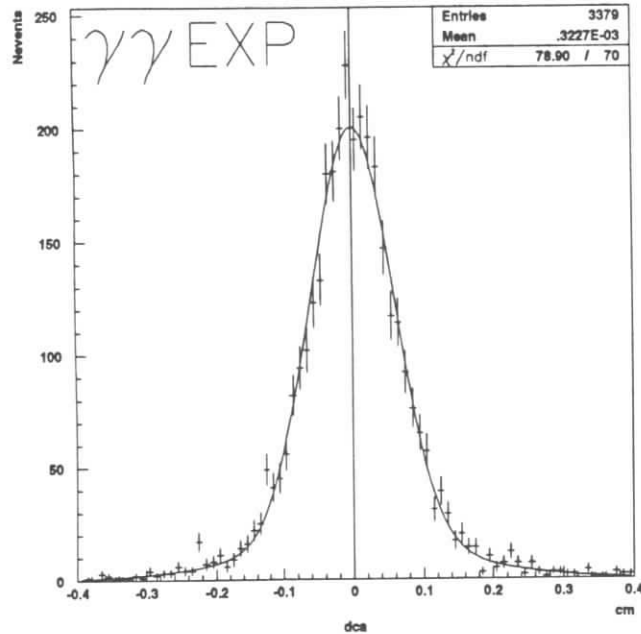
Figure 8.17: The *dca* spectrum for a sample of $\gamma\gamma$ events. The overlaid function is the result of a double Gaussian fit.

the data. The mean of this distribution was found to be 3 ± 14 microns. The fit yields a value of 3 ± 12 microns. Although the statistical significance is not high, these values are consistent with zero, indicating a bias-free measurement procedure. To apply the VIP method, assumptions would have to be made about the underlying physics functions for the angles, and given that the mean *dca* already provides a handle on any bias present, the full method was not applied. Unfortunately, the inability to make a more precise measurement of this effect compro-

mises the significance of the lifetime measurement. A larger sample of four-prong data would be required to do this, but was not available. No correction was applied to the lifetime value to account for this potential bias.

• One-Prong Charge

To test further for tracking inconsistencies, the data sample was split into two halves depending upon the sign of the one-prong charge. The lifetimes reconstructed from the positively and negatively charged one-prong samples were (306 ± 15)fs and (268 ± 15)fs, respectively, a difference of 1.8 standard deviations. Although a bit dissatisfying, this is not outside the realm of possibility (a greater discrepancy would occur in 7% of all experiments). No systematic error was ascribed to this observation, and it is noted here only as a consistency check.

A total systematic error of 2.7fs is taken for the error due to tracking and vertexing.

8.10.5 K_S^o Contamination

Owing to their lifetime, the presence of any K_S^o particles in the data has the potential to bias the tau lifetime measurement, although only a small fraction of tau decays result in a neutral kaon. Many of these events are successfully rejected by the vertex cuts applied to the data, but a tau Monte Carlo study indicates that there still remains a K_S^o component in the data of about (0.6 ± 0.04)% having a mean *dca* value considerably larger than for tau decay. However, because this component is already included in $\Delta_\tau^{MC} = (2.1 \pm 1.3)$%, no correction to the actual lifetime value is applied. This also holds for the multihadron background component, wherein a larger fraction of events contain K_S^o. The systematic errors for the vertex cuts noted above already include to some extent the uncertainty introduced by K_S^o contamination and no additional uncertainty is considered.

8.10.6   Trigger

The average trigger acceptance for the tau four-prongs was found from the Monte Carlo trigger simulation to be $94.5 \pm 0.5\%$ (statistical error only). To determine the influence of the trigger on the lifetime value, the VIP method was repeated using a likelihood function determined without applying the effect of the trigger to the Monte Carlo data (i.e. all events considered triggered). (The multihadron trigger acceptance is closer to unity and no change to the models for the background distributions was applied.) This extreme modification yielded a change of 0.3fs in the lifetime value. Assuming that the trigger simulation is done correctly this implies that the trigger introduces a negligible bias on the lifetime. A conservative estimate of 1fs is ascribed to the systematic error due to the trigger simulation.

8.10.7   Total Systematic Error and Final Result

An additional assignment of 1fs uncertainty is included for the detector simulation, knowledge of the beam energy and spread in centre of mass energies in the data. Table 8.2 provides a summary of the various sources of uncertainty investigated. Adding the errors in quadrature, the total systematic error is found to be 8fs, dominated by the resolution function. The final value for the tau lifetime using the VIP method is therefore,

$$\tau_\tau = 287 \pm 11(statistical) \pm 8(systematic) \text{ fs} \quad,$$

in excellent agreement with the current world average value of

$$\tau_\tau^{w.a.} = (291.0 \pm 1.5)\text{fs}.$$

While this result does not have the precision or accuracy of the better measurements shown in Figure 3.4, a data sample with higher statistics or which benefits from the superior tracking resolution provided by silicon detectors would yield a lifetime estimate with much improved statistical and systematic errors. This is discussed in more detail in the next and final section.

Summary of Systematic Errors

Source of error		Size of effect (fs)
Resolution function:		
	scaling factor in fit	1.0
	shape	6.0
Physics functions:		
	τ	3.7
	$q\bar{q}$ fraction	1.5
	$q\bar{q}$ lifetime component	1.6
Vertex cuts:		
	χ^2_{VTX}	0.7
	σ_{dca}	0.2
	σ_{d0}	0.2
	$|(dca - .01)|$	1.5
Tracking:		
	MC	1.5
	offsets at beamline	1.0
	VDC alignment	1.5
Trigger:		
		1.0
Other:		
		1.0
	Total:	8.0

Table 8.2: Summary of systematic errors.

8.11 Recommendations and Conclusion

Of the methods described in Chapter 3 the VIP method is most like the IPS method which uses (roughly) the distance between two tracks in 1-1 topology tau decays as a lifetime indicator. In the VIP case the fitted vertex and three-prong momentum define the second one-prong "track". Similar to the VIP method a likelihood function is built using the observed track angles in the $r-\phi$ plane. However, whereas the IPS method relies on the beam spot to provide a reference point for the impact parameter measurement, the VIP method uses the three-prong decay vertex, thus eliminating any dependence upon the beam spot other than possibly for data selection purposes. As demonstrated by this analysis, however, it is possible to carry out the selection procedure without introducing any significant dependence upon the beam spot (see Figure 8.9).

The results of applying the VIP method to ARGUS data are very promising. They indicate that the method is in principle a reliable estimator of the tau lifetime. However, certain important checks could not be completed to satisfaction, e.g. whether the method correctly reproduces the lifetime of a data sample of known lifetime, and more study is required. Due to a lack of statistics and a depletion of resources like disk space, computer processing power, and freely available expert advice, ARGUS has not been the ideal testing ground for the method. Therefore, the strongest recommendation the author can make is that the method be applied at CLEO, where a very large data sample exists. A large data sample would enable a proper study and determination of the dca resolution function, a close check of the tracking accuracy, and a more complete suppression of the multihadron background contamination. A proper treatment of these factors could bring the systematic error down to levels comparable to those quoted in various other studies (see below). The method is also applicable at LEP or SLC, but as discussed in Chapter 3 there are a wide variety of powerful methods already available to the experiments at these machines.

There are several improvements that can be made to the analysis.

The calibration of the drift chamber could be considerably improved by

using separate distance-time relations and resolution functions for axial and stereo layers. In retrospect, this would have helped correct some of the asymmetries between the two types of cells that are observed during calibration, and possibly facilitate a proper determination of the z-dependence of the wire positions.

In the ORIFIT procedure for estimating the DC wire positions a constraint to the beam energy could be included in the fit, although it is not clear that the extra constraint would help to improve the situation for lower energy tracks. Also, fitting tracks with just the axial wire hits (after determining θ and z from a fit using the full information) would enable a study of the positions of the stereo layers at some level. A calculation of the wire deflections due to electrostatic and gravitational forces could help to correct some of the z-dependence observed in their positions.

For the determination of the resolution function and residual track offsets, the use of a weighting procedure to select events from the multihadron sample so that they have similar topology and kinematics to 1-3 tau decays is strongly suggested. Also, separate resolution functions for each one-prong particle ID type (muon, electron, hadron) should be used and parametrised in terms of angle and momentum. A finer gradation in the validity periods would obviously improve the measurement as well. There were not enough data available to apply any of these suggestions to the present analysis. A larger data sample would allow a much more accurate description of the resolution function.

There are several possible improvements to the VIP method itself. Certainly the most obvious one is to parametrise the physics functions more carefully. Another is to include another parameter in the fit to characterise the overall shape of resolution function. By far the most interesting one, however, is to take into account the correlation between momentum and angle in the physics functions. The dca spectrum is much narrower, for example, for higher one-prong and three-prong momenta because these directions become more correlated with the tau decay axis. This has obvious consequences for the distributions of ϕ_1 and ϕ_3 used to determine the likelihood function. Rather than using average distributions, the forms can be parametrised in

terms of momentum. Admittedly, this is a more difficult task as it requires a considerable amount of Monte Carlo to get a proper parametrisation of the two-dimensional $p - \phi$ distribution. An attempt was made by the author to do this but due to time constraints this path was abandoned. A proper treatment of $p - \phi$ correlations would lead to a more precise but probably less accurate (due to the difficulties in modelling the $p - \phi$ distribution) lifetime measurement. In this form the *momentum dependent vertex impact parameter method* would be most like a combination of the IPS and MIPS methods.

The potential accuracy of the method is far better than the 8fs quoted. The largest contributions to the systematic error are due to the resolution function (6fs), to the the modelling of the likelihood function (4fs), and to tracking (2.7fs). Typical values of (2-3)fs for the systematic error introduced by the resolution function are currently quoted in the literature, and it is not unreasonable to expect a similar accuracy with a more careful study of a higher statistics sample. Most of the uncertainty arising from the likelihood function comes from ℓ_o (3.5fs); with an improved modelling scheme and a larger Monte Carlo database this could be reduced to 1fs, bringing the entire contribution from the likelihood function to below 2fs. The tracking contribution is dominated by the VDC alignment (2fs) and by the Monte Carlo tracking accuracy (1.5fs), both of which could be considerably improved at another experiment (the contribution due to misalignment quoted in various other analyses is typically 0.5fs.), so that a total tracking contribution below 1.5fs could be achieved. Reevaluating the total systematic error contribution, an accuracy better than 4fs can be expected from the VIP method. This fares reasonably well in comparison with the accuracies indicated in Figure 3.4 , although the techniques applied at LEP still appear to dominate. However, the LEP results are not single measurements but rather weighted averages of the lifetimes measured using several methods, so a direct comparison is misleading. For example, the ALEPH lifetime value using the method most similar to the VIP method (the IPS method) has a systematic uncertainty of 3.4fs, which is likely also achievable with the VIP method.

In conclusion, this thesis introduces a new technique for measuring the

tau lifetime, the *vertex impact parameter* (VIP) method. Applied to ARGUS data the method yields a lifetime value of

$$\tau_\tau = 287 \pm 11(statistical) \pm 8(systematic) \quad \text{fs},$$

in excellent agreement with the current world average value of

$$\tau_\tau^{w.a.} = (291.0 \pm 1.5)\text{fs}.$$

Appendix A

Derivation of the 2-D Likelihood Function

The expression for the likelihood function used to measure the tau lifetime is derived here in its entirety.

Figure 4.8 shows the variables used to derive the two-dimensional likelihood function $F(dca, \psi)$ for tau decays. The signs of the variables ϕ_1 and ϕ_3 are important: the daughter directions are considered positive if they deviate counter-clockwise from the tau production axis, therefore both angles are positive in the figure. The unsigned variable ψ can be defined in terms of them:

$$\psi = |\phi_1 - \phi_3|. \tag{A.1}$$

The variable ℓ is always positive and can be related directly to the observable dca (hereafter referred to as d to make the formalism less cluttered),

$$d = dca = \ell \cdot \sin(\phi_1) \cdot sign(\phi_1 - \phi_3). \tag{A.2}$$

A bit of thought will convince the reader that this expression endows d with the correct sign, i.e. as defined in Section 3.2: unphysical configurations of the three-prong tau direction (as defined through the three-prong momentum), the three-prong decay point and the one-prong direction are associated with negative d values.

Ignoring any correlation in the angles ϕ_1 and ϕ_3 that might be introduced by cuts or spin-spin correlations, the three variables ϕ_1, ϕ_3, and ℓ are independent. The probability density function for observing the triplet $\{\phi_1, \phi_3, \ell\}$ is

therefore simply the product of their individual probability density functions, i.e.,

$$P(\phi_1, \phi_3, \ell)d\phi_1 d\phi_3 d\ell = h(\phi_1) \cdot g(\phi_3) \cdot f(\ell)d\phi_1 d\phi_3 d\ell. \tag{A.3}$$

Because we are only interested in the the probability density function for observing the pair $\{d, \psi\}$ we can make a change of variables from $\{\ell, \phi_3, \phi_1\}$ to $\{d, \psi, \phi_1\}$ and integrate over the third unobserved variable, which in this case is chosen to be ϕ_1. The change of variables introduces a Jacobian factor $|J|$ where

$$J^{-1} = \begin{vmatrix} \frac{\partial d}{\partial \phi_3} & \frac{\partial d}{\partial \ell} \\ \frac{\partial \psi}{\partial \phi_3} & \frac{\partial \psi}{\partial \ell} \end{vmatrix} = \begin{vmatrix} 0 & \sin\phi_1 \cdot sign(\phi_1 - \phi_3) \\ -sign(\phi_1 - \phi_3) & 0 \end{vmatrix} = \sin\phi_1. \tag{A.4}$$

The symmetry about the tau production axis makes it unnecessary to carry out the integral over all phase space. One could, for example, restrict the integral to positive ϕ_1 values or ϕ_3 values and simply multiply the result by a factor of 2. The definitions of d and ψ, however, suggest it might be advantageous to restrict the integral instead to

$$\phi_1 - \phi_3 > 0. \tag{A.5}$$

Although not immediately obvious this choice also simplifies matters further on in the calculation of the likelihood function. The simplified forms of d and ψ become

$$d = \ell \sin \phi_1 \tag{A.6}$$

and

$$\psi = \phi_1 - \phi_3. \tag{A.7}$$

Note that by considering only positive ψ values, the condition A.5 is implicitly satisfied. The joint probability density function is then given by

$$F(d', \psi') = 2 \int_{\phi_1} \frac{d\phi_1}{\sin(\phi_1)} h(\phi_1) \cdot g(\phi_1 - \psi') \cdot f(\frac{d'}{\sin(\phi_1)}) \tag{A.8}$$

where the primes have been introduced to indicate explicitly that these variables describe the situation before the effect of detector smearing is taken into account. The smearing in d is far greater than that in ψ, which is to

a very good approximation the same as that actual angle observed at the reconstruction level, $\psi \approx \psi'$. Therefore, the smearing in ψ' is neglected here, and to relate the likelihood function for the actual variables d' and ψ' to that of their measured counterparts it is only necessary to account for a finite uncertainty in d. This is done using the resolution function $R(\epsilon)$ which gives the probability for observing the measured value $d = d' + \epsilon$ given the actual value d'. The expression A.8 is then convoluted with this resolution function to yield the full probability density function:

$$F(d, \psi) = 2 \int_{\epsilon} d\epsilon R(\epsilon) \int_{\phi_1} \frac{d\phi_1}{\sin(\phi_1)} h(\phi_1) \cdot g(\phi_1 - \psi) \cdot f(\frac{d - \epsilon}{\sin(\phi_1)}). \quad \text{(A.9)}$$

For arbitrary choices of the functions f, g and h, this expression has in general no closed form. The double integral is much too time consuming, however, to perform accurately with a numerical package. Fortunately, with the choice of function $f(\ell)$ given by 4.4,

$$f(\ell) = \frac{\ell}{\ell_o^2} \times e^{-\ell/\ell_o}, \quad \text{(A.10)}$$

and with the resolution function parametrised by a sum of Gaussians,

$$R(\epsilon; \sigma_1, \sigma_2 ..., \sigma_n) = \sum_{i=1}^{n} c_i G(\epsilon; \sigma_i) \quad \text{(A.11)}$$

$$G(\epsilon, \sigma) = \frac{1}{\sqrt{2\pi\sigma^2}} e^{-\frac{\epsilon^2}{2\sigma^2}},$$

$$\sum_{i=1}^{n} c_i = 1 \quad (c_i \geq 0 \ \forall i)$$

the expression A.9 can be reduced to a single integral by reversing the order of integration and performing the integral over ϵ first. Thus, the likelihood function becomes

$$F(d, \psi) = 2 \int_{\phi_1} \frac{d\phi_1}{\sin(\phi_1)} h(\phi_1) \cdot g(\phi_1 - \psi) \int_{\epsilon} d\epsilon R(\epsilon) \cdot f(\frac{d - \epsilon}{\sin(\phi_1)})$$

$$= \frac{2}{\ell_o^2} \sum_{i=1}^{n} c_i \int_{\phi_1} \frac{d\phi_1}{\sin^2(\phi_1)} h(\phi_1) \cdot g(\phi_1 - \psi) \cdot I(\phi_1, d, \sigma_i) \quad \text{(A.12)}$$

$$I(\phi_1, d, \sigma) = \frac{1}{\sqrt{2\pi\sigma^2}} \int_{\epsilon} d\epsilon \cdot e^{-\frac{\epsilon^2}{2\sigma^2}} \cdot (d - \epsilon) \cdot e^{-\frac{(d - \epsilon)}{\ell_o \sin \phi_1}} \quad \text{(A.13)}$$

It is necessary to proceed with some caution when dealing with the limits here. The range of ϵ is not completely unconstrained but depends upon the value of ϕ_1. This can be seen directly from the expression for d'. Because ℓ is always positive the condition

$$\frac{d'}{\sin \phi_1} = \frac{d - \epsilon}{\sin \phi_1} > 0 \quad \text{(A.14)}$$

must hold. Therefore,

$$-\infty < \epsilon < d \quad \text{for} \quad \phi_1 > 0 \quad \text{(A.15)}$$

$$d < \epsilon < \infty \quad \text{for} \quad \phi_1 < 0. \quad \text{(A.16)}$$

The range of ϕ_1 is mathematically unconstrained but physically lies within roughly $\pm\phi_1^{max} = \pm\frac{\pi}{2}$ at ARGUS energies. (See the distributions in Chapter 4.) Putting these limits in explicitly, and making use of the symmetry of the functions g and h, F becomes

$$F(d, \psi) \quad \text{(A.17)}$$

$$= \frac{2}{\ell_o^2} \sum_{i=1}^{n} c_i \int_0^{\phi_1^{max}} \left[\frac{d\phi_1}{\sin^2(\phi_1)} h(\phi_1) \cdot g(\phi_1 - \psi) \right.$$
$$\left. \cdot \frac{1}{\sqrt{2\pi\sigma_i^2}} \int_{-\infty}^{d} d\epsilon \cdot e^{-\frac{\epsilon^2}{2\sigma_i^2}} \cdot (d - \epsilon) \cdot e^{-\frac{(d-\epsilon)}{\ell_o \sin \phi_1}} \right]$$

$$+ \frac{2}{\ell_o^2} \sum_{i=1}^{n} c_i \int_{-\phi_1^{max}}^{0} \left[\frac{d\phi_1}{\sin^2(\phi_1)} h(\phi_1) \cdot g(\phi_1 - \psi) \right.$$
$$\left. \cdot \frac{1}{\sqrt{2\pi\sigma_i^2}} \int_d^{\infty} d\epsilon \cdot e^{-\frac{\epsilon^2}{2\sigma_i^2}} \cdot (d - \epsilon) \cdot e^{-\frac{(d-\epsilon)}{\ell_o \sin \phi_1}} \right]$$

$$= \frac{2}{\ell_o^2} \sum_{i=1}^{n} c_i \int_0^{\phi_1^{max}} \left[\frac{d\phi_1}{\sin^2(\phi_1)} h(\phi_1) \cdot g(\phi_1 - \psi) \right.$$
$$\left. \cdot \frac{1}{\sqrt{2\pi\sigma_i^2}} \int_d^{\infty} d\epsilon \cdot e^{-\frac{\epsilon^2}{2\sigma_i^2}} \cdot (\epsilon + d) \cdot e^{-\frac{(\epsilon+d)}{\ell_o \sin \phi_1}} \right]$$

$$+ \frac{2}{\ell_o^2} \sum_{i=1}^{n} c_i \int_0^{\phi_1^{max}} \left[\frac{d\phi_1}{\sin^2(\phi_1)} h(\phi_1) \cdot g(\phi_1 + \psi) \right.$$
$$\left. \cdot \frac{1}{\sqrt{2\pi\sigma_i^2}} \int_d^{\infty} d\epsilon \cdot e^{-\frac{\epsilon^2}{2\sigma_i^2}} \cdot (\epsilon - d) \cdot e^{-\frac{(\epsilon-d)}{\ell_o \sin \phi_1}} \right]$$

$$= \frac{2}{\ell_o^2} \sum_{i=1}^{n} c_i \int_0^{\phi_1^{max}} \left[\frac{d\phi_1}{\sin^2(\phi_1)} h(\phi_1) \right.$$
$$\left. \cdot [g(\phi_1 - \psi) \cdot I(\phi_1, -d, \sigma_i) + g(\phi_1 + \psi) \cdot I(\phi_1, d, \sigma_i)] \right]$$

where

$$I(\phi_1, d, \sigma) \frac{1}{\sqrt{2\pi\sigma^2}} \int_d^{\infty} d\epsilon \cdot e^{-\frac{\epsilon^2}{2\sigma^2}} \cdot (\epsilon - d) \cdot e^{-\frac{(\epsilon-d)}{\ell_o \sin \phi_1}}. \quad \text{(A.18)}$$

A straight-forward but tedious calculation yields the following expression for the integral I:

$$I(\phi_1, d, \sigma) = \sqrt{2\sigma^2} e^{-\frac{d^2}{2\sigma^2}} \cdot Q(z) \tag{A.19}$$

$$Q(z) = \frac{1}{2\sqrt{\pi}} - \frac{1}{2} z e^{z^2} \mathrm{erfc}(z) \tag{A.20}$$

$$z = \frac{1}{\sqrt{2\sigma^2}} \cdot \left[d + \frac{\sigma^2}{\ell_o \sin\phi_1} \right] \tag{A.21}$$

The function $Q(z)$ is awkward to code correctly for the following reasons (the numbers quoted are for an HP-UX 9000 platform and are approximate):

- the function e^{z^2} blows up for $z^2 > 709$ leading to overflow problems; and

- the function $\mathrm{erfc}(z)$ gets set to 0 and 2 for $z > 8.9$ and $z < -5.53$, respectively making it discontinuous at these boundaries.

The value of z often goes outside these bounds. Left uncorrected these characteristics of the function $Q(z)$ play havoc with the fit and lead to biased results. For example, because $\mathrm{erfc}(z)$ goes to zero for large z it is not difficult to imagine that the product $z e^{z^2} \mathrm{erfc}(z)$ might stay finite or tend to zero rather than be blown up by the exponential. Yet this term in Q consistently gets set to zero for $z > 8.9$ because the limited machine precision forces the value of $\mathrm{erfc}(z)$ to be zero. This nullifies the contribution of this term to the likelihood function, effectively changing the apparent weight of the event in the lifetime fit, a situation which must obviously be avoided. In fact, for large positive z the second term *is* finite and has the the form [65]

$$z e^{z^2} \mathrm{erfc}(z) \approx \frac{1}{\sqrt{\pi}} [1 + \sum_{m=1}^{\infty} (-1)^m \frac{1 \cdot 3...(2m-1)}{(2z^2)^m}], \tag{A.22}$$

so that in the large z limit $Q(z)$ has the value

$$Q(z)_{z \to +\infty} \approx \frac{-1}{2\sqrt{\pi}} \sum_{m=1}^{\infty} (-1)^m \frac{1 \cdot 3...(2m-1)}{(2z^2)^m}. \tag{A.23}$$

This approximation [1] is used for $Q(z)$ for $z > 8.8$. For negative z the function $Q(z)$ can be recast as

$$Q(-|z|) = \frac{1}{2\sqrt{\pi}} + \frac{1}{2} |z| e^{|z|^2} \mathrm{erfc}(-|z|) \tag{A.24}$$

$$= \frac{1}{2\sqrt{\pi}} + \frac{1}{2} |z| e^{|z|^2} [2 - \mathrm{erfc}(|z|)] \tag{A.25}$$

$$= \frac{1}{2\sqrt{\pi}} - \frac{1}{2} |z| e^{|z|^2} \mathrm{erfc}(|z|) + |z| e^{|z|^2} \tag{A.26}$$

so that for large negative z values $Q(z)$ has the form

$$Q(z)_{z \to -\infty} \approx |z| e^{|z|^2} - \frac{1}{2\sqrt{\pi}} \sum_{m=1}^{\infty} (-1)^m \frac{1 \cdot 3...(2m-1)}{(2z^2)^m}, \tag{A.27}$$

wherein the first term obviously dominates and, as noted above, leads to overflow problems for $z^2 > 709$. To cure this and other remaining overflow and underflow problems, calculations are done as much as possible using logarithms. In this way extreme argument values in exponentials can be mitigated by other factors in the likelihood function.

The coding of the likelihood function was checked carefully with a simple FORTRAN algorithm which

- generates simple MC tau events having the input distributions g, h, and f,

- builds the variables dca and ψ from them, and

- smears dca with a known input resolution function R.

Datasets generated in this way were then processed using the VIP method with the same input distributions g, h, f, and R. A wide range of input parameters were tested. In all cases the value for the lifetime variable ℓ_o was successfully reproduced. Although this does not mean that the VIP method is unbiased, it does confirm that the likelihood function has been properly coded.

---

[1] Note that expression A.22 is an asymptotic expansion, valid for large z, and is not to be considered a strict equality.

Appendix B

Di-Muon Constrained Track Fit at Beam line

This appendix details the fit procedure (ORIFIT) used to determine the best estimate of the true track parameters in a di-muon event at the beam line, given the track parameters and their covariance matrices there. These are provided by the track fit and swim-to-beam-line algorithms discussed in Chapter 6. A χ^2 minimisation procedure is employed.

The assumption here is that the combined system of the two true tracks has zero linear and angular momentum, i.e. that

$$
\begin{aligned}
z &= z_+ &&= z_- \\
d &= d_+ &&= -d_- \\
\kappa &= \kappa_+ &&= -\kappa_- \\
\cot\theta &= \cot\theta_+ &&= -\cot\theta_- \\
\phi &= \phi_+ &&= \phi_- + \pi
\end{aligned}
\tag{B.1}
$$

where the $+$ and $-$ serve to label the best estimates of the positive and negative muon tracks, respectively. Denoting the five-dimensional column vectors of true and observed track parameter differences by Δ_+ and Δ_- the following χ^2 is minimised:

$$
\chi^2 = \Delta_+^T V_+ \Delta_+ + \Delta_-^T V_- \Delta_-
\tag{B.2}
$$

where V_+ and V_- are the covariance matrices of the positive and negative

track parameters at the origin, respectively, and $\Delta_\pm$ are explicitly given by

$$
\Delta_+ =
\begin{pmatrix}
d_+ - \overline{d}_+ \\
z_+ - \overline{z}_+ \\
\kappa_+ - \overline{\kappa}_+ \\
\cot\theta_+ - \overline{\cot\theta}_+ \\
\phi_+ - \overline{\phi}_+
\end{pmatrix}
=
\begin{pmatrix}
d - \overline{d}_+ \\
z - \overline{z}_+ \\
\kappa - \overline{\kappa}_+ \\
\cot\theta - \overline{\cot\theta}_+ \\
\phi - \overline{\phi}_+
\end{pmatrix}
\tag{B.3}
$$

and

$$
\Delta_- =
\begin{pmatrix}
d_- - \overline{d}_- \\
z_- - \overline{z}_- \\
\kappa_- - \overline{\kappa}_- \\
\cot\theta_- - \overline{\cot\theta}_- \\
\phi_- - \overline{\phi}_-
\end{pmatrix}
=
\begin{pmatrix}
-d - \overline{d}_- \\
z - \overline{z}_- \\
-\kappa - \overline{\kappa}_- \\
-\cot\theta - \overline{\cot\theta}_- \\
\phi - \overline{\phi}_- - \pi
\end{pmatrix}.
\tag{B.4}
$$

The overlined variables denote the measured track parameters. These are kept constant in the minimisation of the the χ^2 with respect to the five variables d, z, κ, $\cot\theta$, and ϕ. The best estimate of the true track parameters is then given by the set of variables that minimises expression B.2, i.e., for which the derivative of B.2 is simultaneously zero for all five parameters. With the help of the diagonal matrix

$$
D =
\begin{pmatrix}
-1 & & & & \\
& 1 & & & \\
& & -1 & & \\
& & & -1 & \\
& & & & 1
\end{pmatrix}
\tag{B.5}
$$

and the (constant) column matrix

$$
A =
\begin{pmatrix}
\overline{d}_- + \overline{d}_- \\
\overline{z}_+ - \overline{z}_- \\
\overline{\kappa}_+ + \overline{\kappa}_- \\
\overline{\cot\theta}_+ + \overline{\cot\theta}_- \\
\overline{\phi}_+ - \overline{\phi}_- - \pi
\end{pmatrix},
\tag{B.6}
$$

Δ_- can be rewritten as

$$
\Delta_- = D\left(\Delta_+ + A\right)
\tag{B.7}
$$

so that the the χ^2 expression can be put into a simpler form (note that $D^T = D$ and $V_\pm^T = V_\pm$):

$$
\chi^2 = \Delta_+^T V_+ \Delta_+ + \Delta_-^T V_- \Delta_-
\tag{B.8}
$$

$$
\begin{aligned}
&= \Delta_+^T V_+ \Delta_+ + (D\Delta_+ + DA)^T V_- (D\Delta_+ + DA) \\
&= \Delta_+^T V_+ \Delta_+ + \left(\Delta_+^T D + A^T D\right) V_- (D\Delta_+ + DA) \\
&= \Delta_+^T (V_+ + DV_- D)\Delta_+ + \Delta_+^T DV_- DA + A^T DV_- D\Delta_+ + A^T DV_- DA \\
&= \Delta_+^T (V_+ + DV_- D)\Delta_+ + 2\Delta_+^T DV_- DA + A^T DV_- DA.
\end{aligned}
$$

Setting to zero the derivative of this with respect to the column vector Δ_+ yields

$$
\begin{aligned}
0 &= 2(V_+ + DV_- D)\Delta_+^{min} + 2DV_- DA \qquad\qquad (\text{B.9}) \\
\Delta_+^{min} &= -(V_+ + DV_- D)^{-1}(DV_- DA)
\end{aligned}
$$

This expression for Δ_+^{min} is then used to determine the new set of track parameters via Equation B.3.

Bibliography

[1] Particle Data Group, Phys. Rev. D 54 (1996) 1.

[2] H.Albrecht et al. (ARGUS Collaboration), Phys. Lett. B 192 (1987) 245.

[3] M. Artuso et al. (CLEO Collaboration), Phys. Rev. Lett. 62 (1989) 2233.

[4] S.Abachi et al. (D0 Collaboration), Phys. Rev. Lett. 74 (1995) 2632.

[5] F.Abe et al. (CDF Collaboration), Phys. Rev. Lett. 74 (1995) 2626.

[6] N.G. Cooper and G.B. West ed., *Particle Physics: A Los Alamos Primer*, Cambridge University Press, N.Y. (1988).

[7] T.D.Lee and C.N.Yang, Phys. Rev. 108 (1957) 1611.

[8] M. Gell-Mann, Phys. Lett. 8 (1964) 214; G. Zweig, CERN Report 8182/TH.401 (1964).

[9] P.D.B. Collins et al., *Particle Physics and Cosmology*, John Wiley and Sons Inc., N.Y. (1989).

[10] M. Kobayashi and M. Maskawa, Prog. Theor. Phys. 49 (1973) 652.

[11] S. L. Glashow, J. Iliopoulos, and L. Maiani, Phys. Rev. D 2 (1970) 1285.

[12] J. J. Aubert et al., Phys. Rev. Lett. 33 (1974) 1404; J.-E. Augustin et al., Phys. Rev. Lett. 33 (1974) 1406.

[13] Y.S. Tsai, Phys. Rev. D 4 (1971) 2821.

[14] M. Perl et al., Phys. Rev. Lett. 35 (1975) 1489.

[15] E.D.Commins and P.H.Bucksbaum,*Weak Interactions of Leptons and Quarks*, Cambridge University Press, London (1983).

[16] S.Weinberg, Phys. Rev. Lett. 18 (1967) 507.

[17] T.Das and V.S.Mathur and S.Okubo, Phys. Rev. Lett. 18 (1967) 761.

[18] H.Albrecht et al. (ARGUS Collaboration), Z. Phys. C58 (1993) 61.

[19] A.J. Weinstein, CALT-68-1853 (1993).

[20] D.Buskulic et al. (ALEPH Collaboration), Phys. Lett. B 349 (1995) 585.

[21] H.Albrecht et al. (ARGUS Collaboration), Phys. Lett. B 292 (1992) 221.

[22] Particle Data Group, Phys. Lett. B 239 (1990) 1.

[23] Particle Data Group, Phys. Rev. D 45 (1992) 1.

[24] Particle Data Group, Phys. Rev. D 50 (1994) 1173.

[25] W.Bacino et al. (DELCO Collaboration), Phys. Rev. Lett. 41 (1978) 13.

[26] J.Z.Bai et al. (BES Collaboration), Phys. Rev. D 53 (1996) 20.

[27] R.Balest et al. (CLEO Collaboration), Phys. Rev. D 47 (1993) 3671.

[28] T.N.Truong, Phys. Rev. D 30 (1984) 1509.

[29] F.J.Gilman and S.H.Rie, Phys. Rev. D 31 (1985) 1066.

[30] H.J.Berend et al. (CELLO Collaboration), Z. Phys. C46 (1990) 537.

[31] D.Decamp et al. (ALEPH Collaboration), Z. Phys. C54 (1992) 211.

[32] D. Buskulic et al. (ALEPH Collaboration), CERN-PPE-95-140 (1995).

[33] P.Abreu et al. (DELPHI Collaboration), Phys. Lett. B 365 (1996) 448.

[34] P.Padley, Ph.D. thesis, University of Toronto (1987).

[35] P.Abreu et al. (DELPHI Collaboration), Phys. Lett. B 302 (1993) 356.

[36] D.Buskulic et al. (ALEPH Collaboration), Phys. Lett. B 297 (1992) 432.

[37] D.Buskulic et al. (ALEPH Collaboration), Z. Phys. 70 (1996) 549.

[38] D.Decamp et al. (ALEPH Collaboration), Phys. Lett. B 279 (1992) 411.

[39] I.Park, Ph.D. thesis, l'Université de Paris XI Orsay (1995).

[40] F. James and M. Roos, CERN Program Library, D506, CERN (1993).

[41] B.Andersson et al.: Phys. Lett. B 199 (1987) 291; Phys. Rep. 97 (1983) 31.

[42] H.Albrecht et al. (ARGUS Collaboration), Nucl. Inst. & Meth. in Phys. Res. A275 (1989) 1.

[43] K.W. Edwards et al., Nucl. Inst. & Meth. A252 (1986) 384.

[44] H.Albrecht et al. (ARGUS Collaboration), Nucl. Inst. & Meth. A283 (1989) 544.

[45] M. Danilov et al., Nucl. Inst. & Meth. 217 (1983) 153.

[46] R. Heller et al., Nucl. Inst. & Meth. A235 (1985) 26.

[47] R. Salomon, Diplomarbeit, Heidelberg University, IHEP-HD/83-3 (1993).

[48] A. Drescher et al.: Nucl. Inst. & Meth. 205 (1983) 125; Nucl. Inst. & Meth. 216 (1983) 35; Nucl. Inst. & Meth. A237 (1985) 464; Nucl. Inst. & Meth. A249 (1986) 277.

[49] A. Arefiev et al., DESY 83-025 and Instr. Exp. Tech. 29 (1985) 333.

[50] C.W. Hast, Diplomarbeit, Dortmund University (1988).

[51] H.Kapitza, *Track Fitting at ARGUS*, internal ARGUS note.

[52] L.D. Gladney, Ph.D. thesis, Stanford University (1985).

[53] D.Gilkinson, Ph.D. thesis, University of Toronto (1987).

[54] H. Kapitza, private communication.

[55] M. Danilov, private communication.

[56] H.Kapitza, *The Calibration of the ARGUS Drift Chamber*, internal ARGUS note.

[57] S.Jadach et al.: Comput. Phys. Commun. 36 (1985) 191; Erratum, Acta Phys. Pol. B16 (1985) 483; Comput. Phys. Commun. 64 (1991) 267; Comput. Phys. Commun. 64 (1991) 275.

[58] H. Gennow, *SIMARG, A Program to Simulate the ARGUS detector*, DESY Technical Report, F15-85-02 (1985).

[59] R. Brun et al., CERN-DD/78/2 (1978).

[60] M.W.Grünewald, HUB-IEP-95/13 (1995).

[61] H.Albrecht et al. (ARGUS Collaboration), Z. Phys. C41 (1988) 405.

[62] H.Albrecht et al. (ARGUS Collaboration), Z. Phys. C58 (1993) 61.

[63] R.Balest et al. (CLEO Collaboration), CLNS 96/1417, CLEO 96-8 (1996).

[64] H.Albrecht et al. (ARGUS Collaboration), Z. Phys. C50 (1991) 1.

[65] M. Abramowitz and I.A. Stegun, *Handbook of Mathematical Functions*, Dover Publications Inc., New York (1972).